January 2015

Detailed Investigations of Capillary and van der Waals Forces in the Adhesion between Solids

Aaron Harrison
Purdue University

Graduate School Form 30
Updated 1/15/2015

PURDUE UNIVERSITY
GRADUATE SCHOOL
Thesis/Dissertation Acceptance

This is to certify that the thesis/dissertation prepared

By Aaron J. Harrison

Entitled

Detailed Investigations of Capillary and van der Waals Forces in the Adhesion between Solids

For the degree of Doctor of Philosophy

Is approved by the final examining committee:

Stephen P. Beaudoin
Chair

David S. Corti

Carl Wassgren

James D. Litster

To the best of my knowledge and as understood by the student in the Thesis/Dissertation Agreement, Publication Delay, and Certification Disclaimer (Graduate School Form 32), this thesis/dissertation adheres to the provisions of Purdue University's "Policy of Integrity in Research" and the use of copyright material.

Approved by Major Professor(s): Stephen P. Beaudoin

Approved by: John Morgan 8/19/2015

Head of the Departmental Graduate Program Date

DETAILED INVESTIGATIONS OF CAPILLARY AND VAN DER WAALS FORCES IN THE ADHESION BETWEEN SOLIDS

A Dissertation

Submitted to the Faculty

of

Purdue University

by

Aaron J. Harrison

In Partial Fulfillment of the

Requirements for the Degree

of

Doctor of Philosophy

December 2015

Purdue University

West Lafayette, Indiana

To my wife and children:

Increased recycle rate increases conversion

ACKNOWLEDGEMENTS

I'm not sure that anyone who begins the journey of completing a dissertation and all of the research that is associated therein ever fully comprehends the gravity of the situation until they face a blank screen waiting to be filled with years of hard work. It is probably at that moment that they realize this journey has not been theirs alone, but has been shared with those closest to them. So it has been with me.

I thank my advisor Steve Beaudoin for his technical guidance on all of my varied projects, his friendship, and most importantly patience with me throughout this process. I also thank my co-advisor Dave Corti for his tireless efforts in helping me to understand statistical mechanics, thermodynamics, and proper simulation etiquette. With the AFM-IR project, I thank Lynne Taylor for her guidance and patience while I struggled through experimental challenges. Moreover, I thank Jim Litster and Carl Wassgren for serving on my dissertation committee. Thank you also to all of my coworkers and dear friends for your support.

Without a doubt, my parents have been with me throughout this entire process and I thank them for their love and support, as well as their commitment to education and training me in the way that I should go. Their efforts continue to bless me.

Throughout my time in graduate school, I've often heard that being married and rearing children while in graduate school must be a challenge and most are thankful to

have avoided it. Yet for me, my wife and children are the reason to come home at night, the reason to keep on trying, and the reason life can be so joyous. I thank my children for the smiles and the laughter after a hard day at work. And of course, these wonderful moments are all because of my wife and her hard, routine, and often thankless work. I thank her for everything she is. She truly deserves this dissertation and degree in her own field of Plant Genetics more than I do in mine.

Finally, as I have tried to understand the intricacies of particle science I have often felt inspired like Moses when he "cast his eyes and beheld the earth, yea, even all of it; and there was not a particle of it which he did not behold, discerning it by the Spirit of God" (Moses 1:27, *Pearl of Great Price*).

TABLE OF CONTENTS

Page

LIST OF TABLES

LIST OF FIGURES

Figure Page

Figure Page

LIST OF SYMBOLS

Chapters 1-3 Symbols: Roman Symbols

A – Interfacial surface area for a given interface and curvature,
$\bar{A}_I$ – Planar interfacial area divided by σ^2
$\bar{A}_{int}$ – Area of the circular segment divided by σ^2
A_{LG} – Area of the liquid-vapor interface
$\bar{A}_S$ – Surface area of the plates divided by σ^2 or σ for 2-D
A_S – Solid surface area
A_{SL} – Area of the solid-liquid interface
A_w – Wetted area
a – Distance of the center of the circle to $N_x/2$ divided by σ
b – Radius of a sphere
b_S – Binding energy of the adsorbate to the lower solid surface
b_T – Binding energy of the adsorbate to an AFM tip or top surface
c – Height of the meniscus onto the particle, length of the chord of a circle divided by σ
c_i – Occupation of site i (*i.e.,* 0 or 1)
E^b – Internal energy for a bulk system with the same volume as the true system
E – Internal Energy
$\mathcal{F}$ – Helmholtz free energy
f – Modification factor in the WLMC technique
F_C – Total capillary force
$\bar{F}_C$ – Total capillary force multiplied by σ/ε
F_S – Surface tension force
F_p – Capillary pressure force
G – Gibbs Energy
$g(E,N)$ – Density of states for a given E and N
h - Plate separation
$\bar{h}$ - Plate separation divided by σ
I – Identity tensor
J – Mean curvature of an interface
k_B – Boltzmann's Constant
l_w – Wetted perimeter
N – Total number of moles (or molecules) in the system
N_0 – Total number of lattice sites within a bubble
N_a – Number of occupied sites

N^b – Number of molecules or moles in a bulk system
N_{tot} – Total number of lattice sites
$\boldsymbol{n}$ – Unit normal from the interface into phase β
n – Number of molecules within a bubble, or iteration number
P – Probability of accepting a Monte Carlo move
$\bar{P}_{int}$ – Perimeter of the circular segment divided by σ
p – Pressure of the system or pressure component normal to the interface
$\bar{p}$ – Non-dimensional pressure normal to the interface
p_G – Bulk, homogenous pressure in the vapor phase
p_L – Bulk, homogenous pressure in the liquid phase
p_{ref} – Reference pressure of the critical bubble
$\bar{p}_{ref}$ – Non-dimensional reference pressure of the critical bubble
p^S – Saturation pressure
$\bar{p}_{T,i}$ – Non-dimensional transverse pressure at a specified site
$\bar{p}_T$ – Non-dimensional transverse pressure
p^α – Bulk pressure in the α phase
p^β – Bulk pressure in the β phase
R – Radius of a spherical interface
$\bar{R}$ - Radius of a curved interface divided by σ
r – Radius of the three-phase contact line
R_1 – Principal radius of curvature of an interface in the plane of the page
R_2 – Principal radius of curvature of an interface into and out of the page
R_b – Radial distance from the bubble center
$\bar{R}_e$ – Equimolar dividing surface for a radial system divided by σ
$\bar{R}_s$ – Surface of tension for a radial system divided by σ
R_s – Kelvin radius, radius of curvature of an interface at the surface of tension
S^b – Entropy for a bulk system
S – Entropy
T – Absolute temperature
T_c – Critical temperature
$\mathbf{T}^\alpha$ – Bulk stress tensor in the α fluid phase
$\mathbf{T}^\beta$ – Bulk stress tensor in the β fluid phase
V – Total volume of the system
V_G – Volume of the vapor phase
V_L – Volume of the liquid phase
$\mathrm{V_m}$ – Molar volume
$V_{m,L}$ – Liquid molar volume
V_o – Volume per lattice site
$\bar{V}_o$ – Volume of a lattice site divided by σ^3
V_S – Volume of the solid surface
$\bar{X}_e$ – Equimolar dividing surface for a planar interface divided by σ
$\bar{X}_s$ – Surface of tension for a planar interface divided by σ
Z – Partition function

Z^b – Partition function for a bulk system with the same volume as the true system
$\mathcal{Z}$ – Total number of possible bonds per site

Chapters 1-3: Greek Symbols

α – Refers to the state of matter of the species (different than β phase)
β – Refers to the state of matter of the species (different than α phase)
β_w – Energy of adsorption of a molecule onto a wall divided by ε
γ – Surface energy of an interface
$\bar{\gamma}_s$ – Fluid-fluid surface tension at the surface of tension multiplied by σ^2/ε
$\bar{\gamma}_\infty$ - Planar surface tension (unitless)
γ_{LG} – Fluid-fluid surface tension
$\bar{\gamma}_{LG}$ – Fluid-fluid surface tension multiplied by σ^2/ε
γ_{SF} – Solid-fluid interfacial tension
γ_{SG} – Solid-vapor surface energy
γ_{SL} – Solid-liquid surface energy
ΔP – Laplace Pressure
δ – Tolman length divided by σ
ε – Intermolecular attraction energy
η_i – Matrix occupancy or whether or not a site is adjacent to a wall
θ – Dimensionless temperature term (k_bT/ε)
$\bar{\kappa}$ – Chemical potential inside of a bubble, Lagrange multiplier
μ – Chemical potential of the system
$\bar{\mu}$ – Chemical potential of the system divided by ε (unitless)
μ_c – Chemical potential at the bulk gas-liquid transition
μ^o – Reference chemical potential
μ^α – Chemical potential in the α phase
μ^β – Chemical potential in the β phase
ρ – Average density or average occupancy for a bulk system
ρ_c – Critical density
ρ_c^G – Density of the site at the center of the bubble.
ρ^G – Average occupation of sites or density in the bulk vapor
ρ_i – Average density or average occupancy at site i
ρ^L – Average occupation of sites or density in the bulk liquid
σ – Molecular diameter and lattice spacing unit
ϕ – Contact angle
ϕ_1 – Contact angle of the liquid bridge against upper plate
ϕ_2 – Contact angle of the liquid bridge against lower plate
ϕ_f – Filling angle
ϕ_n – Angle of inclination
Ω – Grand potential of the system
$\overline{\Omega}$ – Grand potential of the system divided by ε (unitless)
Ω^b – Grand potential of a bulk system with the same volume as the true system
$\overline{\Omega}^{ex}$ – Excess energy or grand potential of the system divided by ε

$\overline{\Omega}^G$ – Grand potential or energetic contribution of the bulk vapor divided by ε
$\overline{\Omega}_{int}^G$ – Grand potential of the bulk vapor within the circular segment divided by ε
$\overline{\Omega}^{\mathrm{L}}$ – Grand potential or energetic contribution of the bulk liquid divided by ε
$\overline{\Omega}_{int}^L$ – Grand potential of the liquid bridge within the circular segment divided by ε.

Chapters 1-3: Mathematical Operators

$\langle\ \rangle$ - Ensemble average of a specified thermodynamic quantity
$grad_s$ – Non-normal component of the surface gradient ($grad_s = \nabla - \boldsymbol{n}(\boldsymbol{n} \cdot \nabla)$)

Chapter 4: Roman Symbols

A – Hamaker Constant
a – Cross-sectional area of the probe molecule
A_{ii} – Cohesive Hamaker Constant
A_{ijk} – Adhesive Hamaker Constant
C – Constant of integration dependent on the chosen reference state
D_0 – Separation between surfaces, ~ 0.165 nm
F – Exit flow rate of the probe
i – Indicates and adhering material, refractive index wavelength
j – Medium through which two materials are adhering
j_m – James-Martin compressibility factor
k – Indicates an adhering material, Boltzmann's Constant
m – Mass
N_A – Avogadro's number
n_i – Refractive index at wavelength i
R – Ideal gas constant
T – Temperature
t_n – Net retention time of the probe
T_r – Reference Temperature
V_n – Net retention volume
W_A – Energy of adhesion per unit surface area
W_A^D – Dispersive energy of adhesion per unit surface area

Chapter 4: Greek Symbols

ΔG^0 – Gibbs energy of adsorption
γ – Surface tension
γ^D – Dispersive component to the surface tension
γ^P – Polar component to the surface tension
γ_L^D – Dispersive surface tension of a liquid
γ_S^D – Dispersive surface tension of a solid
γ_S^p – Polar component of the surface tension of a solid

γ^T – Total surface tension
ε_i – Dielectric constant
v_e – Main electronic absorption frequency).

ABSTRACT

Harrison, Aaron J. Ph.D., Purdue University, December 2015. Detailed Investigations of Capillary and van der Waals Forces in the Adhesion between Solids. Major Professors: Stephen Beaudoin and David Corti.

The primary focus of this dissertation is on characterizing two fundamental forces common to adhesion between solids: capillary and van der Waals forces. These two forces have a significant impact on how solids flow, stick to surfaces, agglomerate and break; therefore, understanding their behavior can lead to better processing techniques.

Capillary forces are responsible for caking in the food, cosmetic, and pharmaceutical industries and are caused by the spontaneous formation of liquid bridges between two surfaces in close contact. To better understand how capillary forces depend on the system relative humidity (RH), solid surface separation, and surface hydrophilicity, the Wang-Landau Monte Carlo technique on a lattice-gas framework has been used. For a smooth, hydrophilic AFM tip against a flat, hydrophilic plate on a 45x45 lattice, a maximum capillary force occurs when the separation distance is one molecular diameter of the adsorbate and the capillary force decreases as the separation distance increases, except when the tip and the surface are in contact. The capillary forces associated with completely wetting AFM tips are strongly dependent on the system RH, while partially wetting and partially drying tips are relatively independent of RH.

Interestingly, capillary forces can be significant in low RH environments and thus cannot be ignored in AFM studies involving hydrophilic surfaces.

Another aspect in predicting capillary forces involves the use of the Kelvin equation, which describes the relationship between the system saturation and the curvature of the liquid-vapor interface. Using a two-dimensional lattice-gas model with mean-field density functional theory, the effect of meniscus curvature on the prediction of the Kelvin equation has been studied. First, the dependence of the surface tension on the curvature of the liquid-vapor interface is established for critical bubbles forming within a bulk liquid. It is demonstrated that for a pure-component, bulk system the Kelvin equation properly describes the curvature of the interface at the Gibbs surface of tension, even for very small bubbles. Next, the system is modified to include parallel, hydrophilic surfaces between which capillary bridges can form. The curvature of these capillary bridges is quantified at differing saturation levels, separation distances and contact angles and then compared to the Kelvin equation. For these capillary bridges, it is found that the radius of curvature is not constant (*i.e.,* the meniscus is not circular) and that the Kelvin equation is a non-physical extrapolation as the system approaches zero saturation or as the separation distance decreases. Therefore, the Kelvin equation best describes curvatures for pure-component systems or for capillary bridges that are near or at saturation and with large plate separations.

Dry adhesion caused by dipole-dipole interactions (*i.e.*,van der Waals forces) have also been considered. The Hamaker constants (which are a measure of the van der Waals forces) and dispersive surface energies have been characterized for ten energetic powders using inverse gas chromatography. It has been determined that the effect of the

amount of fuel additives in the energetic powders on Hamaker constants is not statistically significant. In addition, the Hamaker constants agree with Lifshitz theory indicating that inverse gas chromatography is a possible alternative for characterizing the dry adhesion of powders. Lastly, when combined with a better prediction of capillary forces, these experimentally determined Hamaker constants can lead to better models describing the removal of these energetic materials.

Finally, an ancillary project investigating the nanoscopic, chemical properties of crystalline griseofulvin embedded in polymer is also included in this dissertation. Obtaining small-scale chemical information from traditional infrared (IR) spectroscopy has recently been improved from 3-30 μm to 10-100 nm by combining atomic force microscopy (AFM) with IR and is known as AFM-IR. It is shown that AFM-IR can chemically distinguish drug nanoparticles embedded in polymer with a sub-100 nm resolution, which is a considerable improvement over traditional IR techniques.

CHAPTER 1. INTRODUCTION

1.1 Overview

The handling, manufacturing, and processing of solid materials represents a substantial portion of the world's economic interests. For example, in 1993, the U.S. Department of Commerce estimated that particulate products contributed approximately one trillion dollars to the U.S. economy [1]. The following year, Ennis, Green, and Davies reported that 62% of DuPont's 3000 products were "powders, crystalline solids, granules, flakes, dispersions, slurries, and pastes" [2]. Similarly, 50% of Dow Chemical's products have been estimated to be particulates [3]. Yet, the behavior of particulate matter is difficult to predict and hence affects the reproducibility of solid processing systems. As such, there is an academic and industrial drive to accurately understand and model the behavior of particulate matter in a wide variety of applications to improve the product reproducibility and quality control of solids processing.

Adhesion between solid particles and between solid particles and surfaces in a medium is fundamental to all aspects of solids processing. Among other things, the adhesion affects how solids flow, stick to surfaces, agglomerate and break. Several forces, such as van der Waals (vdW) forces, electrostatic forces, and forces caused by condensed vapors (i.e., capillary forces) influence the strength of adhesion. The

condensed vapor forces are of particular interest because they will tend to dominate the adhesive interaction when present [4]–[9]. To correctly predict the magnitude of the adhesion between particles and substrates, capillary forces must, therefore, be included in the analysis. However, both capillary-induced adhesion and dry cohesion of solids are considered in this work.

The remainder of this chapter describes the basic equations of capillarity; evaluates atomic force microscope (AFM) measurements of capillary forces throughout the literature; derives the most common analytical equations to describe capillary forces between surfaces; and outlines common simulation techniques. Chapter 2 focuses primarily on determining capillary forces between an AFM tip and a flat surface at varying separation distances, relative humidity levels and hydrophilicity using the Wang-Landau Monte Carlo technique on a lattice-gas framework. Mean-field density functional theory is then used in Chapter 3 to evaluate the applicability of the Kelvin equation in analytical methods to describe capillarity between solid surfaces.

Dry cohesion and solid, dispersive surface energies of ten energetic powders have been characterized in Chapter 4 using inverse gas chromatography. This has direct application in detecting trace amounts of explosives residues. A review of the important literature for that topic is contained in the introduction to that chapter.

Chemical characterization of solids systems is also an important aspect to solid processing, especially for pharmaceutical solid dispersions where the proper dosage of a drug is critical. Therefore, the resolution limits and chemical characterization of a crystalline drug embedded in polymer are established for photothermal-induced

resonance in Chapter 5. Its appropriate literature review is also the introduction to that chapter.

1.2 Introduction to Capillarity

Capillarity is the governance of the effects of surface tension in a given system. Through capillary action, redwood trees transport hundreds of liters of water per day up to 116 vertical meters without the use of a pump [10] and horny devils drink the water that condenses onto their backs in the deserts of Western Australia [11]–[13]. Through capillary condensation, capillarity provides the increased adhesion necessary to mold sand into sandcastles [14]. Similarly, capillarity influences how chemical, pharmaceutical, food, and cosmetic powders flow, stick to surfaces, agglomerate, and break [15], which affects the reproducibility and quality of processing these powders. Hence, there is a biological and industrial interest in understanding and predicting capillary behavior.

The present review focuses on forces caused by capillarity (i.e., capillary forces) in the context of particle adhesion to facilitate powder processing. Adhesion between solid particles and between solid particles and surfaces in a medium is fundamental to all aspects of solids processing. Several forces, such as van der Waals (vdW) or dipole-induced forces, electrostatic forces, and capillary forces influence the strength of adhesion [16]. Capillary forces are of particular interest because they tend to dominate the adhesive interaction when present [4]–[9].

Water is the typical component studied in capillarity because of its ubiquitous nature in experiments and application. However, capillary action, condensation, and capillary forces can happen with a variety of adsorbates, such as organic solvents [17]–[20], with or without a high vapor pressure [14], and even within immiscible fluid-fluid mixtures [21]. The principles of capillarity discussed in this review will be applicable to any type of adsorbate, but the applications will generally refer to water-based systems.

This review begins with the basics of capillarity and capillary forces. This is then followed by the derivation of the governing equations of capillarity and a brief discussion of their utility and applicability. A variety of aspects surrounding the experimental determination and validation of capillary forces primarily via atomic force microscopy are then analyzed. Next a survey of analytical models assuming ideal and non-ideal geometries is presented. This is followed by an analysis of several molecular approaches to simulating capillary forces. Finally, a summary of theoretical, experimental, and analytical utility and applicability is discussed.

1.3 Capillarity Concepts

The excess free energy caused by the formation of an interface when divided by the interfacial area is commonly referred to as the surface energy (or tension for a fluid-fluid system). For a planar interface, it is defined as the reversible work required to increase the interfacial area by a unit area at constant pressure, volume (or total moles) of each component in the system, and temperature [22], or as the work required to bring molecules out of a bulk phase and into the interface as the interface expands [23]. In

terms of forces, the surface energy is the cohesive force per unit length tangent to the interface and normal to its curvature [22]–[24], which results in an elastic, membrane-like surface separating the phases. Because of the surface energy, two bulk phases can be in mechanical equilibrium even if the pressures in the two phases are different; the surface energy balances the net force caused by the pressure difference. In this case, the surface energy is regarded as the amount of work added to the system with a unit change in the area of the dividing surface for a given interfacial curvature [22]. In order to minimize the free energy of the system, the interface will assume the shape with the least amount of surface area. For a two-phase, fluid-fluid system without any external fields, the interface will always be spherical (*e.g.*, droplets and bubbles).

The pressure difference across a curved interface is commonly referred to as the Laplace or capillary pressure and it pushes the interface in the concave direction [25]. This means that the liquid in a droplet has a positive or compressive Laplace pressure, whereas the liquid in a bubble has a negative or tensile Laplace pressure [25] (Figure 1.1). Similarly, the fluid in concave menisci between two solid bodies may also have a negative pressure, which increases the attraction between the two solids. The increased attraction caused by the surface energies and the pressure difference between two solids is the origin of capillary forces in particle adhesion.

For a meniscus to form between two solid bodies, the surfaces must be lyophilic (able to attract the adsorbate) or the system must be at or very near saturation. When two such solids are in close contact, a meniscus forms by either the spontaneous condensation of a vapor in a confined space, otherwise known as capillary condensation; or, for non-volatile liquids, the combination of adsorbed layers on the two surfaces which are drawn

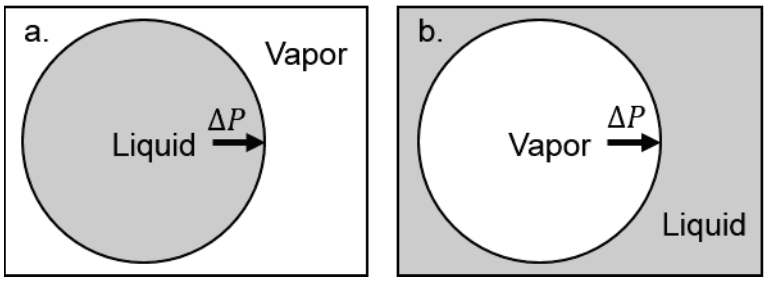

Figure 1.1 The Laplace pressure (ΔP) acts in the concave direction of the interface. a. Liquid droplets surrounded by vapor have positive Laplace pressures. b. Liquid surrounding vapor bubbles have negative Laplace pressures.

into a meniscus [14]. The size of the meniscus depends on several factors including the surface energy of the condensate and solid bodies, the pressures within each bulk phase, the saturation of the system, and the temperature, which also influences the strength of the capillary forces. The challenge of accurately predicting and measuring the impact and magnitude of these forces is addressed throughout the remainder of this article.

1.4 Governing Equations

The three fundamental equations of capillarity are the Young-Laplace equation, the Young equation and the Kelvin equation. The Young-Laplace equation relates the mean curvature of the interface to the pressure difference, whereas the Young equation relates the fluid-fluid surface energies to the solid-fluid surface energies. Both can be derived from classical force balances [23]–[26], thermodynamics [22], [27]–[31], and hydrostatics [29], [32]. The Kelvin equation represents the dependence of the curvature of the interface on the saturation of the system and is typically derived using thermodynamics. Commonly used derivations and forms of these equations are presented

here with some comments as to their utility and application. This will prove useful for analyzing experimental studies and models regarding capillary forces.

1.4.1 Young-Laplace and Young Equations

1.4.1.1 Derivation

Consider a two-phase, fluid-fluid system separated by an interface (Figure 1.2). From a classical point of view, the differential-stress balance yields [23]

$$\left(\mathbf{T}^{\beta} - \mathbf{T}^{\alpha}\right) \cdot \boldsymbol{n} + grad_s \gamma_{LG} - \gamma_{LG} \boldsymbol{n} (\nabla \cdot \boldsymbol{n}) = 0 \qquad (1.1)$$

where $\mathbf{T}^{\alpha}$ and $\mathbf{T}^{\beta}$ are the bulk, stress tensors in the α or β fluid phase, $\boldsymbol{n}$ is the unit normal from the interface into phase β, $grad_s = \nabla - \boldsymbol{n}(\boldsymbol{n} \cdot \nabla)$, and γ_{LG} is the fluid-fluid surface tension. The surface gradient describes spatial variants within the surface and has been divided into its tangential ($grad_s \gamma_{LG}$) and normal ($\gamma_{LG} \boldsymbol{n} (\nabla \cdot \boldsymbol{n})$) components for convenience. Assuming that the system is static, the stress tensor is related to the bulk pressures in the α and β phases (p^{α} and p^{β}, respectively) and strictly diagonal. Thus, $\mathbf{T}^{\alpha} = p^{\alpha}\mathbf{I}$ and $\mathbf{T}^{\beta} = p^{\beta}\mathbf{I}$, where $\mathbf{I}$ is the identity tensor. If only the normal component of the stress balance is considered, equation (1.1) reduces to

$$p^{\alpha} - p^{\beta} = \gamma_{LG} (\nabla \cdot \boldsymbol{n}). \qquad (1.2)$$

Recognizing that $(\nabla \cdot \boldsymbol{n})$ is related to the curvature of the interface, it is immediately apparent that equation (1.2) is the Young-Laplace equation. However, $(\nabla \cdot \boldsymbol{n})$ is more usefully expressed as the mean curvature J of the two principal radii, R_1 and R_2:

$$(\nabla \cdot \boldsymbol{n}) = \left(\frac{1}{R_1} + \frac{1}{R_2}\right) = J. \tag{1.3}$$

For a spherical interface, $R = R_1 = R_2$, and equation (1.2) becomes

$$p^{\alpha} - p^{\beta} = \frac{2\gamma_{LG}}{R}. \tag{1.4}$$

Note that the curvature of the interface may be positive or negative depending on how the phases are defined. For example, if the liquid is defined to be the α phase for a droplet, the curvature will be positive. On the other hand, if the liquid is the α phase surrounding a bubble, the curvature will be negative.

For a system where there is a solid surface interacting with a liquid and a vapor (*e.g.*, a sessile drop), there exists a contact-line between the solid-liquid (subscript *SL*), solid-vapor (subscript *SG*) and liquid-vapor (subscript *LG*) interfaces. A force balance on this contact line in the plane of the solid reveals [23], [25], [26]

$$\gamma_{LG} \cos\phi = \gamma_{SG} - \gamma_{SL}, \tag{5}$$

where ϕ is the contact angle, γ_{SG} is the surface energy of the solid-vapor interface, and γ_{SL} is the surface energy of the solid-liquid interface (Figure 1.3). Equation (1.5) is known as the Young equation and provides an important relation between the fluid-fluid surface energy and the solid-fluid surface energies.

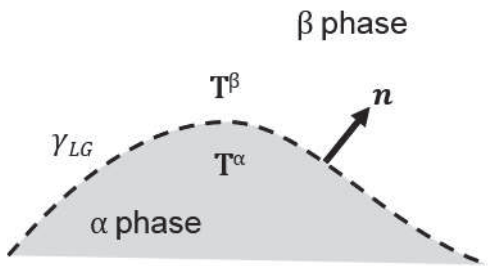

Figure 1.2 Stresses on a fluid-fluid interface. $\mathbf{T}^{\alpha}$ and $\mathbf{T}^{\beta}$ are the bulk, stress tensors in the α or β fluid phase, $\boldsymbol{n}$ is the unit normal, and γ_{LG} is the fluid-fluid surface tension.

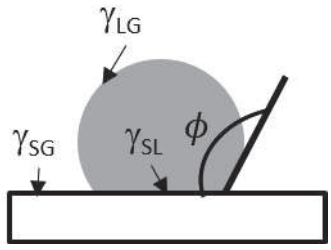

Figure 1.3 The contact angle ϕ between a sessile drop and a solid surface. γ_{SG}, γ_{SL}, and γ_{LG} are the surface energies of the solid-vapor, solid-liquid and liquid-vapor interfaces, respectively.

To discuss some technical aspects of equations (1.2) and (1.5), it is of interest to consider them from a thermodynamic standpoint. The following discussion is based on the method developed by Gibbs, which is elucidated elsewhere [22], [31], [33]. Consider a three-phase system, where the liquid and vapor consist of one component and the solid surface is inert and has a constant volume V_S and surface area A_s (*i.e.*, $\mathrm{d}V_s = 0$ and $\mathrm{d}A_s = 0$). The differential of the free energy $\mathcal{F}$ can then be expressed as [28]

$$\mathrm{d}\mathcal{F} = -S\mathrm{d}T - p_L\mathrm{d}V_L - p_G\mathrm{d}V_G + \gamma_{LG}\mathrm{d}A_{LG} + \gamma_{SL}\mathrm{d}A_{SL} + \gamma_{SG}\mathrm{d}A_{SG} + \mu\mathrm{d}N \qquad (1.6)$$

where S is the entropy; T is the absolute temperature; p_L and p_G are the bulk,

homogeneous pressures in the liquid and vapor phases on either side of the interface; V_L and V_G are the volume of the liquid and vapor phases, respectively; A is the interfacial surface area for a given interface at the surface of tension; μ is the chemical potential (which is the same in the liquid and vapor phases at equilibrium); and N is the number of moles in the liquid and vapor system. For an isothermal and constant mass system (*i.e.*, $\mathrm{d}T = 0$ and $\mathrm{d}N = 0$), equation (1.6) reduces to

$$\mathrm{d}\mathcal{F} = -p_G \mathrm{d}V + (p_G - p_L)\mathrm{d}V_L + \gamma_{LG}\mathrm{d}A_{LG} + (\gamma_{SL} - \gamma_{SG})\mathrm{d}A_{SL} \qquad (1.7)$$

by remembering that $V = V_G + V_L$ and $dV_G = \mathrm{d}V - \mathrm{d}V_L$, where V is the total volume of the system and that $\mathrm{d}A_S = 0 = \mathrm{d}A_{SG} + \mathrm{d}A_{SL}$.

At equilibrium, the Helmholtz free energy must be at a minimum at constant V, T and N. Therefore,

$$\mathrm{d}\mathcal{F} = 0 = (p_G - p_L)\mathrm{d}V_L + \gamma_{LG}\mathrm{d}A_{LG} + (\gamma_{SL} - \gamma_{SG})\mathrm{d}A_{SL} \qquad (1.8)$$

which leads to

$$(p_G - p_L)\mathrm{d}V_L = -\gamma_{LG}\mathrm{d}A_{LG} - (\gamma_{SL} - \gamma_{SG})\mathrm{d}A_{SL}. \qquad (1.9)$$

This is the Young-Laplace equation from a thermodynamic viewpoint although it may not be immediately apparent that equation (1.9) reduces to equation (1.2) for a droplet or bubble. Yet, for a pure-component, spherical droplet (Figure 1.4), $\mathrm{d}V_L = 4\pi R^2$, $\mathrm{d}A_{LG} = 8\pi R$ and $\mathrm{d}A_{SL} = 0$, which leads to equation (1.4).

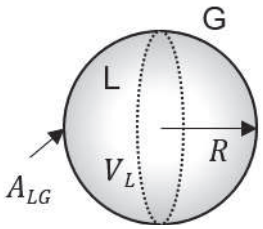

Figure 1.4 Geometry of a spherical droplet in vapor. R is the radius, V_L is the volume, and A_{LG} is the surface area of the droplet

A similar relationship between the three surface energies can be derived for a system consisting of a cylindrical capillary tube with a known inner radius *r* and contact angle ϕ (Figure 1.5). Here, $\mathrm{d}V_L = \pi r^2$, $\mathrm{d}A_{LG} = 0$ and $\mathrm{d}A_{SL} = 2\pi r$ and equation (1.9) reduces to

$$(p_G - p_L) = -\frac{2(\gamma_{SL} - \gamma_{SG})}{r}. \tag{1.10}$$

Utilizing the force balance and noting that that $R = R_1 = R_2$ and $r = R\cos\phi$ in this system, the Laplace pressure must be

$$(p_G - p_L) = \frac{2\gamma_{LG}\cos\phi}{\mathrm{R}} \tag{1.11}$$

because of equations (1.2) and (1.3). Setting equations (1.10) and (1.11) equal to one another reveals

$$\gamma_{LG}\phi = \gamma_{SG} - \gamma_{SL}, \tag{1.12}$$

which is identical to equation (1.5). Though not a purely thermodynamic derivation, the thermodynamic approach reveals that if $\mathrm{d}A_{LG}$ is not independent of $\mathrm{d}A_{SL}$, such as might

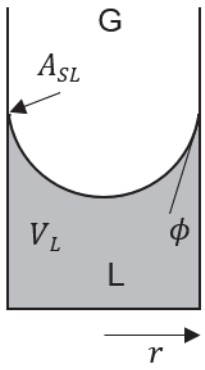

Figure 1.5 Geometry of a curved meniscus in a cylindrical capillary tube. r is the inner radius of the tube, ϕ is the contact angle, V_L is the liquid volume, and A_{SL} is the liquid-solid surface area

be the case for heterogeneous, rough surfaces, then the Young equation becomes much more complex [28]. These complexities related to the determination of the contact angle have been extensively studied [25], [34]–[38] and will not be discussed here.

1.4.1.2 Theoretical and Experimental Limitations

The derivation presented for the Young-Laplace equation is specific to a fluid-fluid system, though it is more general [27], [28], [32], and applies to solid systems [25], reversible, non-isothermal systems, as well as open systems [28]. However, it is important to note that the Young-Laplace equation does operate under some assumptions:

1. The system must be static (no motion in the bulk phase) [23].
2. Bulk pressures are maintained on either side of the interface [22].

That the system must be static means that there can be no bulk motion within the phases toward, away from, or across the interface. The implication here is that if the

system is changing faster than the interface can reach an equilibrium shape, then the Laplace equation will not apply. This is an important aspect to consider when performing and evaluating experimental capillary force studies.

The second assumption is not overly restrictive except in the cases where the curvature is high, and/or the pressure inside phase α is not the bulk pressure. These situations typically occur in very small bubbles and droplets or other nucleation sites. The thermodynamic aspects of these nuclei are considered in section 1.4.2. Still, it should be noted that the Young-Laplace equation can be used even if phase α is not at a bulk pressure. The analysis does require the use of a different reference pressure, like the normal pressure at the center of phase α [31]. Note also that the application of the Young-Laplace equation becomes more complex in the presence of an external field because the isotropy of the pressure tensor changes.

The real challenge in using the Young-Laplace equation is determining the actual shape of the interface. Even for simple geometries, this may be analytically and numerically complex. It is common to encounter functions of incomplete elliptic integrals [39], especially for non-spherical interfaces and complex surface geometries [27], [28]. Yet, this level of precision may not be necessary to accurately represent the magnitude of capillary forces in a given system. Approaches to estimate the shape of the interface are summarized by Schrader *et. al.* [40] and is also discussed in Chapter 3.

The Young equation is less robust and includes these assumptions:

(1) The solid-fluid interfacial surface energies are invariant as the fluid spreads across the surface (*e.g.*, the solid surface is smooth and homogeneous) [28].

(2) The adsorbates do not form a thin film [34].

For the majority of real systems, a solid surface has a significant degree of roughness and heterogeneity. Depending on the severity of the deviation from ideality, these factors will affect the form of equation (1.5) [34]. The second assumption limits the use of the Young equation to moderate or large contact angles because thin films do not exhibit bulk liquid behavior. For low contact angles, the concept of the disjoining pressure must be introduced [25], [41], [42]. Therefore, care must be taken so that the proper form of the Young equation is used for a system of interest [28], [37].

1.4.2 Kelvin Equation

The Kelvin equation describes the relationship between the system saturation and the curvature of the interface. It is extensively used to describe nucleation in supersaturated systems [35], and capillarity in unsaturated systems [25].

1.4.2.1 Derivation

For a pure-component system, let two phases exist in mechanical, thermal, and chemical equilibrium, such that

$$\mu^{\alpha}(T, p^{\alpha}) = \mu^{\beta}\left(T, p^{\beta}\right) \tag{1.13}$$

where μ^{α} and μ^{β} are the chemical potentials in the α and β phases, respectively. It is convenient to choose a reference state where the curvature of the interface is zero, $J = 0$, and the pressures on either side of the interface are equal to the saturation pressure p^{S} [28]. Hence the reference chemical potential μ^{o} is

$$\mu^o = \mu^\alpha(T, p^S) = \mu^\beta(T, p^S) \tag{1.14}$$

Subtracting equation (1.14) from equation (1.13) yields,

$$\mu^\alpha(T, p^\alpha) - \mu^\alpha(T, p^S) = \mu^\beta\left(T, p^\beta\right) - \mu^\alpha(T, p^S) \tag{1.15}$$

At this point, it is important to note that for an isothermal, pure-component system

$$\int_{\mu^o}^{\mu} \mathrm{d}\mu = \int_{p^S}^{p} V_m \mathrm{d}p \tag{1.16}$$

where V_m is the molar volume and an equation of state must be assumed for phase α and β, which will also inherently specify the type of phase. If phase α is an incompressible liquid,

$$\mu_L - \mu^o = V_{m,L}(p_L - p^S). \tag{1.17}$$

with $V_{m,L}$ as the liquid molar volume. If phase β is an ideal gas,

$$\mu_G - \mu^o = RT \ln\left(\frac{p_G}{p^S}\right) \tag{1.18}$$

and p_G/p^S is the relative vapor pressure or relative humidity (RH) for water vapor. Equation (1.15) then becomes

$$V_{m,L}(p_L - p^S) = RT \ln\left(\frac{p_G}{p^S}\right). \tag{1.19}$$

It is convenient to express equation (1.19) in terms of the pressure of the vapor p_G. The Young-Laplace equation provides the necessary relationship and equation (1.19) can be solved to show

$$p_G - p^s - \gamma_{LG} J = \frac{RT}{V_{m,L}} \ln\left(\frac{p_G}{p^s}\right). \quad (1.20)$$

Noting that $p_G - p^s$ is typically negligible (< 0.1% of $RT/V_{m,L}$), equation (1.20) takes on the traditional form of the Kelvin equation

$$R_s = \left(\frac{1}{R_1} + \frac{1}{R_2}\right)^{-1} = -\frac{V_{m,L}\gamma_{LG}}{RT \ln\left(\frac{p_G}{p^s}\right)}. \quad (1.21)$$

where R_s is the Kelvin radius.

1.4.2.2 Theoretical and Experimental Limitations

Though equation (1.21) and other variations using simple geometrical interfaces are commonly presented in literature, it is an approximation [22], [27]–[29], [43] governed by some underlying assumptions that must be considered carefully before it can be properly employed.

As presented, equation (1.21) is only valid for a pure-component system, (*e.g.*, water vapor and liquid water). Since air is a mixture of gases, any theoretical treatment or experiment conducted in air violates this assumption, strictly speaking. Although this assumption may prove to be inconsequential if the extraneous components are chemically inert or mutually soluble across the interface, it is an important aspect to consider for multi-component, non-ideal systems such as in oil extraction [43]. The appropriate alterations for this case to the Kelvin equation can be found in references [43]–[45].

Because the Young-Laplace equation is used to obtain the Kelvin equation, the system must be static. Hence, the kinetics of droplet, bubble, or meniscus formation are

completely neglected in the Kelvin equation. Whether or not this particular constraint is met experimentally is debatable and is discussed in section 1.5.7.

The system must also be in thermal equilibrium, which indicates that capillary condensation does not occur between two solids because of a temperature gradient. It depends solely on the relative vapor pressure, interfacial surface energy, and the molar volume of the condensed phase at a given temperature.

To integrate equation (1.16), the phases and their appropriate equations of state must be specified. Therefore, equation (1.21) is only applicable to a liquid-vapor interface. For systems with other combinations of phases in equilibrium, the Kelvin equation will be different. For pure-component, isothermal, solid-vapor systems, the form of the Kelvin equation is the same as equation (1.21) except that p^S becomes the solid saturation pressure, the molar volume refers to the solid state and the surface tension is the solid-vapor tension [35]. Liquid-liquid systems commonly utilize activity coefficients and liquid-solid systems may require the concept of the disjoining pressure to obtain the proper form of the Kelvin Equation [35]. Additionally, the phases are assumed to be ideal such that the vapor follows the ideal gas law and the liquids and solids are incompressible. For systems dealing with water vapor in an ambient environment, the ideal gas assumption is reasonable. However, at high pressures or low temperatures, this assumption is tentative and requires the use of a more robust equation of state. The incompressibility of the liquids assumption is reasonable except at high curvatures, which correspond to high Laplace pressures. When a liquid is in a high negative pressure state, the molar volume can increase up to 17%, negating the incompressibility assumption

[28], [46]. Models accounting for the different types of non-ideal behavior are illustrated in references [28], [43], [46].

It is common to assume that the bulk properties of the liquid or vapor apply at all levels of saturation and curvatures. However, at low saturation levels the Kelvin radius is on the order of a few molecular radii. For example, at 20 °C and 50% RH, the Kelvin radius for water is 0.8 nm [25]. With an effective diameter of approximately .37 nm [25], water must form a meniscus with less than 3 molecules. Such a constraint considerably stretches the intra- and intermolecular bonds of water. Furthermore, theory [28], [35] and simulations have shown that as the saturation level decreases the change in the surface tension can be significant, especially at saturations near the spinodal [31], [47]. Therefore, assuming that the bulk surface tension or bulk molar volumes are constant at all saturations is also tenuous. Indeed a constant surface tension is neither required nor implied in derivation of the Kelvin equation and its proper application must utilize the true surface tension for a given curvature and saturation level.

Finally, the traditional form of the Kelvin equation is somewhat misleading. Mathematically, it suggests that the curvature of the interface may be obtained for all relative vapor pressures. Yet, at low relative vapor pressures, a condensed phase may not exist, meaning that the Kelvin equation is only applicable for relative vapor pressures between the spinodal and the binodal. Hence predictions involving capillary forces at RH < 20%, are likely not from liquid menisci.

In summary, the *traditional* Kelvin equation includes, explicitly or inherently, these assumptions:

(1) A pure-component system

(2) Mechanical equilibrium such that the Young-Laplace equation applies (*i.e.*, the system must be static).

(3) Thermal equilibrium.

(4) An ideal vapor.

(5) An incompressible liquid or solid.

(6) The coexistence of the two phases at the given temperature for all relative vapor pressures.

1.4.3 General Capillary Force Model

A meniscus minimizes its surface excess energy by forming a curved liquid-vapor interface between two solid surfaces. This results in a more stable system and increases the work necessary to separate the two solid bodies. Hence the adhesion between two solid surfaces is greater because of the meniscus. The increase in adhesion due to these menisci are capillary forces.

There are two components to the capillary force: the capillary pressure force F_P and the surface tension force F_S. The capillary pressure force is the Laplace pressure as described by the Young-Laplace and Kelvin equations multiplied by the wetted area of the solid surfaces:

$$F_p = A_w \Delta P = A_w (p_L - p_G). \tag{1.22}$$

This term is typically dominated by the magnitude of the pressure inside the meniscus and not the ambient pressure [48]. The force that pulls the contact line between the meniscus and the upper solid toward the contact line between the meniscus and the lower solid is the surface tension force [48] and is characterized by the Young equation and the contact angle [49]. F_S is determined by multiplying the wetted perimeter l_w (the three-phase contact line) by the component of the surface tension normal to the two interacting surfaces [48]:

$$F_S = \gamma_{LV} l_w \cos \phi_n \tag{1.23}$$

where ϕ_n is the angle of inclination of the liquid meniscus from the normal (vertical) direction [16] (Figure 1.6).

A general form of the total capillary force F_C is then [14], [16], [48]

$$F_C = F_P + F_S = A_w \Delta P + \gamma_{LV} l_w \cos \phi_n \, . \tag{1.24}$$

F_S is often neglected in the treatment of capillary forces because it is typically much smaller than F_P for lyophilic surfaces [25]. Yet equation (1.24) is the basic form from which analytical capillary force equations are derived (see Section 1.6).

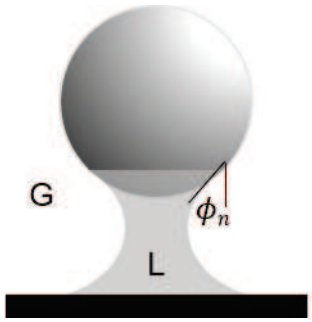

Figure 1.6 Angle of inclination, ϕ_n, of the liquid meniscus between solid surfaces.

1.5 Experimental Considerations for Measuring Capillary Forces

The following section has been published in *Particulate Science and Technology* DOI:10.1080/02726351.2015.1045641 [50].

Capillary forces between particles and surfaces were first characterized with freely-suspended spherical beads (0.03-0.10 cm in radius) and flat, vertical surfaces in a controlled environment [51]. This landmark study indicated that the magnitude of the capillary force depended on the size of the sphere, the surface roughness of the flat plate, the type of condensed vapor, and the lyophilic nature of the surfaces [51]. Since then, more sophisticated techniques involving centrifuges, surface force apparatuses (SFA), and atomic force microscopes (AFM) have been employed to study these same issues in capillarity between solid surfaces.

Though useful in establishing many aspects of capillarity and particle adhesion, the centrifuge technique and the SFA experiments are limited. For example, it is not possible to control the humidity in most centrifuges, and hence this technique is used only sparingly [52]. Moreover, SFA is restricted to substances that can coat highly curved, crossed-cylinders such as mica and gold. Some important results in relation to

surface contamination issues from SFA studies are discussed (see Section 1.5.2), but an extensive review on capillary forces in SFA is not, though it is also commonly used to study capillary forces [17], [53]. Therefore, only AFM studies are considered in this review because of the ease of environmental control and the variety of particles and surfaces that can be investigated through colloidal probe microscopy.

To measure adhesion forces between probes or colloidal particles and surfaces via AFM, the surface is first mounted on a piezoelectric column. This column can move with nanoscale precision in the X, Y, or Z planes based on an applied voltage. Then the surface is lifted toward the probe or particle which has been pre-mounted onto a flexible lever (known as a cantilever) with a known spring constant. As the surface approaches the probe, the attractive forces between the surface and the probe will eventually overcome the restorative force of the cantilever. This causes the cantilever to deflect downward and is known as “snap in” to contact (Figure 1.7, location A). The surface continues to rise for a fixed distance causing the cantilever to deflect in the positive z-direction past its nominal position (location B). Next the surface is lowered and the cantilever deflects in the negative z- direction until the adhesion forces between the probe or particle and the surface are overcome by the restorative force of the cantilever (“snap out” of contact, location C). The difference between the nominal deflection of the cantilever and its minimum negative deflection, represents the amount of adhesion between the probe and the surface. Assuming Hookean mechanics, the adhesion is quantified by multiplying the amount of deflection by the spring constant of the cantilever. Utilizing this method, the effect of water vapor on the adhesion can also be

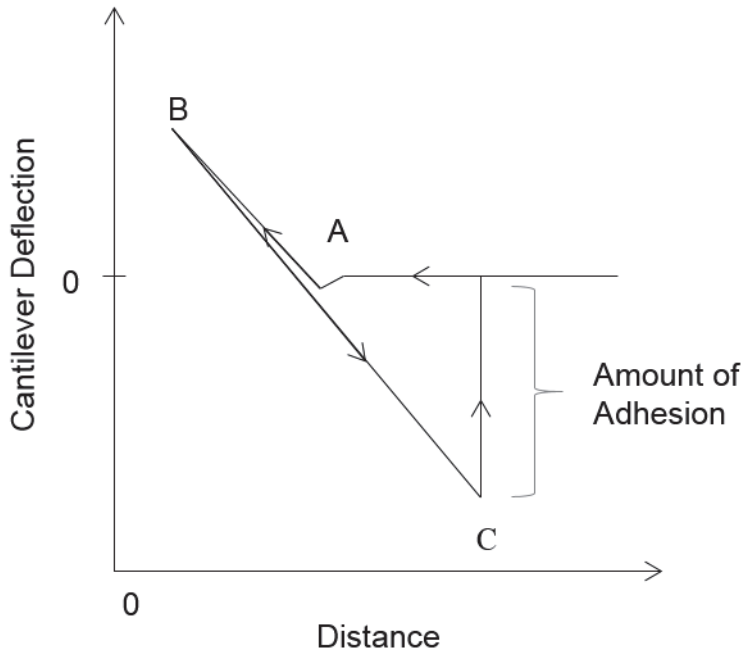

Figure 1.7 AFM cantilever deflection as a function of vertical displacement of the surface during a typical AFM force measurement. The cantilever jumps into contact at point A, reaches a maximum positive deflection at point B, and jumps out of contact with the surface at point C.

determined via AFM by varying the RH around the probe and the surface in a controlled manner. For more details on AFM operation see reference [54].

Accurately accounting for the capillary force in an experimental setting is challenging. The majority of capillary force models assume ideal geometries, smooth surfaces, and/or the unqualified application of the Kelvin equation [47], [48], [55]–[67]. While these models establish trends, they often only qualitatively predict the capillary forces. This is because the strength of the capillary force in reality depends on the particle's and surface's roughness, deformability, lyophilic nature, and shape and size as well as the time required to form a stable meniscus. Expectedly, the relationship among

these parameters and the capillary force is complex and interdependent as is discussed in the following sections.

1.5.1 Hydrophilicity

The hydrophilic nature of adhering surfaces determines the existence of capillary forces. For example, when either or both of the surfaces are hydrophobic, the force of adhesion is generally independent of RH [55], [68]–[75]. These results suggest that the hydrophobicity inhibits capillary condensation and all of the attractive forces can be attributed to other factors such as vdW interactions and surface topography. Contrastingly, when both surfaces are hydrophilic and liquid bridges form more readily, the force of adhesion can monotonically increase, monotonically decrease, exhibit a maximum, step-wise increase, or remain constant as the RH increases (see Figure 1.8 for representative plots of these trends). Therefore, the hydrophilic surfaces clearly enable capillary forces to be a contributing factor to the overall adhesion. Yet with such a variety of observable trends, it is reasonable to conclude that surface hydrophilicity merely creates the circumstances necessary for the existence of capillary forces, but is insufficient to describe how these forces will behave with a change in RH.

To further illustrate this point, it is instructive to analyze the studies which investigate how the adhesion of two hydrophilic surfaces depends on varying RH environments. Due to the wealth of information available on this topic, an attempt has not been made to be comprehensive, but rather to be thoroughly representative of trends and experimental procedures. Again, only AFM studies have been compared, with the

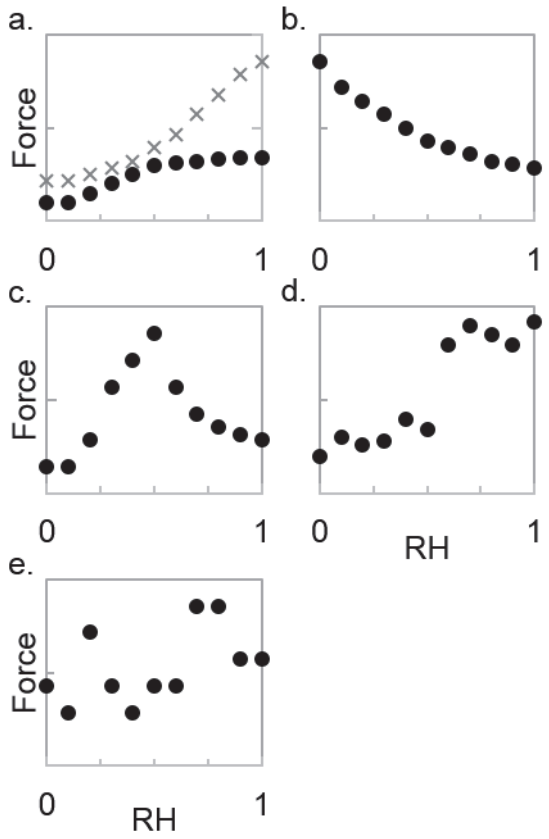

Figure 1.8 Trends of force vs. RH curves typically obtained via AFM: a. monotonic increase (two different types); b. monotonic decrease; c. maximum; d. step-wise increase; and e. force is independent of RH.

exception of the fundamental study of McFarlane and Tabor [51]. Additionally, only studies involving hydrophilic surfaces are being analyzed (with the exception of CaF_2 which will be discussed later) because hydrophobic surfaces tend to be consistently independent of changes in RH.

In Tables 1.1-1.8, experimental details and results of AFM force experiments at varying RH levels are presented. These results are separated by the substrate material and then categorized by the tip material in alphabetical order. Eight substrates are represented: aluminum oxide (Al_2O_3), gold-coated mica, calcium fluoride (CaF_2), mica,

silicon wafers (Si), silicon dioxide/quartz/glass (SiO_2), stainless steel, and titanium dioxide (TiO_2). Of these eight, mica, Si, and SiO_2 are the most commonly studied. There is some ambiguity with Si and SiO_2 since Si readily forms an oxide layer, but if the study mentions a silicon wafer, it has been characterized under Si. Otherwise the study has been characterized under SiO_2. The AFM tips utilized in these studies are comprised of Si, silicon nitride (Si_3N_4), gold-coated Si_3N_4, SiO_2, and TiO_2. (See Table 1.9 for the sessile-drop contact angles of water against each of the substrate and tip materials). The reported radius of curvature (ROC) of the tip or the colloidal probe (in nm) has been used to normalize the adhesion data which is generally size-dependent and allows for the comparison between AFM tips and colloidal probes. Note that the magnitude of the normalized adhesion force for large probes and AFM tips is generally 0.10–1.0 nN nm^{-1}. When a range is listed for the ROC, the mean ROC is used to normalize the adhesion data. The number of force measurements (FM) taken at each RH level and the number of different locations sampled have also been listed for each study. Finally, the range of RH levels investigated, the range of the normalized adhesion forces, and the observed adhesion trends with changes in RH are reported. It is important to note that the values listed for the normalized forces are approximate, but the trends are not. These are followed by some explanatory notes and the reference. Any information that is unknown or unclear is marked with a U.

Table 1.1 Experimental AFM force measurements (FM) of silicon against aluminum oxide. U: Unknown.

Al_2O_3 and Al_2O_3-HfO_2								
Tip	**ROC (nm)**	**# of FM**	**# of Loc.**	**RH range**	**Normalized force range (nN nm^{-1})**	**Observed Trend**	**Notes**	**Ref.**
Si	12	U	U	0.20-0.70	1.5-6.5	Monotonic increase		[76]

Table 1.2 Experimental AFM force measurements (FM) of silicon nitride tips against gold-coated mica. U: Unknown.

Au-coated Mica								
Tip	**ROC (nm)**	**# of FM**	**# of Loc.**	**RH range**	**Normalized force range (nN nm^{-1})**	**Observed Trend**	**Notes**	**Ref.**
Si_3N_4	10	U	U	0.0-0.72	0.35-0.47	Maximum around 0.4 RH	Measurements under UHV were conducted and produced lower results than the 0 RH value. Retraction speed: 150 nm s^{-1}	[77]

Table 1.3 Experimental AFM force measurements (FM) of silicon or silicon nitride tips against calcium fluoride. U: Unknown.

CaF_2								
Tip	**ROC (nm)**	**# of FM**	**# of Loc.**	**RH range**	**Normalized force range (nN nm^{-1})**	**Observed Trend**	**Notes**	**Ref.**
Si or Si_3N_4	10-20	U	U	0.05-0.85	0.47-1.43	Maximum around 0.2 RH	Diffusion of ions from the surfaces into a meniscus can affect the surface tension of the condensing fluid.	[72]
U	U	Numerous	U	0.20-0.80	3.5-4.0	Independent of RH		[78]

Table 1.4 Experimental AFM force measurements (FM) of various AFM tips against mica. U: Unknown.

Mica								
Tip	**ROC (nm)**	**# of FM**	**# of Loc.**	**RH range**	**Normalized force range (nN nm^{-1})**	**Observed Trend**	**Notes**	**Ref.**
Au-coated Si_3N_4	100	Several hundred	U	0.25-0.85	1.7-2.1	Independent of RH		[73]
Si	2 7	U	U	0.05-1.0	0.20-1.3	Monotonic decrease		[63]
	7-20	U	U	0.05-1.0	0.89-1.4	Maximum between 0.15-0.25 RH		[63]
Si_3N_4	20	U	U	0.15-0.95	0.10-0.40	Maximum between 0.30-0.40 RH	Found a similar trend with tips of different radii	[6]
	10-100	U	U	0.10-0.42	1.2-1.8	Monotonic increase		[6]
	20-40	3 / RH	U	0.0-0.75	0.20-0.40	Step-wise increase. The transition occurs between 0.20-0.60 RH.	Used a polonium wand to eliminate electrostatic effects	[7]
	10	~1600/ experiment	U	0.0-0.70	8-11	Maximum between 0.20-0.40 RH	Noted that Force-RH trends differed from experiment to experiment. Both maxima and monotonic increases were observed. Changed RH quickly: ~ 15 min/experiment.	[55]

Table 1.4. Continued

Mica								
Tip	**ROC (nm)**	**# of FM**	**# of Loc.**	**RH range**	**Normalized force range (nN nm^{-1})**	**Observed Trend**	**Notes**	**Ref.**
Si_3N_4	15	U	U	0.0-0.75	0.30-0.70	Step-wise increase. Transition occurs between 0.20-0.50 RH.		[8]
	15-25	U	U	0.05-1.0	0.70-1.4	Maximum between 0.20-0.80 RH.	Always observed this behavior	[63]
	100	Several hundred	U	0.25-0.85	0.43-0.61	Independent of RH		[73]
SiO_2	8000	U	U	0.0-0.85	0.40-0.80	Monotonic increase	Observed a difference between hydrophilic and hydrophobic surfaces and differences between AFM tips and colloidal probes	[79]
U	90	U	U	0.0-0.85	0.40-1.0	Maximum between 0.50-0.60 RH	Observed a difference between hydrophilic and hydrophobic surfaces and differences between AFM tips and colloidal probes	[79]
U	U	Numerous	U	0.20-0.80	6.5-7.2	Independent of RH		[78]

Table 1.5 Experimental AFM force measurements (FM) of various AFM tips against silicon wafers. U: Unknown.

Si Wafer								
Tip	**ROC (nm)**	**# of FM**	**# of Loc.**	**RH range**	**Normalized force range (nN nm^{-1})**	**Observed Trend**	**Notes**	**Ref.**
Si	20	4/RH	1/RH	0.0-0.90	0.50-2.3	Maximum around 0.60-0.80 RH	Observed a repeatable and reversible trend	[70]
	450 900	20/RH	U	0.0-0.70	1.3-1.9 5.2-8.0	Monotonic increase	Used flat tips parallel to the smooth Si Wafer surface. In this arrangement their results were consistently reproducible. Found that force depends on tip shape, RH and piezo speed.	[80]
	2000	250/RH	10 / RH	0.0-0.80	2.4-3.6 0.040-0.19	Maximum around 0.70 RH	Found that the smooth Si surface is able to consistently similar results even over the course of several months. Used flat tips parallel to smooth and etched Si surfaces.	[81]
	15	U	U	0.0-0.90	1.5-7.0	Maximum around 0.30 RH	Observed ice-like water in the low RH regime, which is hypothesized to cause the maximum in the adhesion.	[66]
	135	1024-4096 on a 500 x 500 nm^2 grid		0.20-1.0	0.77-1.2	Maximum around 0.70 RH	This trend was observed for increasing and decreasing humidity	[82]
	25	U	U	0.0-0.40	0.60-1.0	Maximum around 0.30 RH		[83]

Table 1.5. Continued

Si Wafer								
Tip	**ROC (nm)**	**# of FM**	**# of Loc.**	**RH range**	**Normalized force range (nN nm^{-1})**	**Observed Trend**	**Notes**	**Ref.**
Si or Si_3N_4	10-20	U	U	0.05-0.90	0.25-1.45	Maximum between 0.40-0.80 RH		[72]
Si_3N_4	10	U	U	0.0-0.72	0.20-0.60	Monotonic increase	Measurements under UHV were conducted and produced lower results than the 0.0 RH value.	[77]
	10	~1600	U	0.10-1.0	11-14	Maximum between 0.60-0.80 RH	Noted that Force-RH trends differed from experiment to experiment. Both maxima and monotonic increases were observed. Changed RH quite quickly ~ 15 min/experiment	[55]
	10 22 50	25/RH	3 / RH	0.30-0.70	0.90-1.3 0.90 1.5	Monotonic increase	Observed a linear dependence on the size of the tip and the adhesion at 0.30 RH	[84]
	50	U	U	0.0-0.80	0.50-2.3	Step-wise increase with a transition around 0.60 RH		[74]

Table 1.5 Continued

Si Wafer								
Tip	**ROC (nm)**	**# of FM**	**# of Loc.**	**RH range**	**Normalized force range (nN nm^{-1})**	**Observed Trend**	**Notes**	**Ref.**
Si_3N_4	28-43	1024 -4096 on a 500 x 500 nm^2 grid		0.15-1.0 0.20-1.0	0.40 – 1.6 0.99-1.6	Monotonic increase Maximum around 0.25 RH with a sudden increase at 1.0 RH	The shape of the cantilever changes based on the RH of the system. The tip ROC can either increase in size (most common) or decrease.	[82]
SiO_2	3700	U	U	0.12-0.55	0.0033-0.0084	Monotonic increase		[72]
	3800 6900 9500 14500	U	U	0.0-0.65	0.0035-0.030	Step-wise increase with a transition around 0.60 RH	Noted that the size of the sphere did not affect the adhesion force at a given humidity. However, the trend might change when RH > 0.65.	[74]

Table 1.6 Experimental AFM force measurements (FM) of various AFM tips against silicon dioxide and/or glass. U: Unknown. NA: Not applicable.

SiO_2 or Glass								
Tip	**ROC (nm)**	**# of FM**	**# of Loc.**	**RH range**	**Normalized force range (nN nm^{-1})**	**Observed Trend**	**Notes**	**Ref.**
Si	20	4/RH	1/RH	0.0-0.90	0.70-3.0	Monotonic increase	Did not observe hysteresis and found that the RH equilibrated in about 10 min.	[70]
	35	200/RH	2/RH	0.0-0.90	0.3-0.6	Monotonic increase	Exhibited a minimum threshold for capillary forces around 0.25 RH	[48], [85]
	200	16/location	16 / RH	0.24-0.94	0.0050-.50	Decrease from 0.20-0.80 and then a slight increase to 0.95 RH	Demonstrated that the force depends on the ROC of the tip	[86]
Si_3N_4	~100	80/RH	80 / RH	0.05-1.0	0.30-0.75	Maximum around 0.60-0.80 RH	Achieved a Gaussian distribution of forces at each RH	[87]
	U	U	U	0.10-0.55	1.5-2.5	Monotonic increase		[88]
SiO_2	15500	U	U	0.0-0.95	0.060-0.39	Step-wise increase with transition between 0.30-0.70 RH		[89]
	8000	U	U	0.0-0.85	0.60-0.80	Monotonic increase	Observe a difference between hydrophilic and hydrophobic surfaces and differences between AFM tips and colloidal probes	[79]

Table 1.6. Continued

SiO_2 or Glass								
Tip	**ROC (nm)**	**# of FM**	**# of Loc.**	**RH range**	**Normalized force range (nN nm^{-1})**	**Observed Trend**	**Notes**	**Ref.**
SiO_2	1000	200/RH	2/RH	0.0-0.80	0.28-0.48	Monotonic increase	Exhibited a minimum threshold for capillary forces around 0.30 RH	[85]
	2500	200/RH	2/RH	0.0-0.80	0.27-0.33	Monotonic increase	Exhibited a minimum threshold for capillary forces around 0.40 RH	[85]
	35	200/RH	2/RH	0.0-0.85	1.3-1.6	Monotonic increase	Blunted tip	[85]
	120	200/RH	2/RH	0.0-0.80	1.2-1.4	Monotonic increase	Blunted tip	[85]
	10000	U	U	0.04-0.90	0.050-0.33	Step-wise increase with transition above 0.60 RH		[90]
	.2 – 1 mm	NA	NA	0.40-1.0	U	Monotonic increase	Studied the adhesion between a suspended glass bead and a glass surface. This was not an AFM study.	[51]
TiO_2	45	200/RH	2/RH	0.0-0.80	0.18-0.26	Monotonic increase	Exhibited a minimum threshold for capillary forces around 0.45 RH	[85]

Table 1.6 Continued

SiO_2 or Glass								
Tip	**ROC (nm)**	**# of FM**	**# of Loc.**	**RH range**	**Normalized force range ($nN\ nm^{-1}$)**	**Observed Trend**	**Notes**	**Ref.**
U	90	U	U	0.0-0.85	0.55-2.6	Monotonic increase	Observe a difference between hydrophilic and hydrophobic surfaces and differences between AFM tips and colloidal probes	[79]
U	10-25	U	U	0.04-0.90	6.0-20	Step-wise increase with transition above 0.60 RH		[90]

Table 1.7 Experimental AFM force measurements (FM) of silicon nitride tips against stainless steel.

Stainless Steel								
Tip	**ROC (nm)**	**# of FM**	**# of Loc.**	**RH range**	**Normalized force range (nN nm^{-1})**	**Observed Trend**	**Notes**	**Ref.**
Si_3N_4	20	1200/RH	12/RH	0.15-0.65	0.17-1.6	Maximum between 0.35-0.45 RH		[69]

Table 1.8 Experimental AFM force measurements (FM) of various tips against titanium dioxide.

TiO_2								
Tip	**ROC (nm)**	**# of FM**	**# of Loc.**	**RH range**	**Normalized force range (nN nm^{-1})**	**Observed Trend**	**Notes**	**Ref.**
SiO_2	40	200/RH	2/RH	0.0-0.85	0.16-0.43	Monotonic increase		[85]
TiO_2	65	200/RH	2/RH	0.0-0.85	0.3-0.36	Monotonic increase	Exhibited a minimum threshold for capillary forces around 0.45 RH	[85]

Table 1.9 Experimental water contact angles (sessile-drop method) against various substrates

Substrate	Contact Angle (°)	Ref.
Al_2O_3	27-93	[91]
Au	0	[73]
CaF_2	95, 103	[92], [93]
Mica	0	[7]
Si	0-25	[7]
Si_3N_4	3	[7]
SiO_2	10-50	[7]
Stainless Steel	50	[69]
TiO_2	80	[85]

Upon inspection, Tables 1.1-1.8 show inconsistent experimental trends of the capillary force as a function of RH among the different researchers and studies. For example, the capillary force can exhibit a maximum around 0.25 [82] or 0.60-0.80 [55] or monotonically increase [82], [84] with varying magnitudes of adhesion as RH increases for a Si_3N_4 tip and a Si substrate (Table 1.5). In general, the purpose of each study and the consequent differences in experimental preparation and execution primarily contributes to these inconsistencies. Such details must be considered in their proper context before any conclusions are drawn concerning the influence of RH on capillary forces. In outlining these differences, the purpose is to illustrate that the adhesion data presented in the literature represents real trends. However, that one trend from one study represents the true influence of capillary forces for a particular tip-substrate combination

is unlikely, especially because some studies are less carefully executed and reported than others.

For example, three studies do not explicitly mention the AFM tip material [72], [79], [90], which is key to understanding both the vdW interaction between the two surfaces and the hydrophilic nature of the tip. Another does not mention the size of the tip [88] (Table 1.6), so the results cannot easily be compared or extended to other systems. Moreover, RH is controlled using ultra high vacuums [77], fluid cells [55], and/or humidity chambers encasing the AFM [69]. Each method results in uncertainty around the true RH, especially in the vicinity of the measurement. These different methods of environmental control contribute to the scatter of the data.

One of the most prevalent issues among the different studies is that of the statistical validity of the force-RH curves presented. For a study to be statistically arguable, there must be a large enough sample of the population to achieve a normal distribution of forces about the mean. Such a sampling in AFM studies is difficult because a 10 x 10 μm^2 area of a circular substrate with a diameter of 1 cm represents only 0.000032% of the total substrate area. It can be argued that a random location on the substrate likely represents the substrate as a whole chosen at random, but this assumption should be verified by testing different locations. Certainly it is obvious that only taking a few force measurements at a limited number of locations on a surface is insufficient to claim that the force-RH curve is representative of a tip-substrate combination. Therefore, it is necessary to maximize the number of force measurements and locations sampled on a given substrate, while mitigating tip damage.

Unfortunately, 14 of the 28 studies listed in Tables 1.1-1.8 do not report how many force curves at how many different locations are measured [6], [8], [63], [66], [72], [74], [76]–[79], [83], [88]–[90], and therefore do not identify outliers or the amount of random error within the data. Of the remaining 14 studies, the number of force measurements and locations ranges from 3 force curves per RH [7] to "several hundred" [73] to 1024-4096 force measurements on a 500 x 500 nm^2 grid [82] (see Tables 1.1-1.8). While statistical methods are infrequently applied to these data, a few studies mention reproducibility of the experiments [63], [70], [80], [82] even by testing different locations [81]. In fact, Çolak *et. al.*, [81] have noted that the adhesion forces can be log-normally distributed by taking 250 force measurements over 10 different surface locations. While Xiao and Qian [87] have shown a normal distribution of adhesion forces per RH by taking 80 force measurements at 80 different locations at every RH. Interestingly, the normal distribution is only reported for a hydrophobic surface, and even though it is implied that a similar distribution is observed for hydrophilic surfaces, no data is presented to confirm that is the case [87]. Still, these two studies indicate that many force curves and many locations on a given surface must be probed to reasonably claim that a given force is representative for a given tip-substrate combination at a given RH. This observation is important to note for future studies so the data may be properly interpreted and presented in a statistically valid context.

Even with a large sample size, the trends may yet be difficult to establish because Farshchi-Tabrizia *et. al.*, [55] have noted that the force-RH trends are not always consistent across replicated experiments. When approximately 1600 force measurements from low to high RH and back again are obtained in about 15 minutes, maxima or

monotonic increases in the force-RH trends are typically observed. Yet these trends are only "tendencies" for a given tip-substrate combination and can change from experiment to experiment, or even within an experiment [55]. As a side note, it should be noted that the magnitude of the normalized adhesion forces in [55] are an order of magnitude greater than the majority of other studies. This could be a result of the speed at which the measurements have been taken and/or non-equilibrium conditions due to rapid RH adjustments. Nevertheless, this study shows that even with large sample populations and experimental replicates the exact trends seem to largely depend on the specific experimental setup than on properties inherent to the system.

As a result of the dependence on experimental setup and execution, even the studies with better-documented methods sections report conflicting results for the same tip-substrate combinations. For example, the capillary force between a Si_3N_4 tip and mica is independent of RH [73], has a step-wise increase between 0.20-0.60 RH [7], or has a maximum between 0.20-0.40 RH [55] (Table 1.4). The capillary force between a Si tip and SiO_2 increases monotonically [48], [70], or decreases monotonically [86] (Table 1.6). There is one exception. The trend of the capillary forces as RH increases between a Si tip and a Si surface consistently produces a maximum in adhesion around 0.70 RH [70], [80]–[82] (Table 1.5). Indeed, the reproducibility of the Si AFM tip against a smooth Si surface has been noted [81] and is probably the best system for experimentally investigating the influence of RH on capillary forces.

In summary, the hydrophilicity of the adhering surfaces allows for the presence of a capillary force, but its dependence on RH is heavily influenced by other experimental

factors, such as ionic diffusion into liquid bridges [53], local roughness [81], deformation [55], tip size and shape, and the kinetics of meniscus formation.

1.5.2 Ionic Diffusion

A common assumption in capillary force studies is that the liquid bridge is a one component system (*e.g.*, pure water). However, labile ions from ionic substrates or surface contaminants can diffuse into a liquid bridge and thereby alter the properties of the condensed vapor, such as the surface tension.

This effect is particularly significant for capillary studies involving muscovite mica ($KAl_2(Si_3Al)O_{10}(OH,F)_2$) substrates. Mica is an ideal substrate to study moisture effects in the absence of surface roughness because it cleaves easily and leaves a molecularly smooth surface. Yet, the presence of deposited, involatile material after evaporation [94] and a significant shift in the refractive index of water in these liquid bridges [21], [95] in SFA studies suggest that dissolved surface contaminants are present and can significantly change bulk water properties. For mica cleaved in air, it is suspected that these surface contaminants are water-labile potassium salts [94] and are the cause of sizable experimental deviations from theoretical predictions [6], [21], [53], [94]. Once these surface contaminants are removed by rinsing the mica in dilute acid, experimental results align properly with theoretical predictions of the Kelvin equation [53]. Therefore, it is necessary to remove the surface contaminants caused by cleaving the mica in capillary force experiments. Each of the studies in Table 1.4 mention that the mica has been freshly cleaved prior to measurement, but none state that the mica has also been

rinsed. Thus part of the discrepancies in force-RH trends and magnitudes among these studies could be because of ionic diffusion into the liquid bridges.

The leaching of ions and surface contaminants into liquid bridges has also been observed for silica [96] and CaF_2 [72]. CaF_2 is an interesting case because it is a hydrophobic surface with a contact angle of 90-103° (Table 1.9) [92], [93]. Even though ion transport is limited, the small amount of surface ions in the liquid bridge alter the surface tension of the bulk liquid. Presumably this alteration allows for a maximum of adhesion to occur around 0.20 RH [72] (Table 1.3), a trend typically reserved for hydrophilic surfaces. Therefore, the diffusion of ions into the liquid bridge can even cause a hydrophobic surface to exhibit hydrophilic adhesion tendencies. More generally, the leaching of labile surface ions into liquid bridges and the consequent altering of pure component properties of the bridge may explain how capillary forces can exhibit maxima in low RH regimes on a variety of surfaces (Tables 3, 5, and 7). (Note that Tang *et. al*., [78] have indicated that the force-RH curve on CaF_2 is independent of RH, which is consistent with a hydrophobic surface. However, their force-RH curve of mica is unexpectedly also independent of RH and their methods are ambiguous, which suggests questionable results). Because of this leaching effect, care should be taken to remove surface contaminants and/or inhibit ionic diffusion when studying capillary forces via SFA or AFM.

1.5.3 Surface Roughness

The surface roughness of the particle and the substrate is often a controlling factor in the strength of adhesion. This is true for both the vdW and the capillary forces because the surface roughness determines the degree to which two adhering surfaces complement each other. The lower the complementarity between the two surfaces, the lower the vdW force because the actual area of contact has decreased. The capillary force also decreases because the nano-asperities limit the size of the menisci, at least until the RH reaches a critical value at which the condensed moisture encompasses the nano-asperities [57], [70], [97]–[99]. Indeed, if the complementarity of the particle and the substrate is low, the force of adhesion will fall well below theoretical predictions [70].

This has been shown experimentally. AFM force measurements between a smooth, silica sphere (10 μm in radius with a roughness root mean square (R_{rms}) ca. 0.2 nm) and a smooth silicon wafer (R_{rms} ca. 0.2 nm) produced 1.3 μN at 0.65 RH and 1.0 μN at 0.30 RH. The effect of surface roughness was tested by depositing titanium onto the silicon wafer surface through chemical vapor deposition. Adhesion forces of the silica sphere against these regularly-shaped, rough surfaces decreased to ~0.25 μN at both 0.65 and 0.30 RH for a surface with R_{rms} of ca. 4 nm [57]. A similar decrease in the capillary force with increasing surface roughness has been observed for substrate R_{rms} values ranging from 0.2 to 0.7 nm [100] and for cumulative particle and substrate R_{rms} values ranging from 1 to 14 nm [81], [98], [99].

Due to the apparent relationship between R_{rms} and the force of adhesion, models relating the two quantities have been obtained [57], [100], but are of limited use since the

R_{rms} parameter is not a comprehensive description of the surface roughness. That a rougher surface will have a higher R_{rms} value is generally true, but the average asperity height does not capture the average distance between peaks of similar height or surface defects, such as crevices and plateaus. As was demonstrated in a recent microcantilever study [97], it is not simply that the surface asperities have the correct average height, but how and which asperities are in contact that is most important. In other words, the actual area of contact must be recreated accurately (i.e., the two rough surfaces are properly represented *and* aligned) in order to qualitatively predict the force of adhesion. Thus, for regularly-shaped, rough surfaces, surface defects and orientation are less important than the average asperity height or R_{rms} and it is reasonable to use R_{rms} to describe how surface roughness changes forces of adhesion. However, for an *irregularly*-shaped, rough surface, which is much more common, surface defects and orientation dominate, rendering R_{rms} inadequate to predict force behavior by itself. Hence it is requisite to develop methods which accurately account for the actual area of contact between the two surfaces.

1.5.4 Deformation

To model the contact area, the rigidity of the system or its proclivity toward deformation must be properly understood as well. Less rigid systems will deform more readily to a strong attractive force than will a stiff system. This means that an increase in the capillary force will likely increase the amount of deformation in the system, though it will likely influence the strength of the vdW attraction as well, which could lead to more

deformation and a wider, more stable capillary bridge. In the end, the system will deform until an equilibrium between the attractive and repulsive forces is reached, but it must be noted that it is difficult to know the capillary force without the deformation and vice versa. It is reasonable to expect, however, that the capillary force will likely be larger in less rigid, lyophilic systems than in more rigid, lyophilic ones. This is because the actual area of contact will increase in the less rigid system and will encourage larger, more stable liquid bridges to form.

The interdependence of the capillary forces and deformation has been predicted using the Hertzian [55], [101], Greenwood-Williamson models [59], [101], and the Extended-Maugis-Dugdale elastic theory [59]. The surfaces are allowed to be smooth; nanopatterned with spherical [55], [101] and conical [55] asperities with uniform [55], [101] or non-uniform [101] heights; a single spherical asperity [59]; or randomly rough [59], [101]. These surfaces and models reveal that the capillary force increases surface deformation which in turn increases the overall capillary and other attractive forces [55], [59], [101]. Thus models that do not allow surface deformation often under-predict the true contribution of capillary forces in particle adhesion [59].

1.5.5 Particle Shape and Size

The dependence of the capillary force on the shape and size of the particle can be mitigated by normalizing the force by the ROC of the tip, but not eliminated. First, the shape of the AFM tip must be properly represented by a sphere or circle for the normalization by the ROC to be meaningful. Since the shape of the AFM tip or colloidal

probe can easily change through the course of the experiment [55], this assumption may not be accurate for all measurements. Secondly, smaller, sharper tips are more susceptible to local surface roughness than larger, flat ones [80], [81], thereby producing more scatter in the data. Also, some of the large SiO_2 colloidal probes exhibit normalized forces that are well below the typical values (~ 0.003) [72], [74], presumably because the adhesion is not governed by the macroscopic shape, but by the nanoscale roughness on the surface of the particle, thus skewing the normalization. In summary, the size (*i.e.*, mass) of the particle will dictate the general magnitude of adhesion; the local roughness and shape will dictate the actual force measurement.

1.5.6 Kinetics of Meniscus Formation

The filling of a meniscus to stability is governed by bulk or Knudsen diffusion [102], [103], liquid transport through an adsorbed liquid film [104], or liquid drainage of the viscous condensate between the two solids [104]. Whatever the governing mechanism of meniscus formation, it has been shown theoretically and experimentally that smaller particles/asperities have a lower kinetic barrier towards meniscus formation. For example, colloidal probes (*i.e.*, micrometer-sized particles) require contact times longer than 1 s and can require contact times on the order of 1000 s [6], [56], [98], [104] to reach the equilibrium capillary force. Sharp AFM probes (ROC < 50 nm), on the other hand, only require contact times on the order of milliseconds [14], [56], [79]. The relationship between the size of the particle and the required contact time is a result of the time

required to fill the meniscus to its equilibrium volume [56], [104]. This volume is larger for larger particles or asperities.

As a result, the kinetics of meniscus formation between two surfaces is not negligible in capillary force studies. For AFM experiments, this means that force-curves must be conducted slowly to obtain the equilibrium capillary force. The typical acquisition range for conventional force-curve measurements (colloidal probes) is between 0.01 to 10 s [105]. Moreover, force-curve acquisition speeds are between 0.01 – 1 μs for dynamic AFM modes (*i.e.*, tapping mode) and 0.01 – 1 ms for force-curve mapping [105]. Thus, the acquisition speed must be pre-determined based on the size of the particle/tip and the acquisition method so that the time-independent and equilibrium assumptions may be employed. Longer contact times unfortunately may contribute to surface modification of the probe or surface as indicated in the previous sections. As such, differences in the sampling rates among the studies listed in Tables 1.1-1.8, may also be a significant source of error contributing to the discrepancies among the results.

1.5.7 Summary

In summary, AFM experimental studies suggest that the hydrophilicity of the adhering surfaces merely allows for the presence of a capillary force, but does not dictate its dependence on RH. Certainly, experimental factors such as the tip changing shape throughout the experiment [55] and the build-up of adsorbed water on the hydrophilic surfaces [66], [106] affect the outcome of AFM studies and must be recognized as inherent experimental error. Yet other physical factors like ionic diffusion into liquid

bridges [53], local roughness [81], deformation [55], tip size and shape [63], surface heterogeneity [14], [107], local temperature fluctuations [67], kinetics [67], and non-equilibration [79], [108] also affect (if not govern) these trends.

1.6 Analytical Capillary Force Models

For static menisci in thermal, mechanical, and chemical equilibrium, that exhibit bulk fluid properties, analytical models utilizing the Young-Laplace, Young, and Kelvin equations have considerable utility in predicting capillary forces. Butt and Kappl [14] provide an excellent review of equations regarding idealized systems, including plane-plane, sphere-plane, cone-plane, sphere-sphere, and cone-cone systems. In section 1.6.1, the capillary force is derived for the simple case of axisymmetric, smooth parallel planes to demonstrate the technique of deriving capillary forces from geometrical arguments. This is followed by a short discussion of the capillary force equations for the more common sphere-plane system and its most common forms. Section 1.6.2 presents how the governing equations have been modified to account for non-idealities in particle adhesion such as the surface roughness.

1.6.1 Models Assuming Ideal Surfaces

1.6.1.1 Parallel planes

Consider two smooth, parallel planes comprising of different materials separated by a concave, liquid bridge with separation h (Figure 1.9). The system is axisymmetric with respect to the z-axis and all external fields are neglected. Assuming that the lower

plane is rigidly held, the total capillary force is the force required to pull the top plane away from the bottom plane, or the net sum of the capillary pressure force and the surface tension force, as revealed by a force balance on the top plane. Taking the direction of the forces into account (Figure 1.9), equation (1.24) becomes

$$F_C = F_S - F_P. \tag{1.25}$$

From equations (1.2) and (1.3), the capillary pressure force is:

$$F_P = \pi r^2 \gamma_{LG} \left(\frac{1}{R_2} - \frac{1}{R_1}\right) \tag{1.26}$$

where r is the radius of the three-phase contact line on the upper plane, and πr^2 is the wetted area of the plane. R_1 and R_2 have opposite signs because they are acting on opposite sides of the meniscus. Assuming that the meniscus is circular,

$$h = R_2(\cos\phi_1 + \cos\phi_2) \tag{1.27}$$

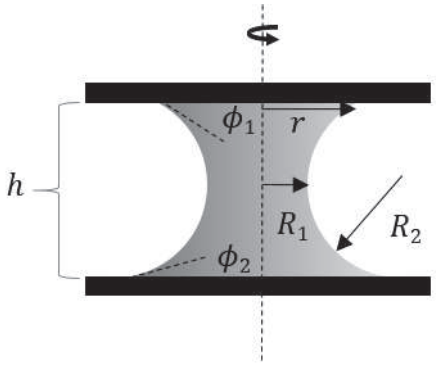

Figure 1.9 Axisymmetric liquid bridge between parallel planes. h is the separation distance; r is the radius of the three-phase contact line on the upper plan; ϕ_1 and ϕ_2 are the contact angles of the liquid bridge against the upper and lower planes, respectively; and R_1 and R_2 are the principle radii of curvature of the meniscus.

with ϕ_1 and ϕ_2 as the contact angles of the liquid bridge against the upper and lower planes, respectively, and that $R_1 \approx r$ for high saturation levels, equation (1.26) becomes

$$F_P = \pi r^2 \gamma_{LG} \left(\frac{(\cos\phi_1 + \cos\phi_2)}{h} - \frac{1}{r} \right). \quad (1.28)$$

The vertical component of the surface tension force can be obtained using equation (1.23):

$$F_S = 2\pi r \gamma_{LG} \sin\phi_1. \quad (1.29)$$

Therefore, the total capillary force acting between the planes separated by a liquid bridge is

$$F_C = 2\pi r \gamma_{LG} \sin\phi_1 - \pi r^2 \gamma_{LG} \left(\frac{(\cos\phi_1 + \cos\phi_2)}{h} - \frac{1}{r} \right). \quad (1.30)$$

Assuming that $R_1 \approx r$ and that the interface was circular significantly reduced the complexity of determining the curvature of the meniscus. The first approximation is not reasonable for low saturations, but the circular approximation is reasonable (within 5%) unless the system is close to saturation [14]. More precise methods to calculate the curvature of the meniscus are known for the plane-plane system but can only be solved numerically [109]–[112].

1.6.1.2 Sphere-Plane

For a smooth sphere against a plane with a toroidal approximation for the curvature of the meniscus, it has been similarly shown that the capillary pressure force is

$$F_P = \pi\gamma_{LG} b^2 \sin^2\phi_f \left(\frac{1}{R_1} - \frac{1}{R_2}\right) \tag{1.31a}$$

$$R_1 = \frac{b(1-\cos\phi_f)+h}{\cos(\phi_1+\phi_f)+\cos\phi_2} \tag{1.31b}$$

$$R_2 = b\sin\phi_f - R_1\left[1-\sin(\phi_1+\phi_f)\right] \tag{1.31c}$$

where b is the radius of the sphere, ϕ_f is the filling angle (Figure 1.10), and h is the separation distance [14], [55], [79], [85], [87]. Again, R_1 and R_2 have opposite signs because they are acting on opposite sides of the meniscus. The surface tension force is

$$F_S = 2\pi b\gamma_{LG}\sin\phi_f\left[\sin(\phi_1+\phi_f)\right]. \tag{1.32}$$

Adding equations (1.31) and (1.32), the total capillary force between a smooth sphere and a plane is

$$F_C = \pi\gamma_{LV} b\sin\phi_f\left[2\sin(\phi_1+\phi_f) + b\sin\phi_f\left(\frac{1}{R_1}-\frac{1}{R_2}\right)\right]. \tag{1.33}$$

Though elegant, equation (1.33) is somewhat cumbersome outside of theoretical studies because the filling angle is not easily determined, especially as it depends on the RH by nature of the Kelvin equation [79]. A simpler expression can be derived by starting with equation (1.26) and assuming that $R_2 \gg R_1$. Then $\left(\frac{1}{R_1}-\frac{1}{R_2}\right) \approx (R_1)^{-1}$ and $F_P \approx \pi R_2^2\gamma_{LG}/R_1$. Additionally, $\pi R_2^2 \approx 2\pi bc$, where c is the height of the meniscus onto

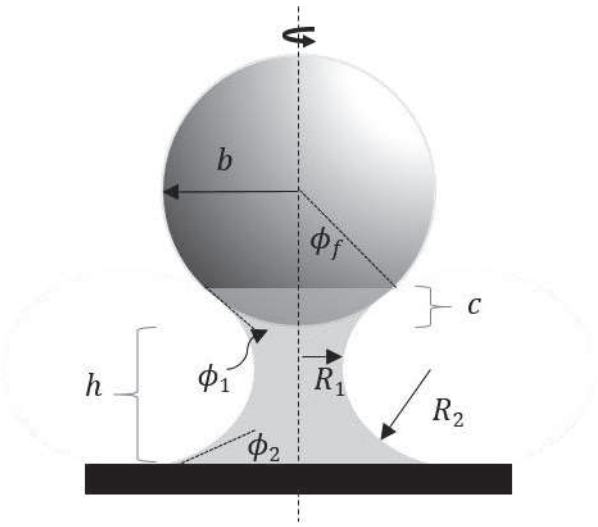

Figure 1.10 Axisymmetric liquid bridge between a smooth sphere and a plane. b is the radius of the sphere; ϕ_f is the filling angle of the meniscus; h is the separation distance; c is the height of the meniscus on the sphere; ϕ_1 and ϕ_2 are the contact angles of the liquid bridge against the sphere and plane, respectively; and R_1 and R_2 are the principle radii of curvature of the meniscus.

the particle (Figure 1.10). When ϕ_f is small and $\phi_1 = \phi_2 = \phi$,

$$h + c \approx 2R_1 \cos\phi. \tag{1.34}$$

Thus, the capillary pressure force is [19], [25]

$$F_p = 4\pi b\gamma_{LG} \cos\phi \left(1 - \frac{h}{2R_1 \cos\phi}\right) = \frac{4\pi b\gamma_{LG} \cos\phi}{1+{}^{h}/_{c}}. \tag{1.35}$$

When $h = 0$ equation (1.35) reduces to

$$F_p = 4\pi b\gamma_{LG} \cos\phi. \tag{1.36}$$

Note that $F_S \approx 2\pi R_2 \gamma_{LG} \sin\phi$, but is generally inconsequential when compared to F_p, unless ϕ is around 90° [25]. Equations (1.35) and (1.36) are the most common forms of the capillary force between a sphere and a plane in the literature [7], [8], [19], [25], [48], [70], [72]–[74], [76], [84], [87], [89]. When utilizing these equations, however, it is important to remember that they are approximations and may not apply at very low or very high RH levels.

1.6.2 Capillary Models Accounting for Non-ideality

As a result of the experimental complexity in obtaining an accurate capillary force as a function of system saturation (see section 1.5), the analytical models used to predict the true contribution of water vapor on adhesion are also widely varied. The effects of surface roughness and ice-like adsorbates on the adhesion will be presented in detail followed by a brief discussion on other treatments of the capillary force.

1.6.2.1 Surface Roughness

The simplest approach to introducing surface roughness into a capillary-force model is to restrict the separation distance between the two adhering surfaces to height h. This represents the height of the asperity limiting the contact between the two surfaces and effectively adds distance to equation (1.31b). This added separation drastically affects the results obtained by equations (1.31), allowing for a zero capillary force at low RH values and causing the capillary force to develop at higher RH for larger separation distances [55]. However, to obtain reasonable results from this method, the average

height asperity must be known and the surface must be fairly uniform in asperity height and distribution. If this is indeed the case, the effect of the average asperity height (R_{rms}) on the capillary force between a sphere and a plate can be represented as [57]

$$F_p = 4\pi b\gamma_{LG}\left(\frac{1-R_{rms}}{2R_1}\right). \quad (1.37)$$

Equation (1.37) has been shown to improve the theoretical prediction of capillary forces between smooth glass spheres and coated Si surfaces.

Most surfaces are not geometrically simple with uniform and nominal roughness. A more sophisticated surface roughness model recognizes that the roughness is actually a distribution of asperity heights. Using this distribution and a distribution of separation distances between rough particles and surfaces, the capillary force can be best estimated [52], [62], [107]. Indeed, the adhesion forces from 13 different experimental studies have been reproduced to within one order of magnitude [85] when modeling surface roughness as a distribution. This indicates that the capillary force may be estimated quantitatively from theory. However, an accurate capillary-force model likely requires the ability to account for the capillary condensation *and* the surface parameters, such as roughness. An excellent review of surface roughness in adhesion models is provided by Prokopovich and Starov [113].

1.6.2.2 Solid-like adsorbed layers on the surface

Traditionally, the forces caused by liquid adsorbates between surfaces is assumed to be caused by the formation of a liquid-vapor interface. However, adsorbed molecules

can form solid-like, monolayer structures on smooth, lyophilic materials (e.g., mica, silicon dioxide, and gold) [114], which changes the interactions in the system from liquid-solid to solid-solid. This phenomenon has been attributed to the surface having an isosteric heat of adsorption greater than the latent heat of condensation for the adsorbate [115]. These solid-solid interactions can increase the overall capillary force by increasing the total surface energy. For example, the number of hydrogen bonds per water molecule is greater in ice than in the liquid, such that a monolayer of ice-like molecules would have a higher surface energy.

An ice-like contribution to the adhesion has been observed by Asay and Kim, who note that the γ_{LG} of water cannot account for the total adhesive force between an AFM probe and an ice-inducing surface. Using attenuated-total-reflectance infrared spectroscopy (ATR-IR) to quantify the thickness of ice-like layers on a strongly hydrophilic surface [106], they develop a solid-adsorbate-solid model that incorporates the estimated surface energy of the ice-like, molecular water with the vdW, Young-Laplace and Kelvin adhesion models. By summing the vdW, capillary and ice-induced forces, they successfully recreate a maximum adhesive force around 0.30 RH, which correlates with their experimental data [66]. Hence, the contribution of the hydrogen bonding within an ice network between the tip and the surface may significantly affect the overall adhesion force for strongly hydrophilic, smooth surfaces [66]. Yet, this result is limited to completely wetting, clean surfaces where ice-like layers are more likely to form.

1.6.2.3 Other Factors

The capillary force is also sensitive to changes in hydrophilicity of the surfaces. Thus, the degree and arrangement of surface heterogeneity is an important factor to consider in capillary force calculations. Butt [107] suggests that surface heterogeneity can be treated as a rough surface where the regions of closer separation represent hydrophilic regions and the larger separation distances represent hydrophobic regions. Essentially, the actual separation distance between the surfaces is adjusted to account for variations in surface hydrophilicity. This treatment exploits the fact that capillary condensation requires a higher RH value to fill larger gaps between surfaces. Overall, it is a promising method but is difficult to experimentally verify because characterizing surface heterogeneity is difficult.

It is also commonly assumed that the meniscus curvature is constant (*i.e.,* circular). However, this assumption is not valid for low RH and RH near saturation. Using numerical methods, the exact form of the Young-Laplace equation has been solved to yield the correct radius of curvature of the meniscus at each point along the interface [48]. Though it can accurately predict experimental forces for AFM tips against smooth surfaces [48], it can be computationally time-consuming and has yet to be extended to describe the interactions between rough surfaces.

Additionally, the capillary force can be considered from the perspective of the work of adhesion required to separate two surfaces from contact [7], [76], [77], [116]. Sedin and Rowlen [7] use this method to predict a vapor-induced force, which they believe is necessary to account for capillary forces in low RH regimes. With the addition

of this vapor-induced force to the traditional prediction of forces caused by liquid-bridges, an experimental maximum in adhesion around 0.3 RH can be explained.

Finally, analytical models of the effects of surface deformation [52], [55], [59], [62], [83], [117], changes in probe/tip shape [14], [48], [55], [63], [79], [85], [87], and vdW force inclusion [55], [66], [69], [73], [79], [82], [83], [87] on the overall adhesion and capillary forces are commonly demonstrated throughout the literature.

In summary, analytical equations describing capillary forces as a function of RH are useful for determining basic trends in ideal situations. However, these models often need to be significantly altered to explain experimental behavior, and often only work in ideal experimental situations. Therefore, while utilizing these models to verify or predict experimental behavior, it is vitally important to note the conditions under which the equations are derived and the inherent or explicit assumptions associated with each model. In this manner, they may be used to appropriately describe capillary forces in particle adhesion.

1.7 Molecular Models

Computer simulations can act as a bridge between capillary-force experiments and analytical equations. With a simulation, specific aspects inherent to every experiment can be isolated or neglected, so, for example, the individual effects of roughness or size and shape may be evaluated without worrying about interference from surface heterogeneity. They also offer insight as to when and how the governing and analytical equations apply. A brief survey of three different types of computer simulations and their application to

capillary forces in particle adhesion is presented starting with a discussion on molecular dynamics. This is followed by the specifics of lattice-gas Monte Carlo techniques. Finally, the utility of mean-field density functional theory is outlined.

1.7.1 Molecular Dynamics Simulations

Molecular dynamics (MD) is a method of simulating the movement of molecules in a system based on continuum or Newtonian equations of motion. Initially, the system is filled with a given number of molecules at specified locations. By allowing the molecules to move and interact, often described by a Leonard-Jones potential, the system evolves over time until a state of equilibrium or quasi-equilibrium has been achieved. At this point, properties of the system can be determined, such as molecular density profiles, temperature, and excess surface energies [118]. Therefore, this type of simulation is particularly suited to investigate the nanoscale properties of capillary forces and interfacial phenomena.

For example, Langroudi *et. al.* [119] have used MD to conclude that the liquid-vapor surface tension is independent of the wettability of the surface and that the Young-Laplace equation is applicable even for nano-size droplets. MD simulations also reveal that the meniscus interface is not a sharp transition from bulk water to water vapor. Indeed, Choi *et. al.* [67] have noted that even with a noticeable density gradient between the liquid-bridge and the bulk vapor, the interfacial thickness ranges from 0.4 to 0.9 nm. Finally, Ko *et. al.* [120] have confirmed that capillary forces are greater between smooth surfaces than that of rough surfaces using MD techniques.

This simulation method is also frequently used to describe capillary effects in AFM measurements [67], [120], [121]. By varying the contact angle of the tip and the surface as well as the separation distance, Cheng and Robbins [121] conclude that the capillary force between AFM tips and surfaces caused by non-volatile liquids is consistent with the Kelvin and Young-Laplace equations for distances greater than 5 nm. At closer separation distances, the MD simulations reveal that the adhesion force becomes oscillatory, which reflects the work required to remove or add complete molecular layers between the surfaces. Such oscillatory behavior is not frequently observed in experiment or reflected in other types of simulations. Other conclusions from this study reveal that the surface tension can be considered to be constant to separation distances close to 1 nm, which is consistent with SFA experiments for hydrocarbons [17]; and that the anisotropy of the pressure tensor causes the pressure difference across the meniscus to be more positive than that predicted by continuum theory [121].

Clearly, MD simulations are robust and offer important insights for experimental studies, since intermolecular attraction, orientation and shape of the molecules may be considered. However, these simulations are computationally arduous and time-consuming. Thus, Monte Carlo techniques and mean-field density functional theory on a lattice-gas offer an attractive alternative to studying interfacial phenomena.

1.7.2 Monte Carlo Lattice Gas Simulations

In the lattice-gas (LG) model, molecules are allowed to occupy sites on a lattice spanning the interstitial space between the two bodies, as shown in Figure 1.11. The

distance between lattice sites usually corresponds to one molecular diameter, and each site is either fully occupied or unoccupied. Molecules are only allowed to interact with their nearest neighbors (NN) with a given intermolecular attraction. When a molecule's NN is either the top or the bottom surface (particle or substrate), binding surface energies are imposed. A molecule is removed from, added to, or moved to a lattice site by calculating the change in the total energy of the system if the change were to occur. If this change is negative (i.e., the change is energetically favorable), the molecular removal, addition or relocation is accepted. If this change is positive, the molecular removal, addition or relocation occurs with a given probability. This grand canonical Monte Carlo (GCMC) process is repeated hundreds of thousands of times, allowing the system to reach equilibrium [65]. Then F_C is calculated by integrating the partial derivative of the excess number of molecules with respect to the bulk system ($N_{ex} = N - N_{bulk}$), with respect to changes in the height (h) for a fixed μ and T [122]

$$F_C = \int_{-\infty}^{\mu} \left(\frac{\partial N_{ex}}{\partial h}\right)_{\mu'} d\mu'. \tag{1.43}$$

These LG GCMC calculations with the thermodynamic integration have been used to predict capillary behavior between an AFM probe and a hydrophilic surface [71], [122]–[128]. By changing the hydrophilicity of the tip relative to the hydrophilicity of the surface, the LG GCMC simulations predict a maximum in the force of adhesion around 30% RH for a strongly hydrophilic tip; a plateau above 34% is predicted for a hydrophobic tip, due to the interaction of two confined layers of water; and a monotonic increase is predicted for a slightly hydrophilic tip [71], [129]. All of these behaviors have

been observed experimentally [6], [7], [55], [66], [115], [130] (see section 1.5). Additionally, the simulations predict the formation, shrinkage, and breakage of liquid bridges between an AFM probe and a substrate [131]. Thus, by only accounting for intermolecular attractions (e.g., hydrogen bonding networks in water) on a simple lattice, it has been shown that capillary forces may affect particle adhesion below 45% RH on strongly or weakly lyophilic surfaces.

This technique is discussed in further detail in Chapter 2, where the results of a LG simulation using the Wang-Landau Monte Carlo technique are presented.

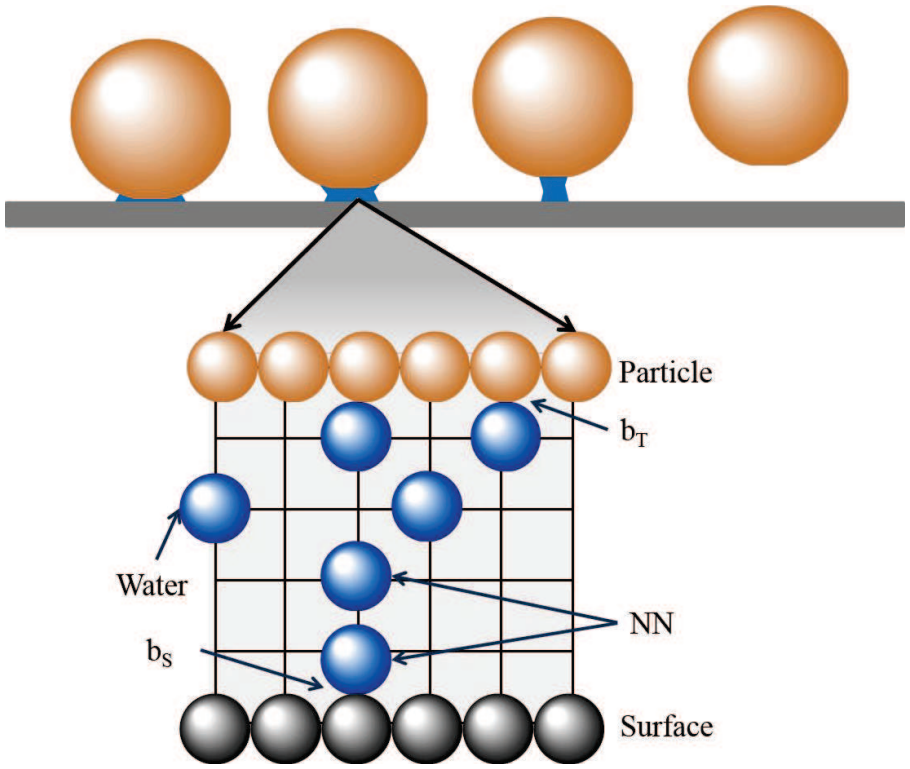

Figure 1.11 Schematic of the lattice-gas simulation model. Water vapor on a lattice interacts with its NNs, the particle and the surface using interaction energies ε, b_T, and b_S, respectively.

1.7.3 Mean-field density functional theory

A similar lattice model based on mean-field density functional theory has also been used to evaluate the liquid-vapor interfacial properties of droplets and liquid bridges. In terms of computational time, lattice density functional theory (LDFT) has the advantage of simply minimizing the energy of the system, rather than requiring the system to equilibrate. Like the LG GCMC model, molecules are allowed to occupy sites on a lattice spanning the interstitial space between the two bodies in LDFT. The lattice spacing remains one molecular diameter, and the value at each site represents the average occupancy or probability a molecule is at that site. Again, molecules can only interact with their NN's.

With the same setup as the LG GCMC model, the LDFT model also predicts a maximum in the adhesive force around 30% RH for a strongly hydrophilic tip; a plateau above 34% RH for a hydrophobic tip; and a monotonic increase for a slightly hydrophilic tip [71]. Moreover, LDFT can predict capillary condensation in mesopores of disordered materials by accurately reproducing experimental hysteresis and equilibrium behavior of condensed vapors [132]–[134]. Furthermore, a relationship between contact angles and surface binding energies can be estimated [134].

Finally, LDFT can be used to examine the meta-stable, stable, and transitional points in the overall energy of the system as a function of surface binding energies and separation distance. Since transitional states or saddle points are unstable thermodynamically and computationally, the LDFT method can be constrained simply to stabilize these transitional states. Some of the major findings are 1) that the formation of

a liquid bridge at high RH has a lower activation energy than the activation energy required to break the liquid bridge. Hence, patterns of hysteresis are observed. 2) The spontaneous formation or rupture of a liquid bridge depends on the distance between the surface and the tip and their hydrophilicity [135] as well as tip pull-off velocity [108]. These results, with the exception of the dependence of the capillary force on RH, are for RH environments of 50-95% [108], [135].

The LDFT approach to modeling capillary condensation is not as robust as the MD or LG GCMC simulations. Hence, there are some results, such as density profiles across an interface resembling a tanh curve, that are mean-field artifacts [136]. However, its simplicity requires less computational resources and time allowing for larger and a wider variety of systems to be analyzed. Hence, it is the method used in Chapter 3 to investigate the curvature of liquid-vapor interfaces of liquid bridges between two plates as a function of contact angle, RH, and separation distance.

1.8 Conclusion

Capillarity is an important phenomenon with applications spanning from biology to tribology. The particular focus of this review has been on forces caused by capillarity in solid systems, known as capillary forces, and their dependence on the system saturation.

As a result, the origin of the governing equations of capillarity, particularly the Young-Laplace, Young, and Kelvin equations have been discussed. The assumptions explicit or inherent to each of them has been evaluated and must be considered carefully before they can be properly employed. Specifically, it is important to remember that the

Kelvin equation is only applicable for a pure-component, two-phase system in thermal and mechanical equilibrium. Hence, utilizing it to describe capillary condensation between solid surfaces can lead to inaccurate results as will be shown in Chapter 3.

Additionally, a variety of aspects surrounding the experimental determination and validation of capillary forces primarily via AFM have been analyzed (Tables 1.1-1.8). It is demonstrated that the hydrophilicity of the adhering surfaces merely allows for the presence of a capillary force, but does not dictate its dependence on RH. Though commonly studied, there is little agreement throughout the literature as to how the capillary force depends on system saturation due to a multitude of experimental factors such as tip size, shape, and deformation, not to mention ionic diffusion into liquid bridges, local roughness, and surface heterogeneity.

Some of the experimental trends have been described by basic analytical equations. However, these models often need to be altered to explain experimental behavior, and may only work in ideal experimental situations. Therefore, while utilizing these models to verify or predict experimental behavior, it is vitally important to note the conditions under which the equations are derived and the inherent or explicit assumptions associated with each model.

Molecular simulations, such as the lattice-gas Monte Carlo technique, circumvent the experimental challenges and do not require geometrical arguments to determine capillary forces. In this manner, aspects such as surface heterogeneity and roughness can be removed in order to investigate basic properties of capillary forces between solid surfaces.

To avoid describing experimental artifact, new AFM capillary force experiments have not been performed in this work, nor has a new analytical model for a specific case been developed. Instead, the LG Monte Carlo and LDFT simulations have been used to study the principles of capillarity in solid systems as the RH level changes in Chapters 2 and 3.

CHAPTER 2. MONTE CARLO SIMULATIONS OF CAPILLARY FORCES

2.1 Introduction

The presence of liquid bridges caused by condensed vapors (water vapor is the most common and the object of this study) can either be a benefit or a hindrance in atomic force microscopy (AFM). For example, the liquid bridge between an AFM cantilever tip and a substrate is the medium through which molecules diffuse onto the substrate in dip-pen nanolithography [122], [131]. Yet, these same liquid bridges can significantly increase the adhesion in AFM force and imaging experiments and thereby complicate the analysis of these studies [54], [55]. Therefore, the ability to correctly predict the presence and influence of capillary forces in varying environments for AFM applications is necessary.

As has been noted experimentally, the capillary forces between a hydrophilic surface and hydrophilic tip can decrease monotonically [63], increase step-wise or monotonically [7], [68], [70], [89], or exhibit a maximum [6], [55], [69], [87] in the adhesion force with increasing relative humidity (RH). Unexpectedly, much of the maxima behavior is observed in low RH environments (<0.5 or 50% RH), where capillary forces are often considered negligible [57], or theoretically unlikely [47], and where the Kelvin equation, which is typically used to describe the onset of capillary

condensation/forces, has not yet been verified for water [17], [20], [53]. Although adsorbed, ice-like monolayers of water are present in these low RH environments [6], [66], [106], [114] and can be expected to influence the overall adhesion between an AFM tip and a substrate, attributing all of the capillary force behavior in low RH to interactions between adsorbed water layers is likely overly simplistic.

In recent years, grand canonical Monte Carlo simulations [65], [71], [122]–[126], [128], [131], [137]–[140], molecular dynamics simulations [67], lattice density functional theory calculations [71], [135], [141], and semi-empirical methods [66], [106], have been used to study the behavior of adsorbed and condensed water vapor in AFM at low RH. The formation and breakage of liquid bridges have been observed [131] along with critical liquid bridge radii and stability requirements [123]. Trends in AFM force experiments have also been qualitatively reproduced [65], [71], though nanoscale roughness on the tip and/or the surface does significantly affect these trends [57], [128], [142]. All of these results suggest that it is possible for liquid-like bridges to form and affect AFM measurements in low RH environments.

In this work, the lattice-gas model developed and extensively studied by Jang *et. al.,* [65] has been utilized to analyze the thermodynamic properties, including the capillary forces and first order transitions, of adsorbed/condensed vapors between an AFM tip and a hydrophilic surface as a function of RH. The Wang-Landau Monte Carlo (WLMC) sampling technique is used to determine these properties in place of the traditional grand canonical Monte Carlo technique because the WLMC technique estimates the partition function of the system. Hence, it is possible to calculate the capillary force, F_C, internal energy (E), entropy (S), and Gibb's energy (G) at several

different temperatures and RH values in one simulation. The WLMC technique and its resulting thermodynamic study has not yet been undertaken to explore capillary behavior in AFM as a function of RH.

In this study, the basic theory needed for the WLMC simulations is first outlined, followed by a brief description of the parameters involved in the simulations. Computational results are then presented and compared with previously published studies.

2.2 Model

As presented in [131], the lattice gas (LG) model for capillary forces allows water molecules to occupy sites on a two-dimensional lattice spanning the interstitial space between the two bodies. The lattice spacing, σ, is one molecular diameter (0.324 nm) and each site is either fully occupied or unoccupied. Only interactions between a molecule and its nearest neighbors (NN) are allowed. Water molecules interact with other NN water molecules with an intermolecular attraction energy of ε, whereas water molecules interact with solid surface NN with binding energies of b_T (solid surface of AFM cantilever tip) or b_s(solid surface below AFM cantilever tip). Finally, each molecule has its own chemical potential, μ, which is related to the RH of the system by

$$\mu = k_B T \ln RH + \mu_c \tag{2.1}$$

where k_B is Boltzmann's constant, T is the system temperature, and μ_c is the

chemical potential at the bulk gas-liquid transition. For a two-dimensional LG system, $\mu_c = -2\varepsilon$ [143].

The internal energy E of the system is then given by

$$E = -\frac{\varepsilon}{2}\sum_{i,j=NN} c_i c_j - b_T \sum_{\substack{i=tip \\ adj.}} c_i - b_s \sum_{\substack{i=surf. \\ adj.}} c_i \tag{2.2}$$

where c_i and c_j indicate the occupation of site i or j and is divided by two to avoid double counting of the NN interaction. The first summation is over all NN not adjacent to the tip or the surface; the second is over all tip-adjacent NN; and the third is over all surface-adjacent NN. The free energy of the system $\mathcal{F}$ is then given by

$$\mathcal{F} = E - \mu N, \tag{2.3}$$

where N is the total number of molecules in the system or the total number of occupied sites [65].

2.3 Theory

It is convenient to work in the grand canonical ensemble where the temperature, T, and the chemical potential, μ, of the system are held constant. The free energy of the system in terms of the grand potential, Ω, can be expressed as

$$\Omega = -pV = E - TS - \mu N, \tag{2.4}$$

where p is the pressure, V is the volume, E is the internal energy, and S is the entropy.

For a fluid confined between two parallel plates [45]

$$\mathrm{d}E = -p\,\mathrm{d}V + T\mathrm{d}S\ + \mu\mathrm{d}N + 2\gamma_{\mathrm{SF}}\mathrm{d}A_s - (F_C)\mathrm{d}h, \tag{2.5}$$

where γ_{SF} is the solid surface-fluid interfacial tension, A_s is the surface area of the plate, F_C is the pressure-driven capillary force, and h is the distance between the two surfaces. Equation (2.4) then becomes

$$\mathrm{d}\Omega = -p\,\mathrm{d}V - S\mathrm{d}T - N\mathrm{d}\mu + 2\gamma_{SF}\mathrm{d}A_s - (F_C)\mathrm{d}h. \tag{2.6}$$

For a bulk system with the same p, V, T, and μ as the confined fluid [45],

$$\mathrm{d}\Omega^{\mathrm{b}} = -p\,\mathrm{d}V - S^b\mathrm{d}T - N^b\mathrm{d}\mu, \tag{2.7}$$

where the superscript b indicates a bulk quantity. Subtracting equation (2.7) from equation (2.6) yields

$$\mathrm{d}\Omega - \mathrm{d}\Omega^b = -S\mathrm{d}T + S^b\mathrm{d}T - N\mathrm{d}\mu + N^b\mathrm{d}\mu + 2\gamma_{SF}\mathrm{d}A_s - (F_C)\mathrm{d}h. \tag{2.8}$$

At constant A_s, T, and μ, equation (2.8) then reduces to

$$F_C = \left(\frac{\partial\Omega^{\mathrm{b}}}{\partial h}\right)_{T,\mu,A_s} - \left(\frac{\partial\Omega}{\partial h}\right)_{T,\mu,A_s}. \tag{2.9}$$

where a negative force is defined as an attractive capillary force between the two plates. Furthermore, Ω and Ω^{b} are related to the partition function Z through

$$\Omega = -k_B T \ln Z \tag{2.10}$$

with

$$Z = \sum_E \sum_N g(E,N) e^{\left(\frac{\mu N}{k_B T}\right)} e^{-\frac{E}{k_B T}}. \tag{2.11}$$

where $g(E,N)$ is the density of states (i.e., the number of configurations) for a given E and N [144].

Since the functional form of Z as a function of h is not explicitly known, $\left(\frac{\partial\Omega}{\partial h}\right)_{T,\mu,A_s}$ is approximated by calculating the difference in Ω with a small change in separation distance (i.e., one lattice spacing, σ):

$$\left(\frac{\partial\Omega}{\partial h}\right)_{T,\mu,A_s} \approx \frac{\Delta\Omega}{\Delta h} = \frac{\Omega_{h+\sigma}-\Omega_h}{\sigma} = -\frac{1}{\sigma}\left(k_B T \ln\frac{Z_{h+\sigma}}{Z_h}\right) \tag{2.12a}$$

$$\left(\frac{\partial\Omega^{\mathrm{b}}}{\partial h}\right)_{T,\mu,A_s} \approx \frac{\Delta\Omega^{\mathrm{b}}}{\Delta h} = \frac{\Omega^{\mathrm{b}}_{h+\sigma}-\Omega^{\mathrm{b}}_{\mathrm{h}}}{\sigma} = -\frac{1}{\sigma}\left(k_B T \ln\frac{Z^b_{h+\sigma}}{Z^b_h}\right). \tag{2.12b}$$

From equations (2.9) and (2.12), F_C is then

$$F_C = \frac{1}{\sigma}\left(k_B T \ln\frac{Z_{h+\sigma}Z^b_h}{Z^b_{h+\sigma}Z_h}\right) \tag{2.13}$$

In addition to calculating F_C, ensemble averages, such as the average number of molecules in the system $\langle N\rangle$, are also calculated with Z:

$$\langle \mathrm{B}\rangle = \frac{\sum_{E,N} g(E,N)\ \mathrm{B}\ e^{\left(\frac{-H}{k_b T}\right)}}{Z}, \tag{2.14}$$

where B represents a thermodynamic property of interest (*e.g.*, N or E). It then follows that the approximate derivatives of the ensemble averaged quantity with respect to h can be determined by

$$\left(\frac{\partial \mathrm{B}}{\partial h}\right)_{T,\mu,A_s} \approx \frac{\Delta\langle \mathrm{B}\rangle}{\Delta h} = \frac{(\langle \mathrm{B}\rangle_{h+\sigma} - \langle \mathrm{B}\rangle_h)}{\sigma} \tag{2.15}$$

Equation (2.15) is utilized in analyzing the effects of different energetic components on the behavior of the capillary force curve as a function of RH.

2.4 Methods

2.4.1 Wang-Landau Monte Carlo Method

Traditional Monte Carlo techniques add, subtract, or remove molecules from the system based on a given probability. A drawback to this approach is that as the size of the system increases, the number of possible configurations exponentially increases. In contrast, the number of energies of a given system scales proportionally with the size of the system [144]. Thus for larger simulations, a more efficient technique is to sample over all of the available energies.

Exploiting this advantage, the Wang-Landau Monte Carlo (WLMC) method [144]–[146] finds Z by sampling the energies of a system and recording the frequency that a given free energy state is visited. The more often free energy $\mathcal{F}(E_0, N_0)$ is visited in comparison to other free energies, the more configurations that correspond to $\mathcal{F}(E_0, N_0)$ and the higher its probability density.

An excellent presentation of the WLMC method is given in [144]. In summary, to perform WLMC sampling, $g(E, N)$ for all E and N and the modification factor f are initialized to $g(E, N) = 1$ and $f = \exp(1)$ or, more conveniently, $\ln\big(g(E, N)\big) = 0$ and $\ln f = 1$. The system is then given a random configuration and $\mathcal{F}(E_0, N_0)$ is determined from equations (2.2) and (2.3). A molecule is then added,

subtracted, or relocated and $\mathcal{F}(E_1, N_1)$ for the new configuration is calculated. The move is accepted based on the following probability, P,

$$P(\mathcal{F}(E_0, N_0) \rightarrow \mathcal{F}(E_1, N_1)) = \min\left(\frac{g(E_0,N_0)}{g(E_1,N_1)}, 1\right). \quad (2.16)$$

Every time a given $\mathcal{F}(E_i, N_i)$ is accessed, its corresponding $g(E_i, N_i)$ and histogram $D(E_i, N_i)$ are updated to $g(E_i, N_i) = fg(E_i, N_i)$ and $D(E_i, N_i) = D(E_i, N_i) + 1$. This algorithm punishes the acceptance of moves toward highly probable energies and permits the uniform sampling of all energies of the system [145]. After an initial number of Monte Carlo moves, the uniformity of $D(E, N)$ is analyzed. If $D(E, N)$ is non-uniform, the addition, subtraction and relocation of molecules continues until the distribution becomes uniform. When this occurs, $D(E, N)$ is reset to zero, the modification factor is reduced, $f_{i+1} = \sqrt{f_i}$, and the Monte Carlo process repeats until $f_{i+1} < f_{min}$. For small, well-behaved systems $f_{min} = \exp(10^{-8})$, typically. The resulting $g(E, N)$ is a relative quantity until it is normalized to the total number of configurations possible for the system. Once the absolute $g(E, N)$ is known, Z may be determined with equation (2.11).

2.4.2 Simulation Parameters

For the present simulations, a 23 nm radius of curvature (ROC) AFM tip is simulated on a square 45x45 lattice with reflective boundary conditions at 300 K. σ is set to the molecular diameter of water, 0.324 nm [122]. The interaction energy between molecules, ε, is 9500 J/mol, from $\varepsilon = 2k_bT_c \ln\left(1 + \sqrt{2}\right)$ and $T_c = 647.3$ K

[147]. Effects of hydrophilicity on capillary forces are investigated by varying the cantilever tip interaction energies from completely wetting (CW) $b_t = 3\varepsilon$, to partially wetting (PW) $b_t = 0.75\varepsilon$, and finally to partially drying (PD) $b_t = 0.25\varepsilon$, whereas the opposing surface is held as a CW surface, $b_S = 3\varepsilon$. Only half of the tip is simulated since the system is symmetric about the center [122] and then the magnitude of the resulting force is multiplied by 2.

For the WLMC method, an initial sweep of 10^5 Monte Carlo moves is performed to determine the number of accessible energies for a given N; f_{min} is set to 10^{-4}, which is the lowest resolution required for Z to converge; and $D(E,N)$ is considered uniform if the minimum of $g(E,N)$ is greater than or equal to 80% of the average of $g(E,N)$.

2.4.3 Verification of the WLMC Model

The validity of the WLMC model has been tested using the simplest case of an ideal gas. Without interactions with the walls (b_T and $b_S = 0$) or between molecules ($\varepsilon = 0$), equation (2.3) reduces to

$$\mu N = k_B T N \ln RH. \tag{2.17}$$

Equation (2.17) can also be expressed in terms of the average site density ρ by dividing by the total number of sites, N_{tot}:

$$\mathcal{F}/N_{tot} = -k_B T \rho \ln RH. \tag{2.18}$$

Using lattice density functional theory [65] (LDFT) it can be shown for an ideal gas that

$$\rho = \frac{RH}{1+RH} \tag{2.19a}$$

and

$$\frac{S}{N_{tot}} = -k_B[\rho \ln \rho + (1-\rho)\ln(1-\rho)]. \tag{2.19b}$$

Therefore, it is expected that as RH $\longrightarrow$ 0, $\mathcal{F}$, ρ, and S/N_{tot} all tend toward 0. As RH $\longrightarrow$ 1, $\mathcal{F} \longrightarrow 0$, $\rho \longrightarrow$ ½, and $S/N_{tot} \longrightarrow -k_B \ln 1/2$. As shown in Figure 2.1, the predicted ideal gas behavior for the lattice system has been reproduced using the WLMC model, even with a curved geometry caused by shape of the tip. In Figure 2.1a, $\mathcal{F}$ tends toward 0 as RH approaches either 0 or 1 and exhibits a global minimum at RH ≈ 0.278, which is the theoretical predicted minimum of $\mathcal{F}$ with respect to RH. Figure 2.1b shows that the average number of molecules in the system increases to ½ as the system approaches saturation and Figure 2.1c demonstrates the predicted entropic increase for both the WLMC and LDFT methods.

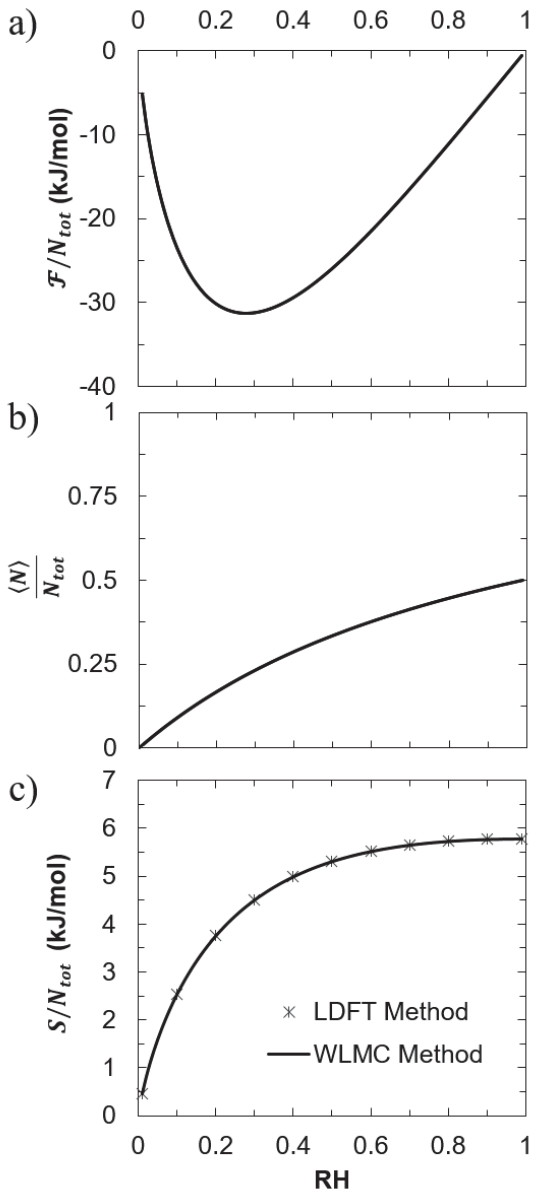

Figure 2.1 WLMC results for an ideal gas (b_T, b_S, and $\epsilon = 0$) at 300 K. a) Total free energy as a function of RH with a minimum at RH = 0.278. b) Average number of particles divided by the total number of sites as a function of RH. c) Entropy as a function of RH as predicted by the LDFT (crosses) and WLMC method (solid line).

2.5 Results and Discussion

The interaction forces between a cantilever tip and a substrate (force-distance curves) for a CW tip and CW surface at varying RH levels from a 10x10 matrix with periodic boundary conditions are shown in Figure 2.2. The forces have been non-dimensionalized and are reported in units of ε/σ, which is approximately 49 pN. A negative force indicates an attractive interaction, whereas a positive force indicates a repulsive interaction. The purpose of using a small simulation size is to quickly verify the general shape of force vs. distance curves and to identify the point at which the highest attractive force occurs.

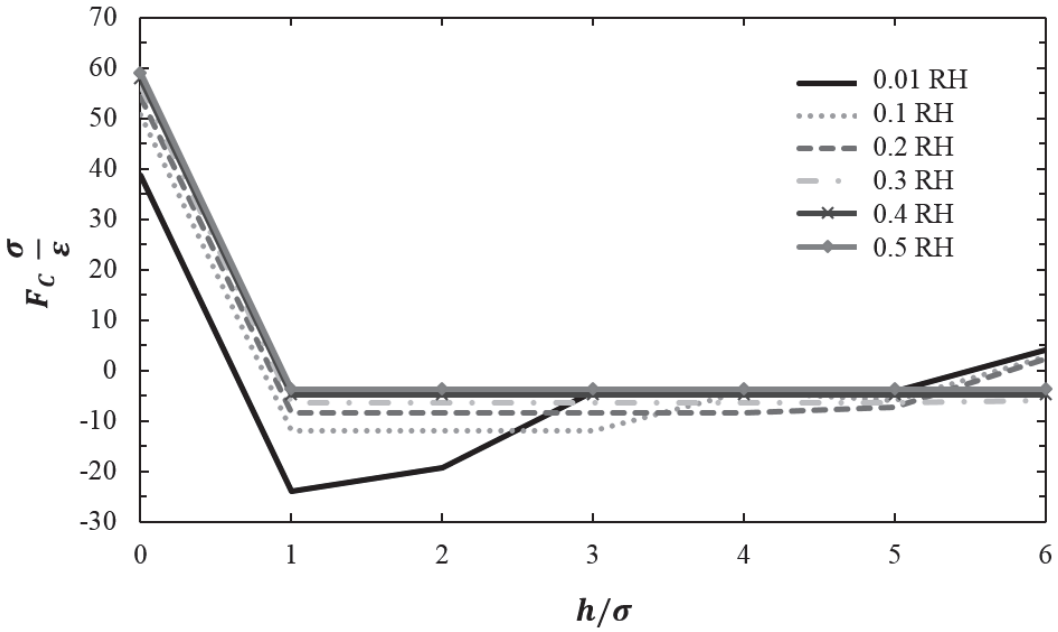

Figure 2.2 Capillary force-distance curves at varying RH levels for a CW tip and CW surface at 300 K. The size of the lattice is 10x10. Force is given in units of ε/σ and the separation distance is in lattice units, σ.

When the tip and the substrate are in contact (i.e., $h/\sigma = 0$), F_C is repulsive. This means that the free energy required to hold the two surfaces together is much greater than the free energy required to form a monolayer of water between the two surfaces. Such a result is expected for two highly hydrophilic surfaces that don't interact with one another. At large tip-surface separation distances, F_C approaches 0, indicating the rupture of confined fluid bridges. The strongest attractive force occurs when $h/\sigma = 1$ for all RH levels, indicating this is the most energetically favored separation distance for F_C. As such, the separation distance between the tip and substrate has been fixed at $h/\sigma = 1$ for all other calculations of F_C in this study. The fact that the adhesion decreases monotonically with increasing RH is a consequence of simulation size, boundary effects, and the strong hydrophilic nature of the tip and surface.

Figure 2.3 shows F_C as a function of RH for CW, PW, and PD tips (dark, medium, and light gray lines, respectively) from the WLMC simulations (using reflective boundary conditions) on a 45x45 lattice. Even with size and boundary effects mitigated on this larger lattice, F_C remains strongly dependent on RH and the hydrophilicity of the tip and the surface, resembling experimental results via AFM [7], [69]. For example, a CW tip exhibits a maximum in adhesion between .05 and 0.3 RH and then decreases toward zero as RH approaches one. Figure 2.3 also agrees with that of Jang, Schatz, and Ratner [122] who obtained similar trends and magnitudes in their study of the same system using grand canonical Monte Carlo sampling. That the two do not align perfectly is to be expected because the methods of sampling the system are different. Jang and Schatz sample the number of

configurations, whereas this study samples the number of free energy states. Thus the two methods should produce identical results but might not because one method may be more efficient in sampling the free energy space than the other. It is more important to note that the trends and magnitudes of the force-RH curves are similar leading to the same conclusion. Other common factors between the two studies are that the magnitude of F_C typically increases with increasing tip hydrophilicity; that F_C for PD and PW tips is weakly dependent on RH, as expected due to the tips' more hydrophobic nature; and that F_C for the PD, PW, and CW tips approach a similar value as the RH approaches one. All of this leads to the conclusion that it is theoretically possible to observe a maximum in capillary forces below 0.45 RH for hydrophilic surfaces.

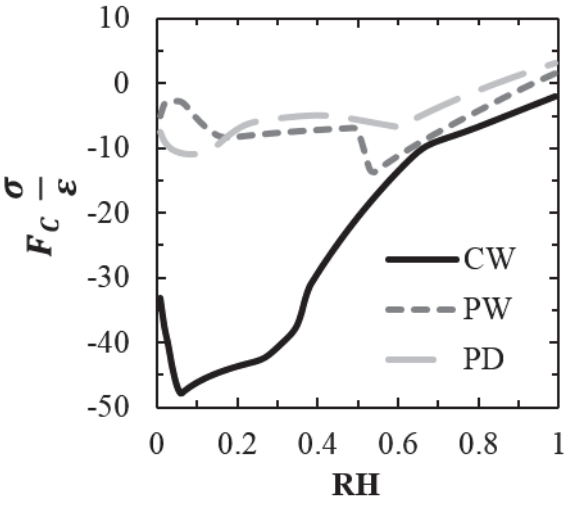

Figure 2.3 Capillary force as a function of RH for CW, PW and PD AFM tips (23 nm ROC). Force is given in units of ε/σ on a 45x45 lattice. All calculations are performed at 300 K.

The trends in F_C can be explained by evaluating the thermodynamic properties of the equilibrated systems. Only the results of the PW tip are shown in Figure 2.4 as a representation of the trends observed in all three tip types. As calculated using equations (2.14) and (2.15), the individual energetic ($\Delta\langle E\rangle/\Delta h$, dark gray), Gibbs energetic ($\Delta\langle G\rangle/\Delta h$, solid light gray), and entropic ($\Delta\langle ST\rangle/\Delta h$, broken light gray) contributions to $\Delta\Omega/\Delta h$ are shown in Figure 2.4a. Expectedly, $\Delta\langle E\rangle/\Delta h$ and $\Delta\langle G\rangle/\Delta h$ are similar in shape and magnitude and it is the difference between these two quantities that dominates $\Delta\Omega/\Delta$h (and by corollary, F_C). However, as the RH approaches the extremes, the difference between the energetic and Gibbs energetic contributions is on the same order of magnitude as $\Delta\langle ST\rangle/\Delta h$ and $\Delta\Omega/\Delta$h is instead dominated by a combination of the three components. This suggests that entropy becomes an important aspect to capillary forces at low RH and near saturation.

Figure 2.4b shows the average number of molecules in the system at h ($\langle N\rangle_h$, solid dark gray line) and $h+\sigma$ ($\langle N\rangle_{h+\sigma}$, solid light gray line) as a function of RH. The change in the average number of molecules in the system divided by the change in height ($\Delta\langle N\rangle/\Delta h$) is plotted on the secondary axis (light gray broken line). At 0.01 RH, $\langle N\rangle_h$ and $\langle N\rangle_{h+\sigma}$ are between 30 and 40, suggesting that a monolayer of water is forming on the CW substrate. When both systems have reached 0.2 RH, a complete monolayer of water has formed on the CW surface and dominates the interaction up to about 0.5 RH. Such a persistence of adsorbed layers of water vapor on hydrophilic surfaces has been observed experimentally [98] and does influence the strength of the capillary force in the low RH environment. Around 0.5 RH, $\langle N\rangle_h$ sharply increases followed shortly thereafter by $\langle N\rangle_{h+\sigma}$, suggesting the formation of a liquid bridge that

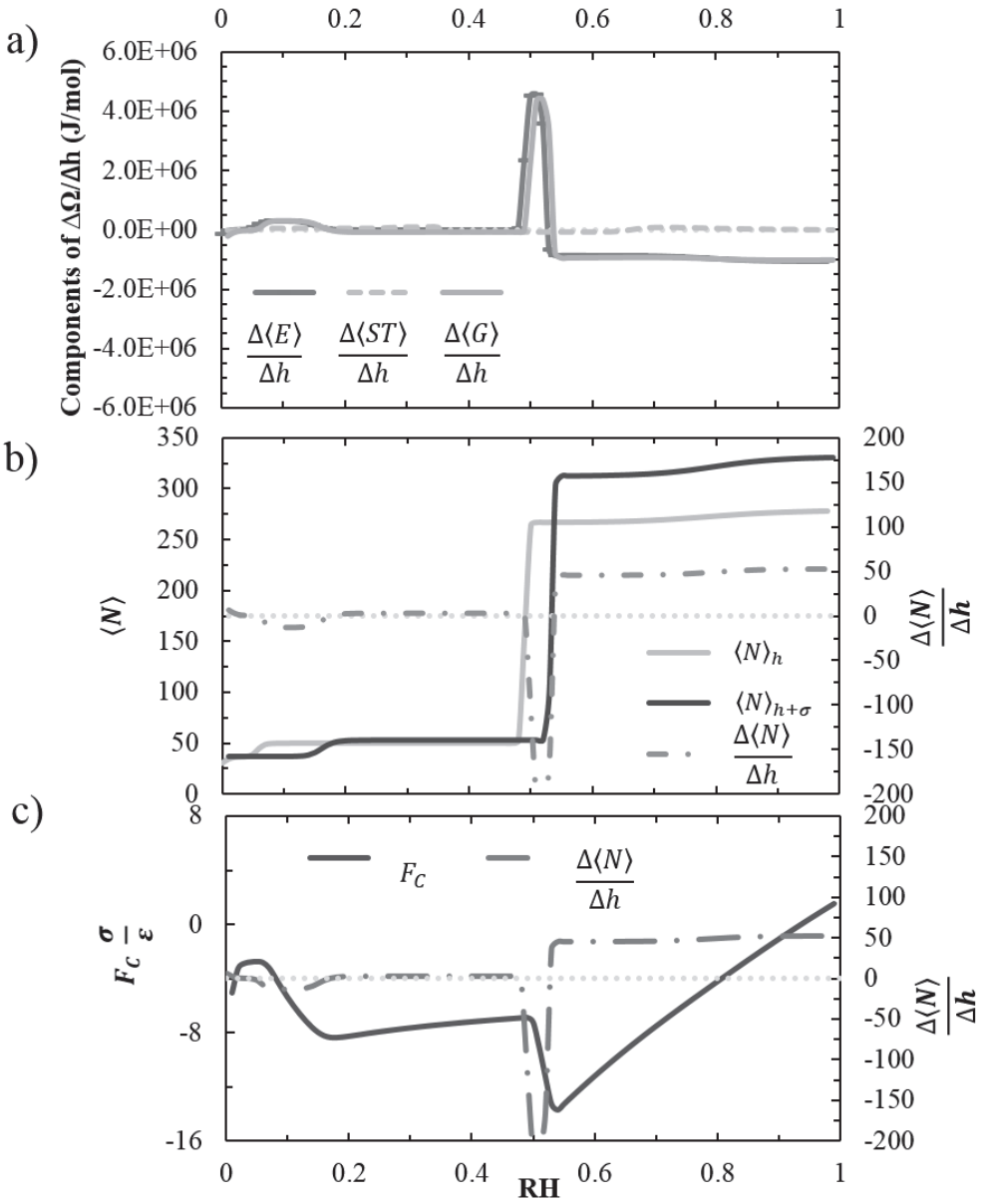

Figure 2.4 Capillary force dependence on $\Delta\langle E\rangle/\Delta h$, $\Delta\langle G\rangle/\Delta h$, $\Delta\langle ST\rangle/\Delta h$ and $\Delta\langle N\rangle/\Delta h$ on a 45x45 lattice for a PW tip at 300 K. a) Contributions of $\Delta\langle E\rangle/\Delta h$, $\Delta\langle G\rangle/\Delta h$, and $\Delta\langle ST\rangle/\Delta h$ to $\Delta\Omega/\Delta$h. b) Average number of particles in the system at tip-substrate distances h and $h+\sigma$ ($\langle N\rangle_h$ and $\langle N\rangle_{h+\sigma}$, respsectively) (primary axis). $\Delta\langle N\rangle/\Delta h$ is indicated on the secondary axis. c) The capillary force is shown on the right-hand axis in units of ε/σ. $\Delta\langle N\rangle/\Delta h$ refers to the left-hand axis. In all figures, the dotted gray line indicates the zero line.

then gradually fills the system as it approaches saturation. The appearance of capillary forces above a threshold RH is commonly observed experimentally [8], [48], [74].

Interestingly, there are regions where $\langle N \rangle_h > \langle N \rangle_{h+\sigma}$ causing $\Delta\langle N \rangle / \Delta h$ to be negative. Physically this situation indicates that the system at h can hold more molecules because of its proximity to the two surfaces than the system at $h + \sigma$ can at that RH. In Figure 2.4c, the plot of F_C vs. RH on the primary axis and $\Delta\langle N \rangle / \Delta h$ on the secondary axis is reproduced for comparison. This representation clearly indicates that F_C increases when $\Delta\langle N \rangle / \Delta h$ is negative and decreases when $\Delta\langle N \rangle / \Delta h$ is positive. In other words, F_C increases if the average number of molecules in the confined liquid bridge increases as the two surfaces approach one another. Or, conversely, F_C decreases if the average number of molecules in the confined liquid bridge decreases as the two surfaces approach one another. Therefore, the decrease in F_C as RH increases that is observed for the tips suggests that $\langle N \rangle_{h+\sigma} > \langle N \rangle_h$ at high RH.

Figures 2.3 and 2.4 suggest that capillary forces can be present and dominant in low RH environments. These forces, whether caused by interactions within solid or liquid water, can affect the results of AFM studies through either the transfer of ions onto the sample surfaces or increased adhesion. Therefore, it is important to consider the possibility of capillary forces in any AFM study where hydrophilic surfaces are used.

2.6 Conclusion

The LG GCMC model has been used with WLMC sampling to predict F_C as a function of h, RH, and tip hydrophilicity on a 45x45 lattice. It is found that the maximum force occurs when $h = \sigma$ and that F_C decreases as h increases, except when the tip and the surface are in contact. CW tips exhibit a maximum in F_C as RH increases, while PW and PD tips are relatively independent of RH. These force-RH trends are generally dominated by the difference between the internal energy and the Gibbs energy of the system and $\Delta\langle N\rangle/\Delta h$. It is also observed that capillary forces can be significant in low RH environments and thus cannot be ignored in AFM studies involving hydrophilic surfaces.

CHAPTER 3. ANALYSIS OF THE KELVIN EQUATION

3.1 Introduction

Though the WLMC simulations are useful for determining the thermodynamic properties of a confined fluid, the time requirements of these simulations limit the dimensionality, size, and number of parameters that can be evaluated with this technique, even when the code is fully parallelized. Therefore, it is proposed that a similar lattice model based on mean-field density functional theory be used to evaluate the nanoscopic properties of condensed vapor in particle adhesion. In terms of computational time, lattice density functional theory (LDFT) has the advantage of only minimizing the free energy of the system, rather than finding the density of states of all free energies. Because it is computationally simpler, LDFT can be used to investigate how the surface tension of a meniscus depends on the curvature of the meniscus and ultimately how these curvature effects influence the presence and strength of capillary forces in particle adhesion.

In this chapter, LDFT has been utilized to describe bulk and two- behavior of a pure component system for planar interfaces, bubbles in a metastable liquid, and liquid bridges between parallel plates. The concepts of dividing surfaces, particularly the surface of tension, are introduced, and are used to determine the dependence of the curvatures of an interface as a function of system saturation.

These results are compared with the traditional Kelvin equation for curved interfaces with and without plates at varying RH levels, separation distances, and contact angles. Accounting for the deviation from the Kelvin equation can yield more physical results and allows for the appropriate calculation of pressure differences across the liquid-bridge interface and corresponding capillary forces.

3.2 Lattice Density Functional Theory

LDFT conveniently operates within the framework of the lattice-gas (LG) model which can be described as a molecularly-occupied, skeletal lattice in free space or in the interstitial space between two surfaces. Each intersection represents a site where a molecule can exist and is separated from other lattice sites by the effective diameter of one molecule. Each site is assigned a value between zero and one indicating the average occupancy (or density) of a molecule at that site. Finally, only interactions between nearest neighbors (NN) are allowed. A benefit of using the LG model in LDFT is that the critical chemical potential at the bulk gas-liquid transition is known [65]. This is necessary to relate the RH to the chemical potential.

Using the mean-field approximation [71], [148], the energy E of a pure component, unconfined system with only intermolecular interactions on a lattice is

$$E = -\frac{\mathcal{Z}}{2}\varepsilon N_a \frac{N_a}{N_{tot}}. \tag{3.1}$$

$\mathcal{Z}$ is the total number of possible bonds per site (4 for a 2-D system and 6 for a 3-D system), ε is the intermolecular attraction energy, N_a is the number of occupied sites, and N_{tot} is the total number of sites in the system. With the average occupancy at

each site defined as $\rho = N_a/N_{tot}$, equation (3.1) becomes

$$E = -\frac{\mathcal{Z}}{2} N_{tot} \varepsilon \rho^2. \tag{3.2}$$

By assuming random mixing and neglecting energies of interaction, the entropy S of the system is

$$S = -N_{tot} k_b [\rho \ln \rho + (1-\rho) \ln(1-\rho)]. \tag{3.3}$$

where k_b is Boltzmann's constant. As a result, the Helmholtz energy $\mathcal{F}$ of the system in terms of ρ is

$$\mathcal{F} = E - TS = -\frac{\mathcal{Z}}{2} N_{tot} \varepsilon \rho^2 + N_{tot} k_B T [\rho \ln \rho + (1-\rho) \ln(1-\rho)] \tag{3.4}$$

with T as the absolute temperature of the system.

The system pressure p is the change in the Helmholtz energy with respect to the change in volume of the system while the temperature and number of occupied sites are held constant or

$$p = -\left(\frac{\partial \mathcal{F}}{\partial V}\right)_{T,N_a}. \tag{3.5}$$

From equation (3.4) and by noting that $V = N_{tot} V_o$ (V_o is the volume per lattice site), the pressure-volume element pV_o at each site becomes

$$pV_o = -\left(\frac{\partial \mathcal{F}}{\partial N_{tot}}\right)_{T,N_a} = -\frac{\mathcal{Z}}{2} \varepsilon \rho^2 - k_b T \ln(1-\rho). \tag{3.6}$$

Similarly, the chemical potential of the system μ becomes

$$\mu = \frac{\mathcal{F}+pV_oN_{tot}}{N_a} = -\mathcal{Z}\varepsilon\rho + k_bT\ln\frac{\rho}{1-\rho}. \quad (3.7)$$

In order to ensure that the LDFT model properly represents a physical system, the behavior at the critical point must be established. The critical point marks the end of the phase coexistence curve for a given pure-component system [144], [149]. For conditions beyond the critical point, only one phase is present; for conditions below this point, two or more phases can simultaneously coexist. On a pressure-volume diagram (Figure 3.1), the critical point is the point of inflection on the critical temperature (T_c) isotherm. Thus, the critical parameters occur when

$$\left(\frac{\partial p}{\partial V}\right)_{T_c,N_a} = \left(\frac{\partial^2 p}{\partial V^2}\right)_{T_c,N_a} = 0 \quad (3.8)$$

which yields

$$\mathcal{Z}\varepsilon\rho_c = \frac{k_bT_c}{1-\rho_c} \quad (3.9a)$$

$$3\mathcal{Z}\varepsilon\rho_c = k_bT_c\frac{2-\rho_c}{(1-\rho_c)^2}. \quad (3.9b)$$

from equation (3.6). Solving equations (3.9) for the critical density, ρ_c, gives $\rho_c = 1/2$, indicating that at the critical point each lattice site has an average occupancy of 50%. Equations (3.9) now reduce to

$$\frac{k_bT_c}{\varepsilon} = \frac{\mathcal{Z}}{4} \quad (3.10)$$

Hence, if T_c and $\mathcal{Z}$ are known, ε is also specified. For water, T_c = 647.3 K. Thus on a two-dimensional (2-D) lattice ($\mathcal{Z}$ = 4), ε is estimated to be 5382 J mol^{-1}. For a three-

dimensional (3-D) system ($\mathcal{Z}$ = 6), ε is estimated to be 3588 J mol^{-1}. By solving equation (3.7) at ρ_c, the critical chemical potential $\bar{\mu}_c$ is

$$\mu_c = -\frac{\mathcal{Z}\varepsilon}{2} \tag{3.11}$$

Therefore, $\mu_c = -2\varepsilon$ for a 2-D lattice and $\mu_c = -3\varepsilon$ for a 3-D lattice. Note that the value of the critical chemical potential is independent of the system temperature.

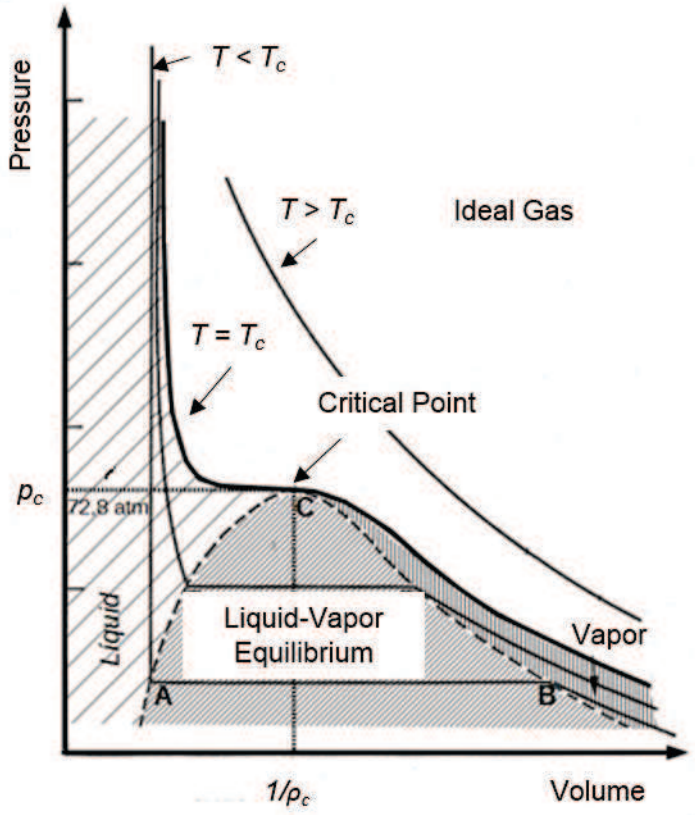

Figure 3.1 Pure component pressure-volume phase diagram. The critical temperature isotherm has a point of inflection at the critical point. Adapted from Antoni Salvà (Own work), via Wikimedia Commons.

Experimentally, the RH is controlled instead of the chemical potential. Thus a relationship between the chemical potential and RH is necessary to predict the dependence of capillary forces on RH. For an ideal gas [149]

$$\mu = k_b T \ln p + \mu^o. \tag{3.12}$$

where μ is the reference chemical potential. The chemical potential at saturation μ_c is

$$\mu_c = k_b T \ln p^S + \mu^o. \tag{3.13}$$

where p^S is the saturation pressure. Combining equations (3.12) and (3.13) and noting that p/p^S = RH leads to

$$\mu - \mu_c = k_b T \ln p/p^S = k_b T \ln \text{RH} \tag{3.14}$$

or by rearrangement

$$\text{RH} = \exp\left(\frac{\mu-\mu_c}{k_b T}\right). \tag{3.15}$$

From equations (3.7), (3.11), and (3.15), the RH is also related to the average occupancy

$$\text{RH} = \frac{\rho}{1-\rho}\exp\left[-\frac{\mathcal{Z}\varepsilon}{2k_b T}(2\rho - 1)\right]. \tag{3.16}$$

With equations (3.7) and (3.16) it is now possible to discuss the thermodynamic behavior of the LDFT model for a pure-component, bulk system as a function of the average occupancy per site. Figure 3.2 shows three μ-ρ isotherms at, above, and below the critical temperature. First, note that the μ-ρ isotherms converge

onto and are symmetric about the critical density at μ_c, which is representative of the critical point. Next for $T > T_c$, there is only one ρ value for every μ. This means that for temperatures greater than the critical temperature there is only one phase, as expected. For $T < T_c$, the number of roots for each chemical potential varies from 1 to 3, which means that more than one phase can simultaneously coexist for a given μ. Finally, the critical isotherm is the transition temperature where the phases converge to the same value. When RH is plotted in place of μ (Figure 3.3), similar behavior is observed, except that the system is no longer symmetric about the critical density.

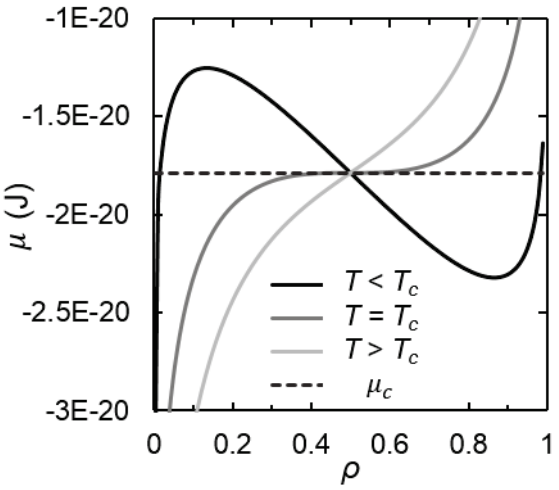

Figure 3.2 The chemical potential as a function of the average occupancy per site from equation (3.7). Three different isotherms in relation to the critical isotherm are represented. Above T_c only one phase exists at a given μ, below T_c more than one phase may coexist.

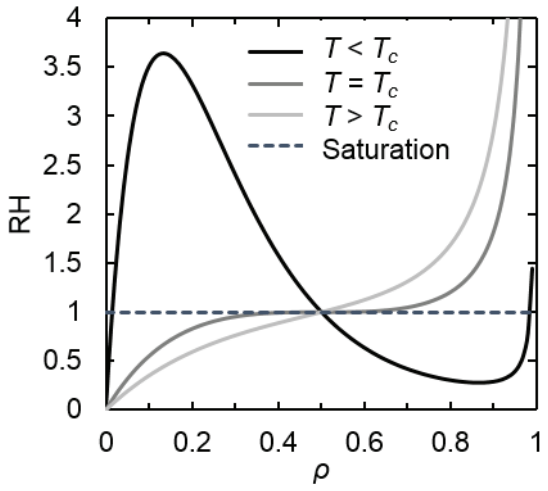

Figure 3.3 RH as a function of the average occupancy per site from equation (3.16) for a two-dimensional lattice. Three different isotherms in relation to the critical isotherm are represented. Above T_c only one phase exists at a given μ, below T_c more than one phase may coexist.

Within the vapor-liquid equilibrium region in Figure 3.1, there exist regions of stability, metastability and instability bounded by the binodal and spinodal curves. As shown on a pressure-volume phase diagram (Figure 3.4), the binodal curve represents the equilibrium coexistence of two phases within a pure-component, bulk system, whereas, the spinodal curve represents the boundary between the metastable and unstable regions [149]. These regions are also represented in the μ-ρ and RH-ρ diagrams. For example, when three roots are possible in Figures 3.2 and 3.3, the root closest to zero represents the stable vapor branch, the root closest to one represents the metastable liquid branch, and the middle root represents the unstable liquid (see Figure 3.5). The binodal curve is represented at $\mu = \mu_c$ and RH = 1. The spinodal occurs at the transition between the metastable and unstable liquid branches. Any chemical potential or RH below the spinodal value can only converge to the

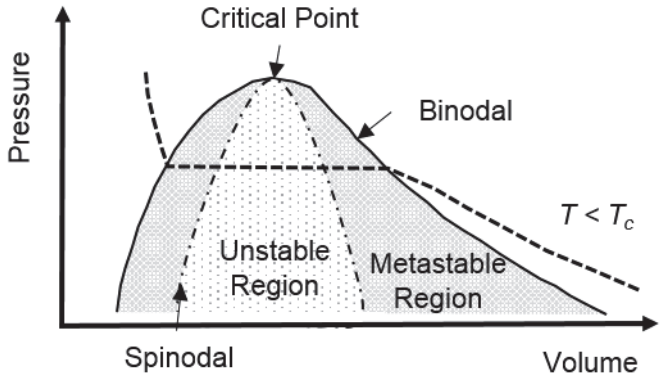

Figure 3.4 Pressure-volume phase diagram illustrating the stable, metastable, and unstable regions at a given temperature.

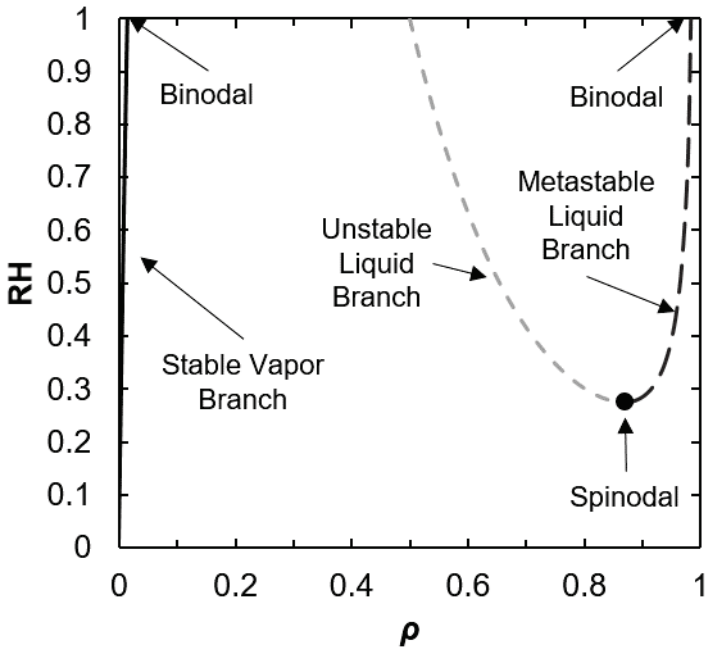

Figure 3.5 RH-ρ phase diagram illustrating the stable, metastable, and unstable regions at $T < T_c$ from equation (3.16) for a two-dimensional lattice. For RH values less than the spinodal, only the stable vapor phase exists.

stable vapor branch because there is no corresponding metastable liquid branch. This is an important result, as it suggests that below the RH that corresponds to the spinodal limit, it is not possible to form two phases in equilibrium. Hence any prediction of a liquid-vapor interface (at least for a single-component system) in that region becomes an unphysical extrapolation.

3.3 Simulation of a Bulk System

The preceding analysis assumes that the occupancy at each site is equal to the average occupancy of all other sites ($\rho_i = \sum_i \rho_i / N_{tot}$). This assumption is reasonable for a non-constrained, bulk system, but is not valid for systems that involve external forces such as molecular adsorption to walls. Hence, it is necessary to allow each site on the lattice to optimize its density according to the density of its nearest neighbors. However, it is expected that the simulated LDFT results of a bulk, pure-component system will match exactly the results of the preceding section, as will be demonstrated.

For the LDFT simulations, it is most convenient to operate in the grand canonical ensemble where the temperature, total volume, and chemical potential of the system are held constant. This ensemble allows the number of molecules in the system to fluctuate for a given μ. The total energy of the system is represented by the grand potential, Ω, which is related to the Helmholtz energy by

$$\Omega = \mathcal{F} - \mu N_a. \tag{3.17}$$

Therefore, for a pure-component system without any external fields, equation (3.4) becomes [132], [135], [141]

$$\Omega(\{\rho_i\}) = k_b T \sum_i [\rho_i \ln \rho_i + (1-\rho_i)\ln(1-\rho_i)] - \frac{\varepsilon}{2}\sum_i \rho_i \sum_{j=NN} \rho_j - \mu \sum_i \rho_i \quad (3.18)$$

by recognizing that $N_a = \sum_i \rho_i$. ρ_i is the average occupancy at each site and the summations over i are over the total number of sites, whereas the summation over j includes only the nearest neighbors of site i. Equation (3.18) can be made non-dimensional by dividing by ε:

$$\bar{\Omega}(\{\rho_i\}) = \theta \sum_i [\rho_i \ln \rho_i + (1-\rho_i)\ln(1-\rho_i)] - \frac{1}{2}\sum_i \rho_i \sum_{j=NN} \rho_j - \bar{\mu} \sum_i \rho_i \quad (3.19)$$

where $\bar{\Omega} = \Omega/\varepsilon$, $\theta = k_b T/\varepsilon$, and $\bar{\mu} = \mu/\varepsilon$ (the bar indicates that the quantity is without units).

The thermodynamic metastable and stable energies are found by minimizing $\bar{\Omega}$ with respect to ρ_i, i.e., $\left(\frac{\partial \bar{\Omega}}{\partial \rho_i}\right)_{\bar{\mu},T} = 0$. Solving for ρ_i at the minimized $\bar{\Omega}$ yields

$$\rho_i = \left[1 + \exp\left(-\frac{1}{\theta}\left[\bar{\mu} + \sum_{j,i=NN}\{\rho_j\}\right]\right)\right]^{-1}. \quad (3.20)$$

After initializing the system, equation (3.20) is solved using a successive iteration method (*i.e.*, the previous set of densities is used to predict the next set of densities) [133]. This process repeats until $(1/N_{tot})\sum_i (\rho_i^{n+1} - \rho_i^n)^2 < 10^{-16}$, where the subscript n is the nth iteration [133]. This procedure prevents the system from sampling saddle points and/or maxima in the free energy domain, thus optimizing the

search for the minimum of the free energy [132], [135], [141]. Once the minimized $\{\rho_i\}$ is found, equation (3.19) is used to determine the stabilized (meta-stabilized) $\overline{\Omega}$.

To compare the bulk simulations to the bulk prediction shown in Figure 3.5, equations (3.19) and (3.20) are solved for a two-dimensional, 100 x 100 lattice with periodic boundary conditions at T = 300 K or θ = 0.4625. Since this is below T_c, there are multiple roots possible. Hence, the system is initialized with random densities between 0 and 0.1 to investigate the stable vapor behavior of the system. Similarly, the system is initialized with random densities between 0.9 and 1 to investigate the metastable liquid branch. Then the system is allowed to reach equilibrium for RH values between 0.01 and 1 in 0.01 increments. These results are plotted on Figure 3.6.

Even though each site on the lattice is initially different from its neighboring sites, the optimized set of densities across the entire lattice converges to one bulk value. This is an expected result, since the goal is to simulate a bulk system in the absence of external fields. Therefore at each level of RH, there is only one value of ρ_i to report. As can be seen in Figure 3.6, below RH of 0.28, ρ_i for systems initialized close to zero and for systems initialized close to one both converge onto the stable vapor branch, as there is not any metastable liquid branch on which to converge. Above RH of 0.28, ρ_i for the vapor-initialized system converges onto the predicted vapor branch, and ρ_i for the liquid-initialized system converges onto the metastable liquid branch. Additionally, the system never converges onto the unstable liquid branches. Clearly, the LDFT simulations are reproducing expected trends for a bulk system. This is necessary to ensure before investigating two-phase phenomena

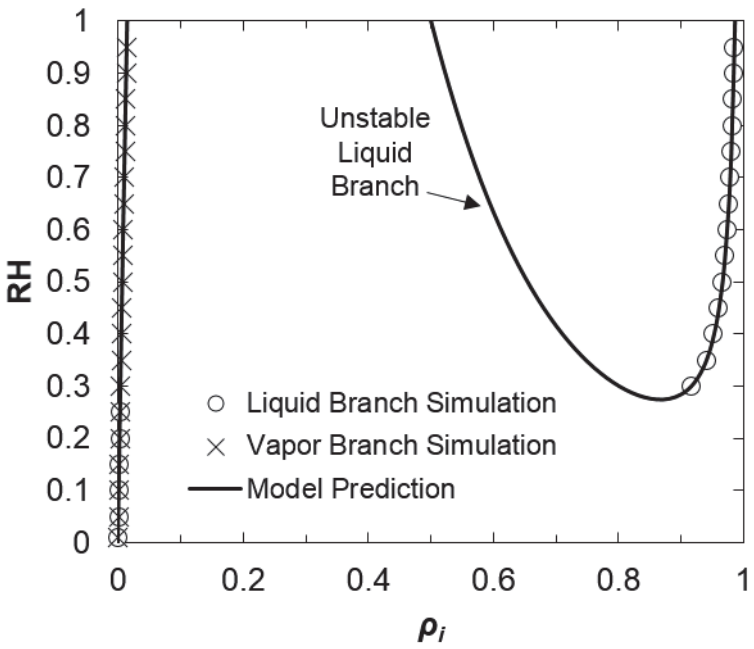

Figure 3.6 Comparison between equation (3.16) and the LDFT simulation of a pure-component, bulk system at T = 300 K for a two-dimensional, 100x100 lattice.

that have inhomogeneous density profiles as will be discussed in the following sections.

3.4 Properties of the Planar Interface and Dividing Surfaces

An interface is caused by the convergence and coexistence of two or more bulk, stable or metastable phases. For a two-phase, pure-component system at the binodal (RH = 1), the normal pressures on either side of the interface are equal and the interface is planar [22]. As this is the simplest type of interface, it is instructive to define its properties before investigating the effects of pressure differences and curvature. Only the most pertinent details of the analysis will be presented here, but

the interested reader is referred to the work of Ono and Kondo [22] for a more extensive presentation of interfaces and surface energies.

Consider a vapor and a liquid separated by a planar interface (Figure 3.7). A cubic element of volume V containing a representative sample of the bulk liquid, interface, and bulk vapor will exhibit an inhomogeneous density profile that transitions from high to low density in the direction normal to the interface (Figure 3.8). The transition region is not a step function, but is instead continuous, indicating that it has a thickness or depth and so cannot always be accurately described as an infinitely-thin, massless membrane. The energy of this interface/transition region is referred to as an excess energy $\overline{\Omega}^{ex}$, which is determined by subtracting the energetic contributions of the bulk liquid and vapor as if there were no interface ($\overline{\Omega}^{\mathrm{L}}$ and $\overline{\Omega}^{G}$, respectively) from the total energy of the system with an interface, $\overline{\Omega}$:

$$\overline{\Omega}^{ex} = \overline{\Omega} - (\overline{\Omega}^{L} + \overline{\Omega}^{G}). \tag{3.21}$$

In general, the grand potential is defined as $\overline{\Omega} = -pV/\varepsilon$, therefore $\overline{\Omega}^{L} = -p_L V_L/\varepsilon$ and $\overline{\Omega}^{V} = -p_G V_G/\varepsilon$, where L and G refer to the liquid and vapor states, respectively. The excess energy can be expressed as

$$\overline{\Omega}^{ex} = \overline{\Omega} - (-pV_L - pV_G)/\varepsilon \; = \overline{\Omega} + p(V_L + V_G)/\varepsilon = \overline{\Omega} + pV/\varepsilon, \tag{3.22}$$

since the interface is planar (i.e., $p = p_L = p_G$) and V does not change with the location of the dividing surface. The surface energy or surface tension $\bar{\gamma}_{\infty}$ of a planar interface is then

$$\bar{\gamma}_{\infty} = \bar{\Omega}^{ex}/\bar{A}_I. \tag{3.23}$$

where $\bar{A}_I$ is the area of the interface divided by σ^2.

It is important to note that the surface energy of the interface γ is generally dependent on the location of the dividing surface. It is independent for the planar case in part because $\bar{A}_I$ is the same no matter where the interface is located within the cubic segment. However, $\bar{A}_I$ increases with increasing radii for a spherical interface, such as with a droplet or bubble, thus the choice of the dividing surface will affect the value of the surface tension. Hence, it is useful to present the different types of dividing surfaces that are available, their meanings, and how they are determined.

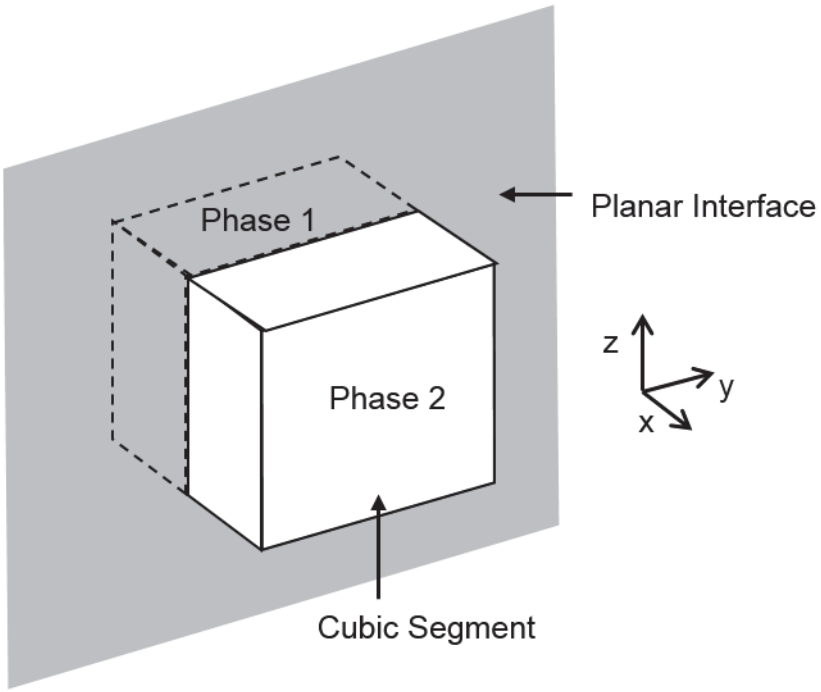

Figure 3.7 Schematic of planar interface separating two phases. The properties of the interface can be examined by considering a cubic segment containing a representative sample of the bulk phases and interface.

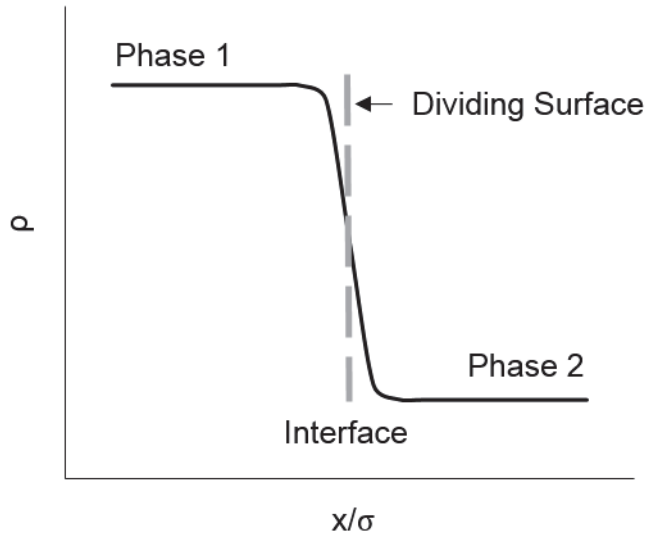

Figure 3.8 A typical density profile for an interface in a two-phase system. σ represents the diameter of one molecule of water.

The equimolar dividing surface $\bar{X}_e$ is the point at which the number of moles on the vapor side of the interface equals the number of moles on the liquid side of the interface. For the planar case, it is the value at which

$$\int_{-\infty}^{\bar{X}_e}[\rho(x) - \rho^G]\,\mathrm{d}x = \int_{\bar{X}_e}^{\infty}[\rho^L - \rho(x)]\mathrm{d}x \tag{3.24}$$

is satisfied. Equation (3.24) is integrated over the density profile $\rho(x)$ of the system in the direction normal to the interface and ρ^L and ρ^G are the bulk liquid and vapor densities, respectively. This dividing surface is primarily used in determining the Tolman length, which has been used to quantify the deviation of the surface tension from its bulk value as a function of curvature [150].

A more useful dividing surface is known as the surface of tension or $\bar{X}_s$, which conveniently becomes the only location for which the Young-Laplace equation

assumes its traditional form and is implicitly assumed when invoking the Young-Laplace equation. It is defined as the point where the surface tension is independent of changes in the mathematical displacement of the interface, all other factors being held constant [22], [31] or as the dividing surface at which the surface tension reaches a minimum value with respect to the location of the dividing surface. This physically corresponds to the location along the direction normal to the interface where the surface tension appears to act in order to balance the forces in the liquid and vapor phases. For a planar interface, this physical definition is the most useful for calculating $\bar{X}_s$.

In order to calculate the forces acting on the interface and the moment, the non-dimensional normal and transverse pressures ($\bar{p}$ and $\bar{p}_T$, respectively) as a function of position in the normal direction must be known. For the cubic segment in Figure 3.7, the normal pressure is the $\bar{p}_{xx}$ component of the pressure tensor and the transverse pressure is the $\bar{p}_{yy}$ and $\bar{p}_{zz}$ components of the pressure tensor (note that $\bar{p}_{yy} = \bar{p}_{zz}$). The normal pressure can be calculated as a function of position using equation (3.6). The transverse pressure is determined by calculating the grand potential at each position $\bar{\Omega}_i$ and dividing it by $\bar{V}_o$:

$$\bar{p}_{T,i}(x) = -\bar{\Omega}_i/\bar{V}_o \tag{3.25}$$

where $\bar{V}_o = V_o/\sigma^3$. Or by invoking equation (3.19)

$$\bar{p}_{T,i}(x) = -\left[\theta[\rho_i \ln \rho_i + (1-\rho_i)\ln(1-\rho_i)] - \frac{1}{2}\rho_i \sum_{j=NN} \rho_j - \bar{\mu}\rho_i\right]/\bar{V}_o. \tag{3.26}$$

In terms of the transverse pressure, the total force acting on the interface is

$$\int \bar{p}_T(x) w \mathrm{d}x \tag{3.27}$$

where w is the width of the interface (see Figure 3.9). In terms of the normal pressure, the total force can also be expressed as

$$-\bar{\gamma}_\infty w + \int \bar{p}(x) w \mathrm{d}x. \tag{3.28}$$

Note that the surface tension is defined to be positive. By equating equations (3.27) and (3.28), the planar surface tension becomes

$$\bar{\gamma}_\infty = \int [\bar{p}(x) - \bar{p}_T(x)] \mathrm{d}x. \tag{3.29}$$

Note also that equation (3.29) and equation (3.23) are equal. To find the location at which the surface tension appears to act, the total moment must also be determined. Since the moment is the force multiplied by the distance from an axis, the total moment in terms of the transverse pressure is

$$\int x \bar{p}_T(x) w \mathrm{d}x, \tag{3.30}$$

and in terms of the normal pressure is

$$-\bar{\gamma}_\infty w \bar{X}_s + \int x \bar{p}(x) w \mathrm{d}x. \tag{3.31}$$

Equations (3.30) and (3.31) lead to

$$\bar{\gamma}_\infty \bar{X}_s = \int x [\bar{p}(x) - \bar{p}_T(x)] \mathrm{d}x. \tag{3.32}$$

Therefore, by invoking equation (3.29)

$$\bar{X}_s = \frac{\int x [\bar{p}(x) - \bar{p}_T(x)] \mathrm{d}x}{\int [\bar{p}(x) - \bar{p}_T(x)] \mathrm{d}x}. \tag{3.33}$$

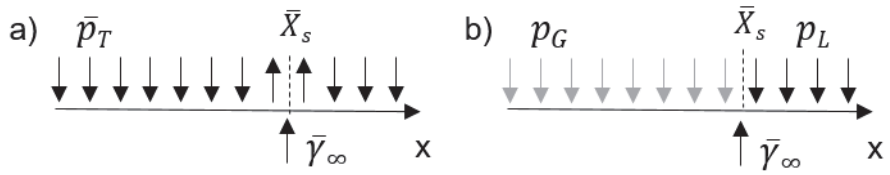

Figure 3.9 Schematic demonstrating the a) transverse pressure and b) normal pressure approaches to calculating the total force and moment for a planar interface. The planar interface is located at the surface of tension or $\bar{X}_s$. The length of the arrow (not to scale) represents the magnitude of the force caused by the normal or transverse pressure. The up or down direction of the arrow represents the direction the force acts at a given position. The pressure-induced forces are balanced by the planar surface tension acting at the surface of tension. In b), the gray arrows represent the bulk pressure in the vapor, the black arrows represent the bulk pressure in the liquid.

Again, equation (3.33) represents the location of the dividing surface where the surface tension appears to act.

With both the equimolar and surface of tension dividing surfaces defined, the Tolman length for the planar limit is

$$\delta = \bar{X}_e - \bar{X}_s. \tag{3.34}$$

With the theory in place, the properties of a planar interface are simulated using the LDFT model by once again creating a 2-D 100x100 lattice at 300 K and RH is 1. Since the temperature is below T_c, a liquid and vapor phase can coexist (see Figure 3.5). The system is initialized by filling half of it (with respect to the x-axis) with vapor ($\rho_i = 0$) and the other half with liquid ($\rho_i = 1$). This artificially creates or assigns the interface to be in the center of the simulation. Reflective boundary conditions are imposed to maintain the symmetry of the interface.

As expected, minimizing the free energy of the system according to equation (3.20) leads to a planar, liquid-vapor interface in the center of the simulation (see

Figure 3.10). The density profile, as shown in Figure 3.11, remains constant and close to zero for the bulk or region of the simulation. It then sharply, but continuously, transitions to the bulk liquid density at the interface. The transverse pressure, plotted on the secondary axis of Figure 3.11, is constant and equal to the normal pressure of the system throughout the bulk phases, but then sharply decreases within the interfacial region. From these two profiles and equations (3.24), (3.33), (3.34) and (3.29), $\bar{X}_e = 47.5$, $\bar{X}_s = 48.1$, $\bar{\gamma}_\infty = 0.394$ (= 33.5 mJ m^{-2}) and $\delta = \pm 0.6$ (= ± 0.2 nm). Note that the Tolman length can be either positive or negative depending on whether the starting phase is bulk liquid or vapor.

The LDFT model clearly under-predicts the bulk surface tension of water, which is approximately 71 mJ m^{-2} at 300 K [151]. Yet this is to be expected because intermolecular attraction energy is defined solely by the number of bonds per site and the critical temperature (see equation 3.10). Hence there is no leniency in the lattice-gas model that allows hydrogen bonding to occur, which is a significant contributor to the surface tension of water. Though its prediction of the surface tension is low, the LDFT construction can still be used to demonstrate the effect of the curvature on the surface tension. Traditionally, the surface tension's curvature dependence has been determined by the Tolman length as used in the Gibbs-Tolman-Koenig-Buff equation [22], [150], [152]–[154]. However, because δ is a function of the curvature itself, the utility of a Tolman length analysis is quite limited [153]. Therefore, a thermodynamic approach using excess energy as is readily available in the LDFT model will be used in the following sections to show the dependence of the surface tension on the

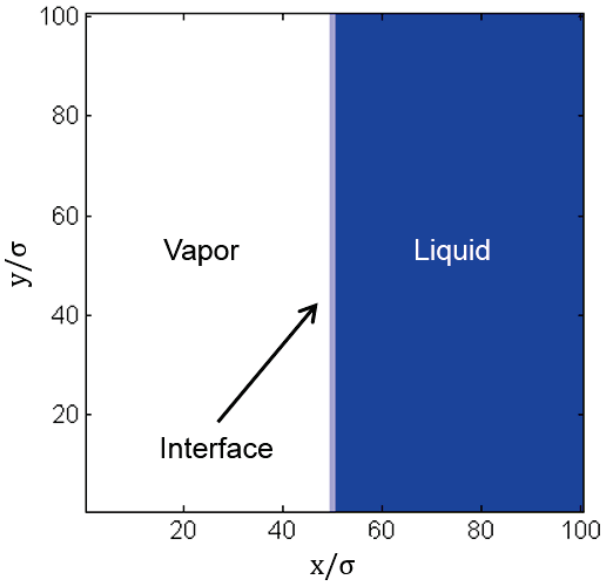

Figure 3.10 LDFT simulated planar liquid-vapor interface on a 2-D 100x100 lattice at 300 K with reflective boundary conditions. The dark blue corresponds to dense liquid, the light blue indicates a dense vapor, and white indicates a vapor phase.

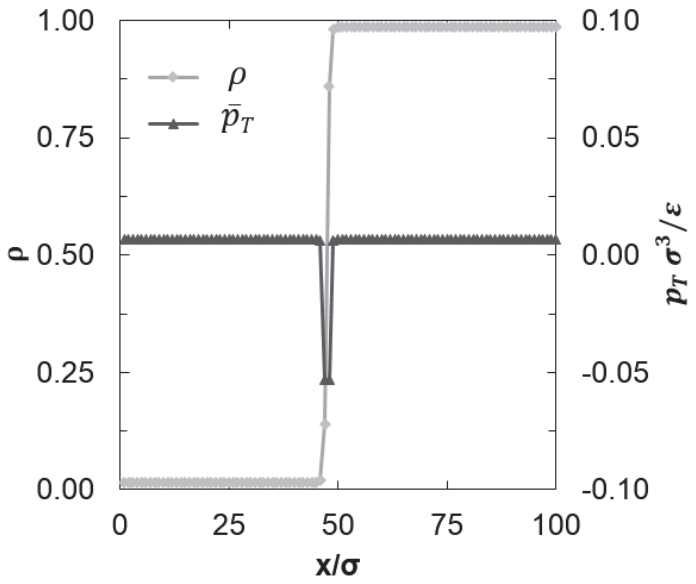

Figure 3.11 The non-dimensional density (light gray diamonds, primary axis) and transverse pressure (dark gray triangles, secondary axis) as a function of position for a planar interface. Note the sharp transition in both the density and the transverse pressure at the interface.

curvature of the interface. In this manner the Tolman method of analysis is circumvented altogether.

3.5 Curvature Dependence of the Surface Tension for a Two-Phase System

With the characteristics of a planar interface solidly established, the properties of a curved interface in a two-phase, pure component system can be investigated. The introduction of curvature implies that the bulk pressures on either side of the interface are no longer equal. As first demonstrated by Lord Kelvin [155], the pressure difference across the interface (as quantified by the curvature of the interface) is also related to the saturation of the system, or in this case the RH, and is described by the Kelvin equation (equation (1.21)). For a bulk, pure-component, two-phase system, the Kelvin equation is accurate. However, at low humidity or high interfacial curvature, its application is tenuous because the liquid-vapor surface tension and liquid molar volumes may no longer be independent of saturation and interfacial curvature. Therefore, the LDFT simulations can be compared against the Kelvin equation to verify the LDFT model's accuracy in bulk systems. Additionally, the LDFT model can investigate deviations from the Kelvin equation in non-ideal situations because interfacial curvatures can be thermodynamically determined without assuming a value for the liquid-vapor surface energy or the liquid molar volume.

A two-phase system consisting of a bubble within a metastable bulk liquid has been simulated. This system has been chosen because capillary bridges between two surfaces are generally concave with respect to the vapor. The goal of these simulations is to investigate the properties of curved interfaces spanning from the

spinodal to the binodal, yet LDFT simulations are numerically unstable near the spinodal (i.e., for bubbles of small radii). To circumvent this numerical issue, a constraint has been introduced into the LDFT model using the method of Lagrange multipliers [31], [135], [141].

Consider a system with two regions: inside a bubble and outside a bubble (Figure 3.12). For an unconstrained system, the chemical potential is imposed in both regions. For a constrained system, the chemical potential is only imposed on the outside region, whereas the total number of molecules within the bubble is fixed. Both regions interact to optimize the imposed chemical potential outside and the constraint inside the bubble. Assigning the number of molecules within the bubble automatically assigns the chemical potential within the bubble. Hence, the chemical potentials across the interface are not necessarily equal in the constrained system. However, the constraint stabilizes the simulation by guaranteeing that the center region has the assigned density regardless of possible numerical instabilities.

Following the method in [31], [135], the total energy of the system can be split into inside and outside regions:

$$\begin{aligned}\bar{\Omega}(\{\rho_i\}) = \theta \sum_i^{out} [\rho_i \ln \rho_i + (1-\rho_i)\ln(1-\rho_i)] - \frac{1}{2}\sum_i^{out} \rho_i \sum_{j=NN} \rho_j - \\ \bar{\mu}\sum_i^{out} \rho_i + \theta \sum_i^{in} [\rho_i \ln \rho_i + (1-\rho_i)\ln(1-\rho_i)] - \\ \frac{1}{2}\sum_i^{in} \rho_i \sum_{j=NN} \rho_j + \bar{\kappa}\left(n - \sum_i^{in} \rho_i\right) - n\bar{\mu}\end{aligned} \tag{3.35}$$

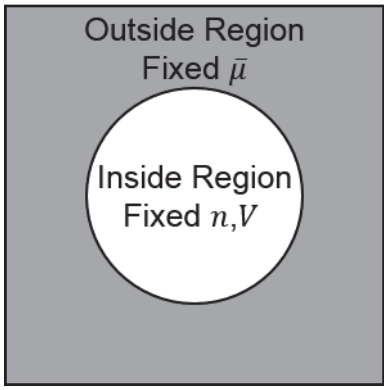

Figure 3.12 Inside and outside regions for a bubble in metastable liquid used in the constrained LDFT method.

The summation over the outside region includes all lattice sites outside of the bubble radius and the summation over the inside region includes all lattice sites inside of the bubble. $\bar{\kappa}$ is the Lagrange multiplier and represents the chemical potential inside of the bubble and n is the total number of molecules within the bubble. As before, the free energy of the system is minimized by taking the partial derivatives of $\overline{\Omega}$ of the inside and outside regions with respect to ρ_i. This leads to

$$\rho_i = \left[1 + \exp\left(-\frac{1}{\theta}\left[\bar{\mu} + \sum_{j,i=NN}\{\rho_j\}\right]\right)\right]^{-1} \tag{3.36}$$

for the outside region and

$$\rho_i = \left[1 + \exp\left(-\frac{1}{\theta}\left[\bar{\kappa} + \sum_{j,i=NN}\{\rho_j\}\right]\right)\right]^{-1} \tag{3.37}$$

or

$$\bar{\kappa} = \theta \ln\left(\frac{\rho_i}{1-\rho_i}\right) - \sum_{j,i=NN}\{\rho_j\} \tag{3.38}$$

for the inside region. The constraint within the bubble can be expressed as

$$\sum_i^{in} \rho_i = n \tag{3.39}$$

and when applied to equation (3. 37), it leads to

$$(N_0 - n)\exp(\bar{\kappa}/\theta) = \sum_i^{in} \rho_i \exp\left(-\frac{1}{\theta}\sum_{j,i=NN}\{\rho_j\}\right) \tag{3.40}$$

where N_0 is the total number of lattice sites within the bubble. By combining equations (3.38) and (3.40), an iterative solution to the local densities within the bubble is established:

$$\rho_i = \left[1 + \frac{N_0 - n}{\left[\exp\left(-\frac{1}{\theta}\sum_{j,i=NN}\{\rho_j\}\right)\sum_i^{in}\rho_i\right]\exp\left(\frac{1}{\theta}\sum_{j,i=NN}\{\rho_j\}\right)}\right]^{-1}. \tag{3.41}$$

The free energy of the system is then minimized with the same iteration scheme described previously, except that for each iteration of equation (3.36), equation (3.41) is solved until the local densities do not change within the bubble. In this manner, both the imposed chemical potential and the constraint of a fixed number of molecules are satisfied. To locate the critical bubble size for a given RH, the number of molecules is iteratively changed until $\bar{\kappa}$ and $\bar{\mu}$ are equal, which indicates that the system is in equilibrium and that the density profile across the interface is continuous.

Once the minimized free energy of the critical bubble is established, the curvature of the liquid-vapor interface and the surface tension can be investigated using the thermodynamic approach described by equations (3.21)-(3.23). However, since the pressures across the interface are no longer equal, equation (3.22) becomes

$$\overline{\Omega}^{ex} = \overline{\Omega} + (p_{ref}V_G + pV_L)/\varepsilon. \tag{3.42}$$

p_{ref} is the reference pressure of the critical bubble and can be defined in two different ways. The traditional approach defines the reference pressure to be equal to the pressure of the bulk vapor at the chemical potential of the system (from equation (3.6)). The alternative approach defines the reference pressure as the transverse pressure at the center of the critical bubble [31]. For bubbles large enough to exhibit bulk properties in the interior, the two definitions yield the same results. Close to the spinodal however, Corti *et. al.* [31] demonstrate that the two approaches deviate in their predictions. As the transverse pressure more accurately represents the behavior within the interior of the critical bubble, it has been used to define the reference hereafter.

Like the planar case, the surface of tension is also the dividing surface of interest for curved interfaces. This is because it is the surface where the Kelvin equation is specifically defined, it represents the radius of curvature of the interface, and it corresponds to the minimum of the surface tension. The surface of tension is the circle of radius $\bar{R}_s$ which entirely encompasses the cylindrical bubble, while minimizing the free energy of the interface as represented by $\overline{\Omega}^{ex}$. Hence, it is found by minimizing equation (3.23). Assuming that $V_G = \pi\bar{R}^2$, $V_L = N_{tot} - \pi\bar{R}^2$, and $\bar{A}_I = 2\pi\bar{R}$ for a 2-D cylindrical bubble, equation (3.23) becomes

$$\bar{\gamma}_{LG} = \overline{\Omega}^{ex}/\bar{A}_I = \frac{\overline{\Omega} + \bar{p}_{ref}\pi\bar{R}^2 + \bar{p}(N_{tot} - \pi\bar{R}^2)}{2\pi\bar{R}}. \tag{3.43}$$

and both the optimized surface tension of the liquid-vapor interface and the surface of tension can be determined (Figure 3.13).

The equimolar surface can also be determined for comparison by finding the circle of radius $\bar{R}_e$ which satisfies

$$\sum_i^{N_{tot}} \rho_i = \rho^L(N_{tot} - \pi\bar{R}_e^2) + \rho_c^G \pi\bar{R}_e^2 \tag{3.44}$$

where ρ_c^G is the density of the site at the center of the bubble.

The bubbles have been modeled on a 2-D 100x100 lattice (corresponding to cylindrical bubbles in 3-D space) at 300 K with RH varying from 0.01 to 0.99 in 0.01 increments. Reflective boundary conditions have been imposed to maintain the symmetry. Initially, $\rho_i = n/N_0$ inside of the bubble and $\rho_i = 1$ outside of the bubble. For each RH level the optimum bubble radius and number of molecules has been iteratively determined by changing the number of molecules in the bubble until the chemical potential of the bubble matches that of the surrounding liquid.

Figure 3.14 contains the LDFT density map for a bubble in metastable liquid at 300 K and RH = 0.90 and the corresponding density profile of the bubble in the radial direction. In Figure 3.14a, the deeper the blue, the denser the component is at that lattice site; hence, a bubble has been formed in the center of the simulation. The black line around the bubble represents the surface of tension of the bubble and the yellow line marks the 0.5 density line. Clearly, the surface of tension as estimated by minimizing equation (3.43) is a reasonable representation of the radius of curvature of the liquid-vapor interface. Additionally, the density profile again resembles that of a planar interface (Figure 3.14b) with a continuous but sharp transition between the

vapor and the liquid. The transverse pressure again has a sharp decrease within the interfacial region like that of the planar case, but now the bulk pressure on the inside of the bubble is greater than the bulk pressure in the surrounding liquid. Hence there is a pressure difference across the interface, which is to be expected based on the Young-Laplace equation. Finally, the equimolar dividing surface and the surface of tension are in good agreement for this simulation close to the binodal. Similar results were found for each RH value from the spinodal to the binodal.

As shown in Figure 3.15, the radius of curvature of the interfaces (defined to be at the surface of tension) corresponds directly to the Kelvin equation (black line) for most RH levels. Because the Kelvin equation is derived specifically for a pure-component, two-phase system at the surface of tension, it is encouraging that the LDFT model for a pure-component, two-phase system at the surface of tension also predicts a similar behavior without assuming a value for the surface tension or liquid molar volume. This strongly suggests that the LDFT model is capable of accurately predicting interfacial curvatures for other systems where the application of the Kelvin equation is questionable. It is also interesting to note that the agreement between the Kelvin equation and the LDFT simulations deviate as the RH approaches the spinodal limit of 0.28. This is because there is no metastable liquid branch below this RH level (see Figure 3.6). Hence the LDFT simulations offer an important insight that the Kelvin equation is an unphysical extrapolation for very low RH values when the radius of curvature approaches the size of one molecule (Figure 3.15a).

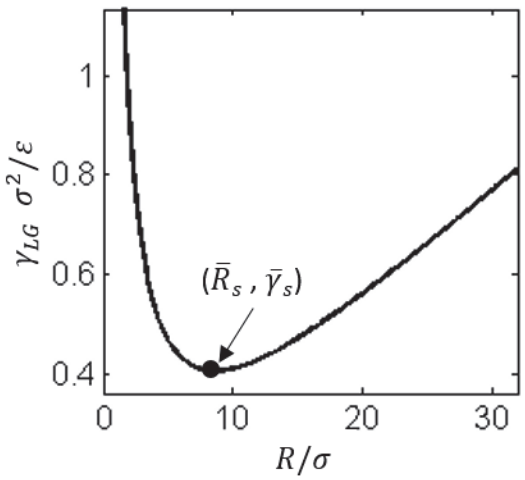

Figure 3.13 The surface tension as a function of the size of the dividing surface for a bubble in metastable liquid (equation (3.43)). The minimum corresponds to the surface of tension $\bar{R}_s$ and the optimized surface tension for a liquid-vapor interface $\bar{\gamma}_s$.

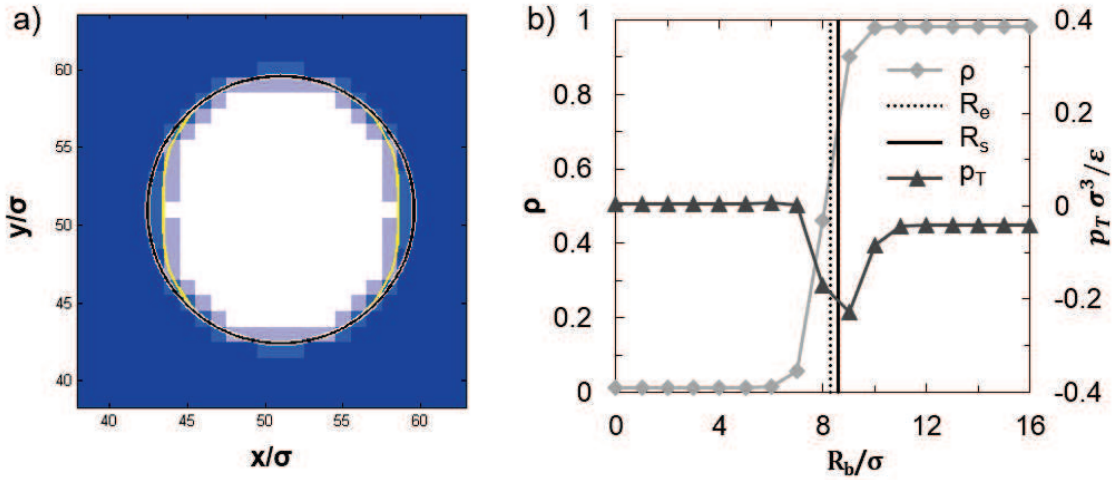

Figure 3.14 LDFT density map for a bubble within a metastable liquid and its corresponding density profile. a) Density map of a bubble within a metastable liquid. The deeper the blue, the more liquid-like the phase at a given site. The black line represents the surface of tension and the yellow line represents the 0.5 density line. b) The density profile, equimolar dividing surface, surface of tension, and transverse pressure as a function of the radial distance from the bubble center R_b. The transverse pressure corresponds to the secondary axis.

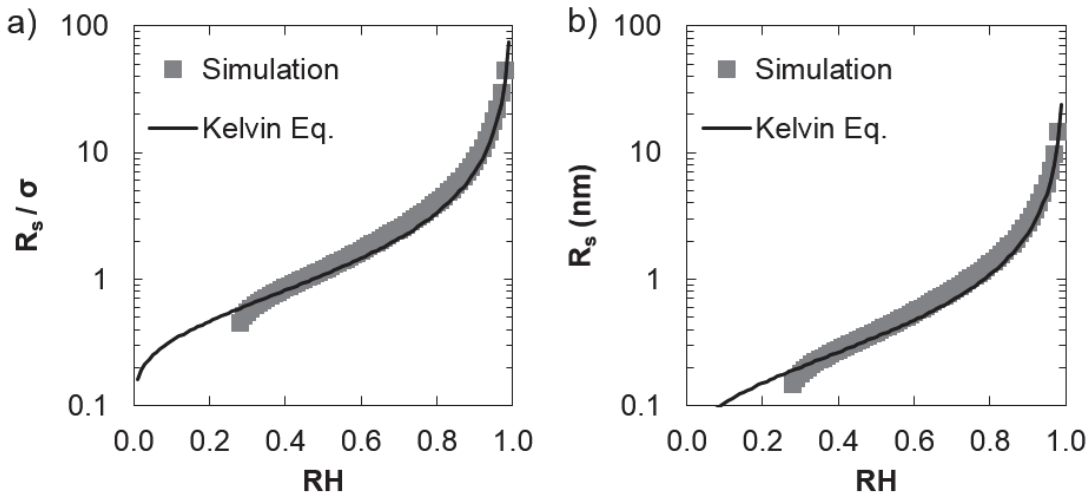

Figure 3.15 Radius of curvature of an interface as a function of RH. a) Non-dimensional plot and b) dimensional plot. The gray squares are the simulation results and the black line is the Kelvin equation.

To further illustrate this point, the surface tension has been plotted as a function of the radius of curvature of the interface (Figure 3.16). As can be seen for large radii of curvature, the surface tension can be considered constant and equal to that of the planar interfacial surface tension. However, for very small radii of curvature the surface tension is considerably dependent on the curvature of the interface and rapidly approaches zero. Therefore, the assumption commonly applied to both the Young-Laplace equation and the Kelvin equation of constant surface tension is only applicable for RH values where the predicted radius of curvature is greater than 2 molecular diameters (Figure 3.16a). Near the spinodal, the effect of curvature on the surface tension must be accounted for in the Kelvin Equation.

In summary, the LDFT simulations of a bubble in a metastable liquid are in good agreement with the traditional Kelvin equation except for RH levels below or near the spinodal. In this region, the Kelvin equation is either an unphysical

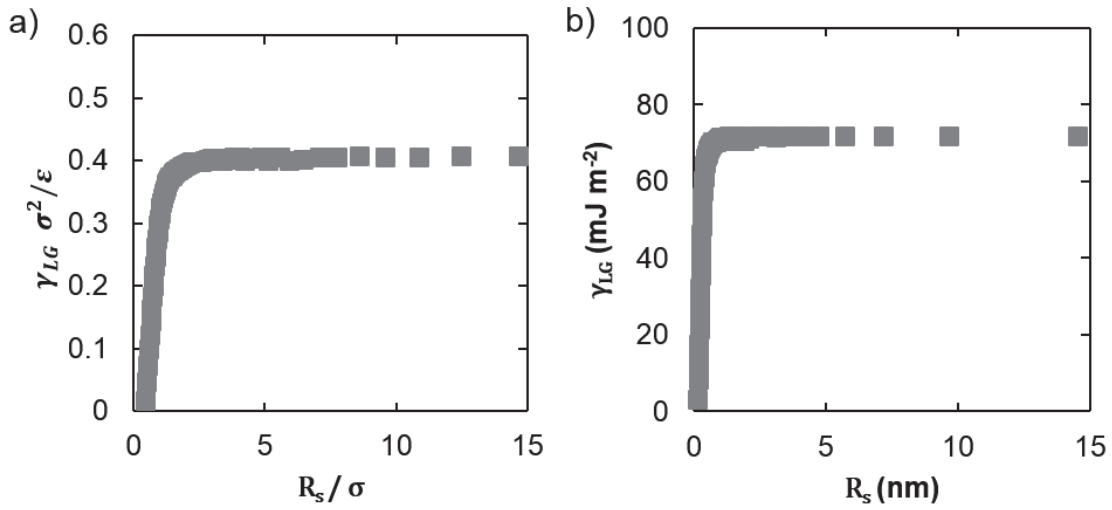

Figure 3.16 Surface tension of a liquid-vapor interface as a function of the surface of tension. a) Non-dimensional plot and b) dimensional plot corresponding to the bulk surface tension of water (71 mJ m^{-2}).

extrapolation (beyond the spinodal) or must account for the dependence of the surface tension on the curvature of the interface in order to be properly applied.

3.6 Radii of Curvature of Liquid Bridges between Walls of Varying Hydrophilicity

With the method of estimating the radii of curvature of interfaces firmly established within the LDFT framework, the more complicated system of a liquid bridge between two parallel planes can now be simulated and the results compared against the Kelvin equation.

Consider a lattice-gas system where N_x is the number of lattice sites in the x-direction and N_z is the number of lattice sites in the z-direction or the separation between the two walls (Figure 3.17). The left half of the simulation ($x < N_x/2$) is unconstrained (*i.e.,* no walls), whereas the right half of the simulation ($x \geq N_x/2$)

has two walls of fixed hydrophilicity at the top and bottom of the system. Both walls have the same hydrophilic properties. The left half of the simulation represents the bulk vapor portion whereas the right half represents the portion under the influence of the walls. Reflective boundary conditions are again employed to maintain symmetry. This configuration allows a liquid bridge to form an equilibrium meniscus with a bulk vapor without constraining the system.

The total energy of this system is

$$\bar{\Omega}(\{\rho_i\}) = \theta \sum_i [\rho_i \ln \rho_i + (1-\rho_i)\ln(1-\rho_i)] - \frac{1}{2}\sum_i \rho_i \sum_{j=NN} \rho_j - \beta_w \sum_{i,j=NN} \left[\rho_i(1-\eta_j) + \rho_j(1-\eta_i)\right] - \bar{\mu}\sum_i \rho_i \tag{3.45}$$

where β_w is the energy of adsorption of a molecule onto a wall divided by ε (in other words a measure of the hydrophilicity), and η_i is the matrix occupancy (whether or not a site is adjacent to a wall). The addition of β_w is an example of an external field acting over the right half of the system. It is the influence of this external field on the radius of curvature of the liquid-vapor interface that is of interest.

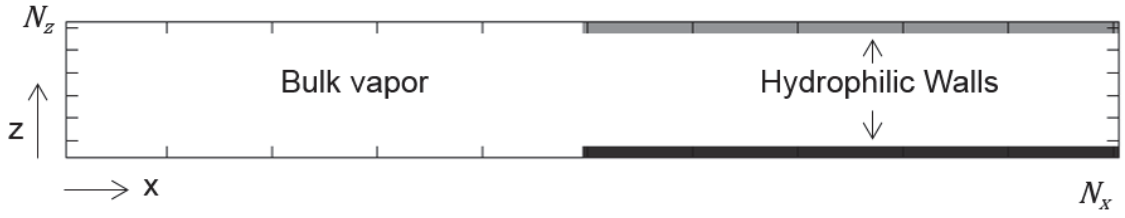

Figure 3.17 Lattice system in the x-z plane for two parallel, hydrophilic walls surrounded by bulk vapor.

As is done in the previous cases, minimizing equation (3.45) with respect to ρ_i yields

$$\rho_i = \left(1 + \exp\left(-\frac{1}{\theta}\left[\bar{\mu} + \sum_{j,i=NN}\{\rho_j + \beta_w(1-\eta_j)\}\right]\right)\right)^{-1} \qquad (3.46)$$

The minimum of the free energy and optimized density profile of the simulation is then found by solving equations (3.45) and (3.46) using the same iteration scheme as described for the bulk and planar cases. The resulting density maps at the minimum of the free energy of the system exhibited three different types: vapor throughout the system; layers of water adsorbed to the walls, but no liquid bridge; and a liquid bridge (Figure 3.18). The first type corresponds to hydrophobic walls, where the vapor does not readily adsorb (Figure 3.18a). The second type represents the case where the vapors readily adsorb, but the separation between the two plates is too large to sustain a liquid bridge (Figure 3.18b). The final situation occurs when the hydrophilicity of the plates is great enough and the separation between them is close enough to condense the vapor into a liquid bridge (Figure 3.18c). Though the first two have interesting applications, it is the third situation that is studied here.

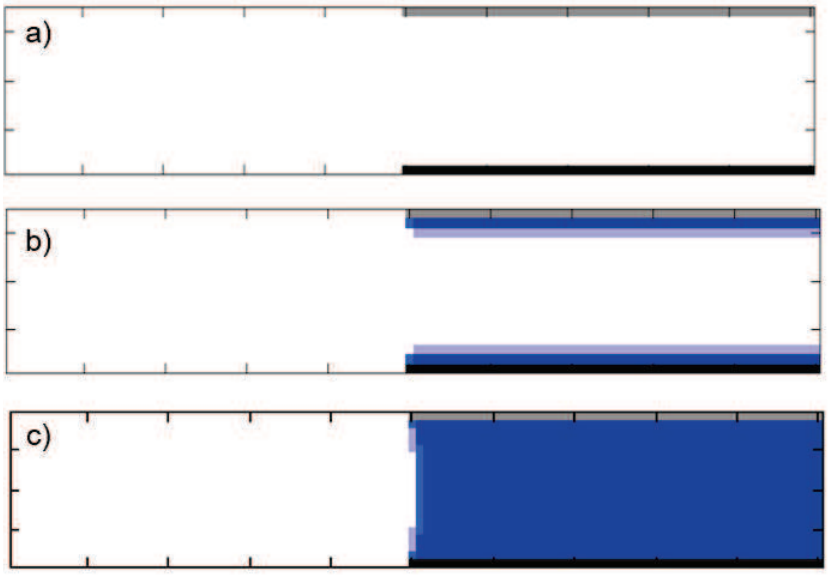

Figure 3.18 Three possible results of the LDFT simulations for two parallel walls surrounded by bulk vapor. a) Hydrophobic walls, no liquid phase, b) hydrophilic walls with adsorbed liquid layers and c) hydrophilic walls and a liquid-bridge with a curved meniscus. The deeper the blue the more dense the phase at the site. The black and gray lines indicate the parallel walls.

3.6.1 Surface of Tension via the Minimization of the Excess Free Energy

The liquid-vapor interface forms a curved meniscus in Figure 3.18c. The radius of curvature of this interface can be estimated using a method similar to that of the bubble within a metastable liquid. First, the liquid-bridge system is recreated by filling the left half with bulk vapor and the right half with bulk liquid. Then bulk vapor in the shape of a circular segment can be added at the center of the simulation while bulk liquid filling the same circular segment is subtracted. In this manner, the liquid-vapor interface can be mathematically reconstructed (see Figure 3.19).

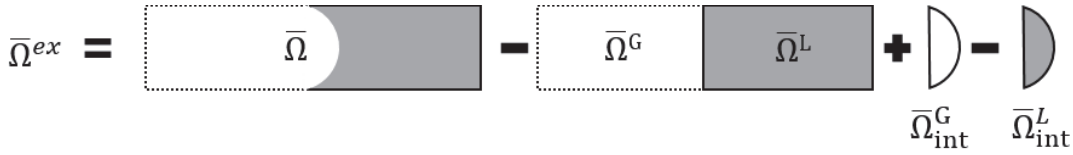

Figure 3.19 Illustration of the method of recreating the liquid-bridge system. This is required to calculate the excess energy.

Similar to equation (3.21), the excess free energy is calculated via

$$\overline{\Omega}^{ex} = \overline{\Omega} - \overline{\Omega}^{L} - \overline{\Omega}^{G} + \overline{\Omega}^{G}_{int} - \overline{\Omega}^{L}_{int} \tag{3.47}$$

where $\overline{\Omega}^{G}_{int}$ is the free energy of the vapor in the circular segment and $\overline{\Omega}^{L}_{int}$ is the free energy of the liquid bridge within the same circular segment. Assuming that the walls extend infinitely into and out of the page, the system can be properly represented in two dimensions. Hence, the bulk free energy in the vapor $\overline{\Omega}^{G}$ is calculated by multiplying the bulk pressure in the vapor by the area of the left-hand side of the simulation. Since the presence of the walls introduces solid-vapor and solid-liquid interfacial tensions into the system, the bulk free energy of the liquid $\overline{\Omega}^{L}$ is determined by summing the transverse pressures in the z-direction at the center of the liquid bridge and multiplying it $N_x/2$. Assuming that the interface will be approximately circular, $\overline{\Omega}^{G}_{int}$ is estimated by multiplying the pressure of the bulk vapor by the area of the circular segment, $\bar{A}_{int}$. Finally, $\overline{\Omega}^{L}_{int}$ is estimated by integrating the transverse pressure at the center of the liquid bridge over the area of the circular segment. As a result, the excess free energy of the system is

$$\overline{\Omega}^{ex} = \overline{\Omega} - \frac{N_x}{2}\int \overline{\Omega}_{i,x=N_x} \mathrm{d}z + p^V \frac{N_z N_x}{2} - p^V \bar{A}_{int} - \int \overline{\Omega}_{i,x=N_x} \mathrm{d}\bar{A}_{int}. \tag{3.48}$$

The surface energy of the liquid-vapor interface is then

$$\bar{\gamma}_{LG} = \bar{\Omega}^{ex}/\bar{P}_{int} \tag{3.49}$$

where $\bar{P}_{int}$ is the perimeter of the circular segment. Both the area and the perimeter of the circular segment are functions of the position of the circle and the radius of the circle:

$$\bar{A}_{int} = \begin{cases} \bar{R}_s^2 \operatorname{acos}(a/\bar{R}_s) - a\sqrt{\bar{R}_s^2 - a^2}, & c \le \frac{N_z}{2} \\ \bar{R}_s^2 \operatorname{acos}(a/\bar{R}_s) - a\sqrt{\bar{R}_s^2 - a^2} - 2\int_{\frac{N_z}{2}}^{\frac{c}{2}} \sqrt{\bar{R}_s^2 - y^2} - a \, \mathrm{d}y, & c > \frac{N_z}{2} \end{cases} \tag{3.50a}$$

$$\bar{P}_{int} = \begin{cases} 2\bar{R}_s \operatorname{asin}\left(\frac{c}{2\bar{R}_s}\right), & c \le \frac{N_z}{2} \\ 2\bar{R}_s \operatorname{asin}\left(\frac{N_z}{2\bar{R}_s}\right), & c > \frac{N_z}{2} \end{cases} \tag{3.50b}$$

where c is the length of the chord given by $c = 2\sqrt{\bar{R}_s^2 - a^2}$, and a is the distance of the center of the circle to $N_x/2$ (Figure 3.20). These equations assume that the meniscus between the walls is always concave with respect to the vapor and that $a < \bar{R}_s$.

The surface of tension and the optimum surface tension are now determined by locating the minimum of equation (3.49) with respect to both $\bar{R}_s$ and a. Figure 3.21 shows the typical shape of the surface tension of a liquid-bridge as a function of the position and radius of the dividing surface. Generally, a global minimum is expected for each liquid-bridge configuration; however, due to numerical issues caused by integrating over a lattice configuration, the global minimum does not always correspond to the correct interfacial curvature. Additionally, the minimum of equation (3.49) is shallow, numerically difficult to distinguish from local minima,

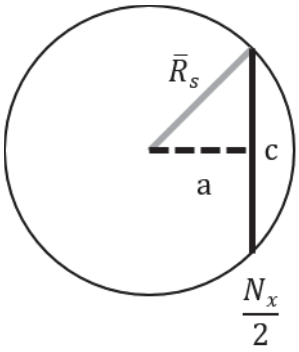

Figure 3.20 Geometry of a circular segment. The radius of the circle $\bar{R}_s$ corresponds to the light gray line. The distance from the center of the circle to the middle of the simulation a is the dashed black line and the length of the chord c is the solid black line.

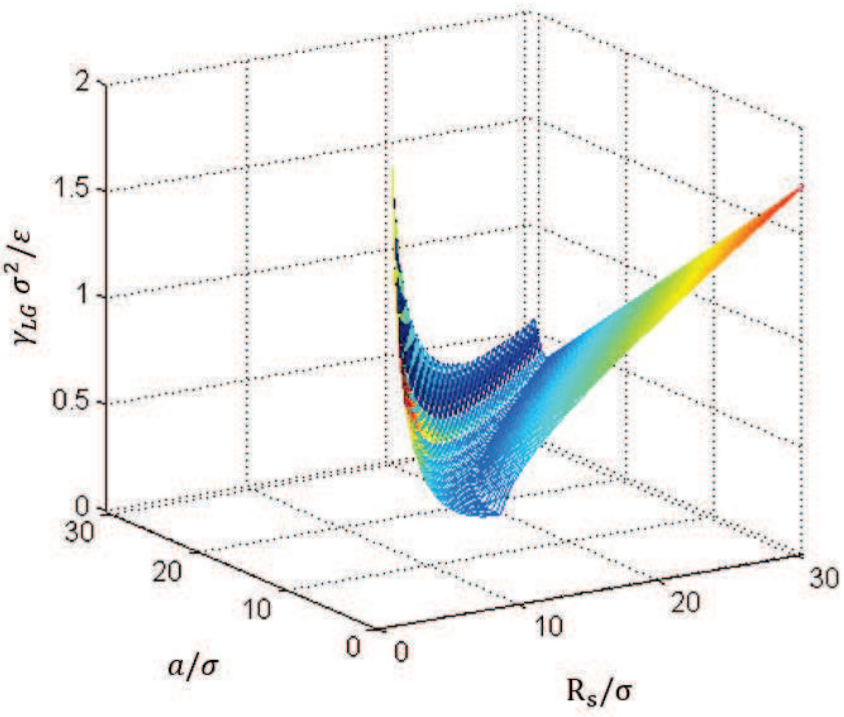

Figure 3.21 The surface energy of the curved interface between two parallel walls as a function of the position of the circle and the radius of the dividing interface.

and often converges to the arbitrarily determined maximum of R_s within the simulation program. Any results that automatically converge to this maximum limit are not presented here because they are not representative of the true curvature of the interface. Indeed, these instances likely indicate that the interface may be approaching a planar or infinite curvature. Thus, the optimum circle which describes the interfacial curvature is defined as that which (1) properly converges, (2) minimizes the surface tension, and (3) minimizes the distance between the edge of the circle and the 0.5 density line of the simulation at $N_z/2$. In this manner, reasonable estimations of the surface of tension have been obtained.

The effect of the RH, plate separation distance and the hydrophilicity of the walls has been studied at 300 K. The RH is allowed to vary from 0.01 to 1 in 0.01 increments. The separation of the walls varies from 1 to 18 lattice units, while N_x is fixed at 100 lattice units. Following the method presented by Monson [134], the relationship between the affinity of the vapor to the wall β_w and the contact angle ϕ has been determined by invoking Young's equation (equation (1.5)), where the solid-vapor and solid-liquid surface energies have been determined from excess grand free energies of LDFT simulations involving only solid-vapor and solid-liquid interfaces. The relationship between β_w and ϕ is shown in Figure 3.22. In this manner, the hydrophilicity of the tip can vary in the simulations from completely wetting ($\beta_w = 1$, $\phi = 0°$) to hydrophobic ($\beta_w = 0.5$, $\phi = 90°$) in increments of 15°. The case where the walls have a higher affinity to the adsorbing vapor than the vapor has to itself has also been studied and is considered a super-hydrophilic surface ($\beta_w = 1.5$, $\phi = 0°$). This differs from the completely wetting case only in that the affinity of the adsorbate

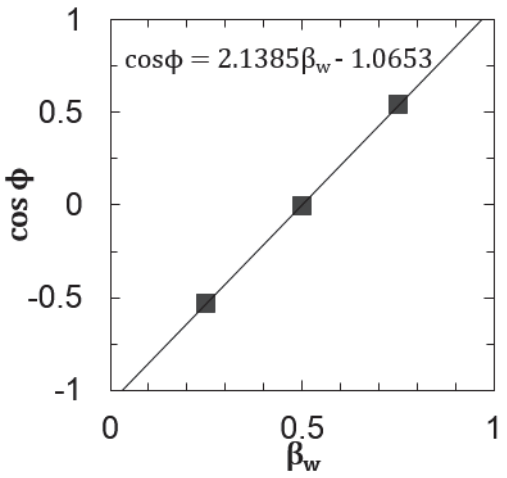

Figure 3.22 Correlation between the contact angle ϕ and β_w. The gray squares are LDFT simulations performed by the method described by Monson [134]. The equation represents the least-squares fit ($R^2 = 1$) and the trend line.

to the surface is greater, while both contact angles are the same. In order to ensure that liquid-bridges form, the system has been initialized by filling the left half with vapor ($\rho_i = 0$) and the right half with liquid ($\rho_i = 1$). Finally, no results derived from a negative excess energy are shown because this causes a negative interfacial surface tension, which is unphysical.

A representative liquid bridge is shown in Figure 3.23 for super-hydrophilic walls at RH = 0.8 and N_z = 12. The black circle represents the surface of tension and the yellow line represents the 0.5 density line. As can be seen, the surface of tension appropriately describes the radius of curvature of the liquid-vapor interface. This result is the same for walls of varying hydrophilicity and separation distances, except for RH levels near saturation where the interface tends toward the planar case.

For super-hydrophilic walls, the predicted surface of tension and interfacial surface tensions at a given RH and wall separation distances of 1, 5 and 10 lattice

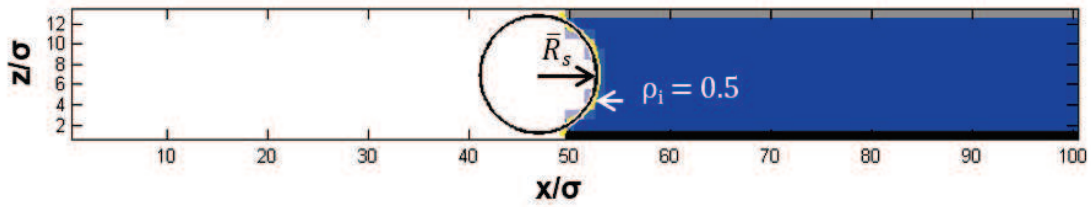

Figure 3.23 Curvature of a liquid bridge between super-hydrophilic walls at 300 K. RH = 0.80 and N_z = 12. The black circle represents the surface of tension and the yellow line represents the 0.5 density line. The deeper the blue the more dense the phase at the site. The black and gray lines indicate the parallel walls.

sites are shown in Figure 3.24. The solid black line represents the Kelvin equation, the dashed black line is the planar surface tension limit, and the symbols represent the simulated results, where lighter gray symbols represent larger wall separation. The numbers indicate which plate separation distance corresponds to which set of simulated results.

In Figure 3.24a, the surface of tension for a wall separation distance of one lattice site corresponds to the situation of a monolayer of liquid between the walls. At RH levels above 0.05, this becomes an extreme case that more closely resembles vapor in contact with a heterogeneous surface than that of a curved liquid-vapor interface between solid plates. Hence at these RH levels the simulation typically converges to the arbitrary maximum value, which is why only two RH levels for super-hydrophilic surfaces are plotted here. The important thing to note, is that the close proximity of the surfaces allows the vapor to condense at very low RH levels primarily due to the strong affinity of the adsorbing vapor to the walls.

A similar phenomenon is observed when the wall separation is increased to five lattice sites (Figure 3.24c). Although, here the formation of a liquid bridge

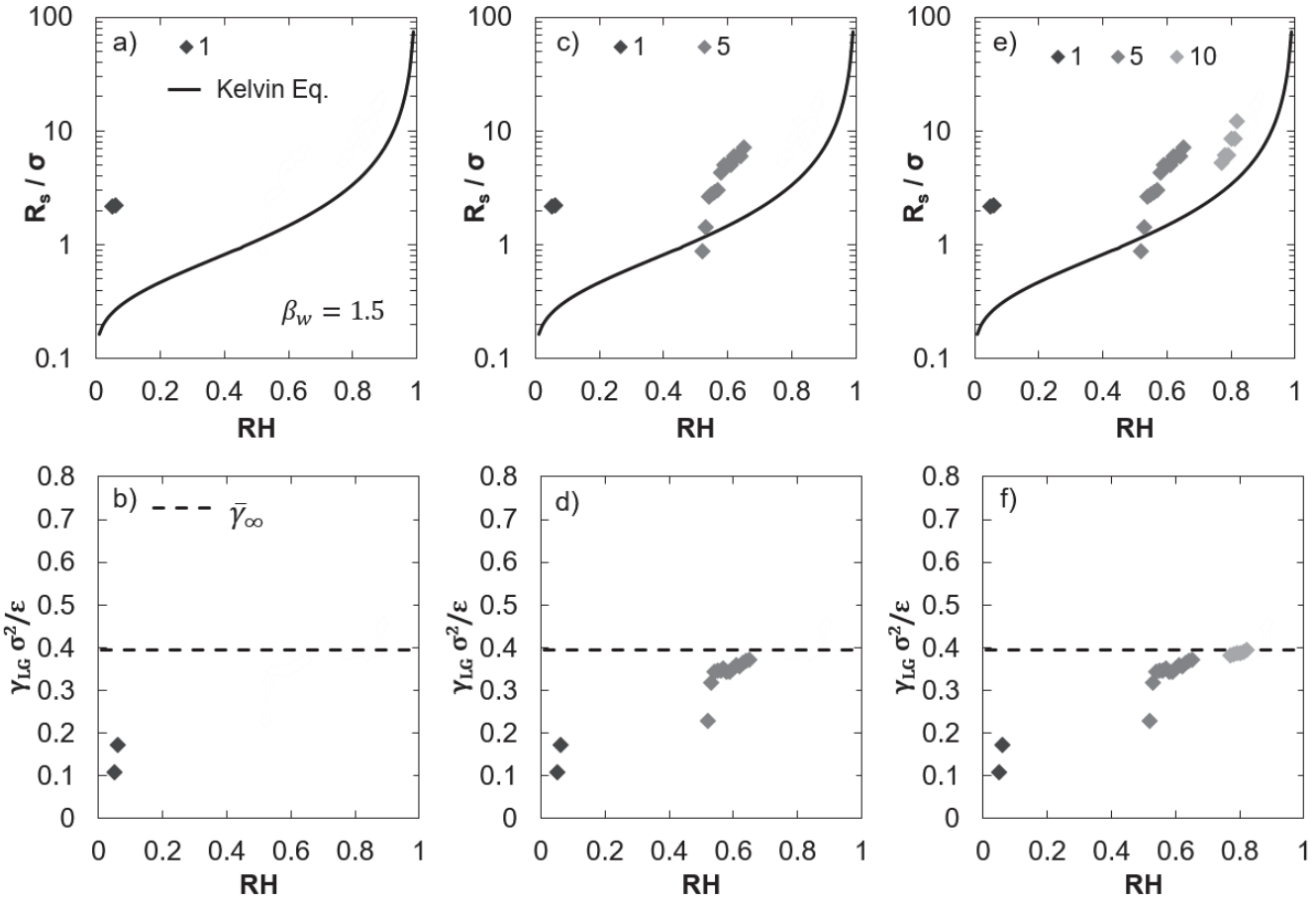

Figure 3.24 Properties of a liquid bridge between two super-hydrophilic ($\beta_w = 1.5$, $\phi = 0^o$) parallel plates at 300 K obtained by minimizing the excess free energy. The numbers indicate the plate separation distance h/σ. a,c,e) Surface of tension vs. RH. Black line represents the Kelvin equation. b,d,f) Surface tension vs. RH. Dotted black line is the planar surface tension.

occurs at RH around 0.5 instead of 0.02. This is expected because a higher saturation is required to fill a larger space and the walls have less influence on the overall behavior of the system. The adsorption to the walls initiates liquid-bridge formation at low RH Subsequent increases in system saturation allow the system to relax and the liquid more readily interacts with the vapor allowing the radius of curvature to increase. Figure 3.25 shows the initial curvature of a liquid bridge and its eventual saturation independence for super-hydrophilic walls separated by three lattice sites at RH = 0.3 and 0.4. Similar trends are observed when the separation distance is increased to ten lattice sites (Figure 3.24e).

Like the surface tension for a bubble in a metastable liquid, the surface tension of a curved meniscus (Figures 3.24b,d,f) approaches zero as the RH approaches the limit of stability of liquid-bridge formation at a given wall separation. This suggests that for each separation distance there is a spinodal limit beyond which no liquid bridge may form. It also suggests that the influence of super-hydrophilic walls can stabilize the formation of a liquid phase at levels beyond the spinodal limit (lower than 0.28 RH for 300 K), thus causing capillary effects at very low humidity levels. This is an important effect to consider while working with hydrophilic surfaces experimentally. Finally, note that the surface tension tends toward the planar limit near saturation and for large separation distances.

The predicted surface of tension and interfacial surface tensions at a given RH and wall separation distances of 1-18 lattice sites for different contact angles including the super-hydrophilic case are shown in Figure 3.26. The lines and symbols

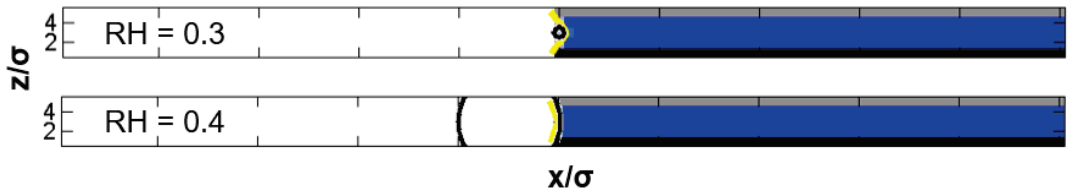

Figure 3.25 Curvature of a liquid bridge for super-hydrophilic walls separated by three lattice sites at N_z = 3 and RH = 0.3 and 0.4. The black circle represents the surface of tension and the yellow line represents the 0.5 density line. The deeper the blue the more dense the phase at the site. The black and gray lines indicate the parallel walls.

are the same as before, remembering that lighter gray symbols represent larger wall separations.

As expected, an increase in the contact angle (decrease in wall hydrophilicity) increases the RH at which a liquid-bridge can form for a given separation distance. For example, in Figures 3.26a, c, and e, the liquid-bridge for a separation distance of one lattice site forms at RH levels of 0.02, 0.28 and 0.36 respectively. This is because the influence of the walls changes the spinodal limit as the contact angle changes. Thus, for a contact angle of 75°, a RH of about 0.8 is required before any capillary condensation can occur (Figure 3.26m). Additionally, as the separation distance between the plates increases, the simulations tend toward the Kelvin equation. This suggests that for high system saturation, the Kelvin equation may be a reasonable estimate of interfacial curvature. As illustrated with the super-hydrophilic case, the radii of curvature of the interfaces tend to gradually increase even as the contact angle increases. Thus, the mechanism of liquid-bridge formation is the same for different contact angles, only the point of formation changes.

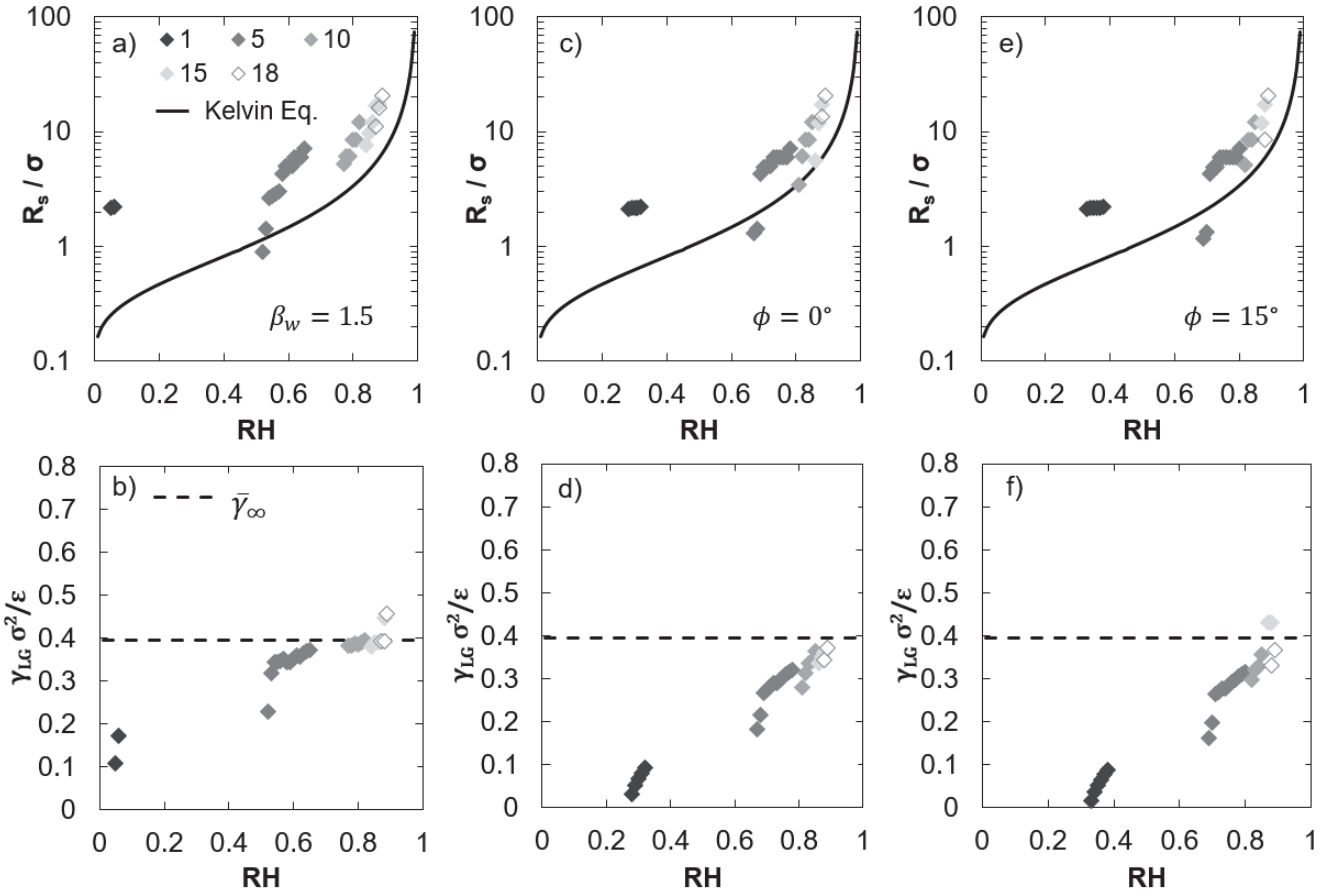

Figure 3.26 Properties obtained by minimizing the excess free energy of a liquid bridge between two parallel plates of varying hydrophilicity at 300 K. The numbers indicate the plate separation distance h/σ. a,c,e) Surface of tension vs. RH at $\beta_w = 1.5$, $\phi = 0^o$, and $\phi = 15^o$, respectively. Black line represents the Kelvin equation. b,d,f) Corresponding surface tension vs. RH at $\beta_w = 1.5$, $\phi = 0^o$, and $\phi = 15^o$, respectively. Dotted black line is the planar surface tension.

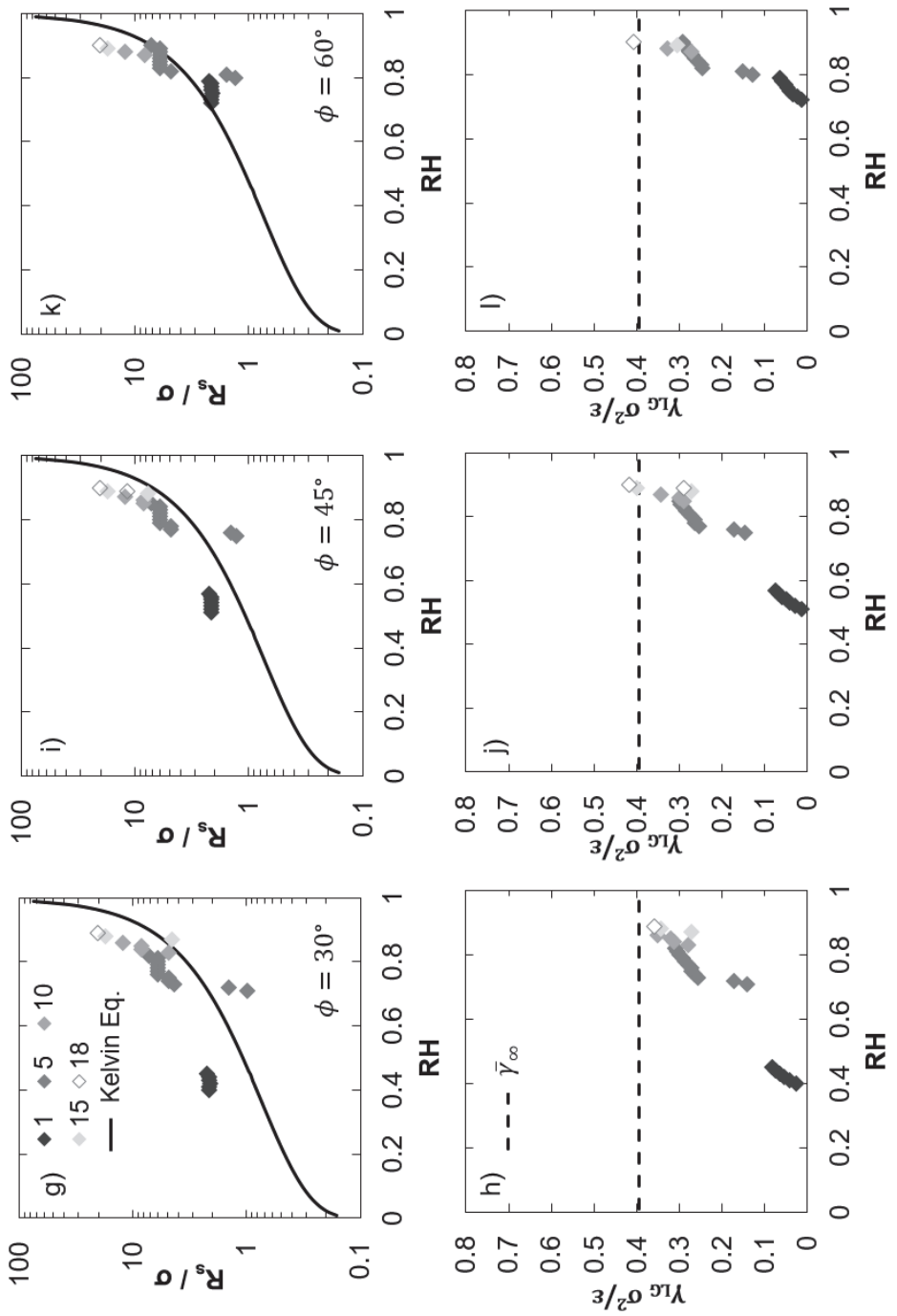

Figure 3.26 Continued g,i,k) Surface of tension vs. RH at $\phi = 30^o$, $\phi = 45^o$, and $\phi = 60^o$, respectively. Black line represents the Kelvin equation. h,j,l) Corresponding surface tension vs. RH at $\phi = 30^o$, $\phi = 45^o$, and $\phi = 60^o$, respectively. Dotted black line is the planar surface tension.

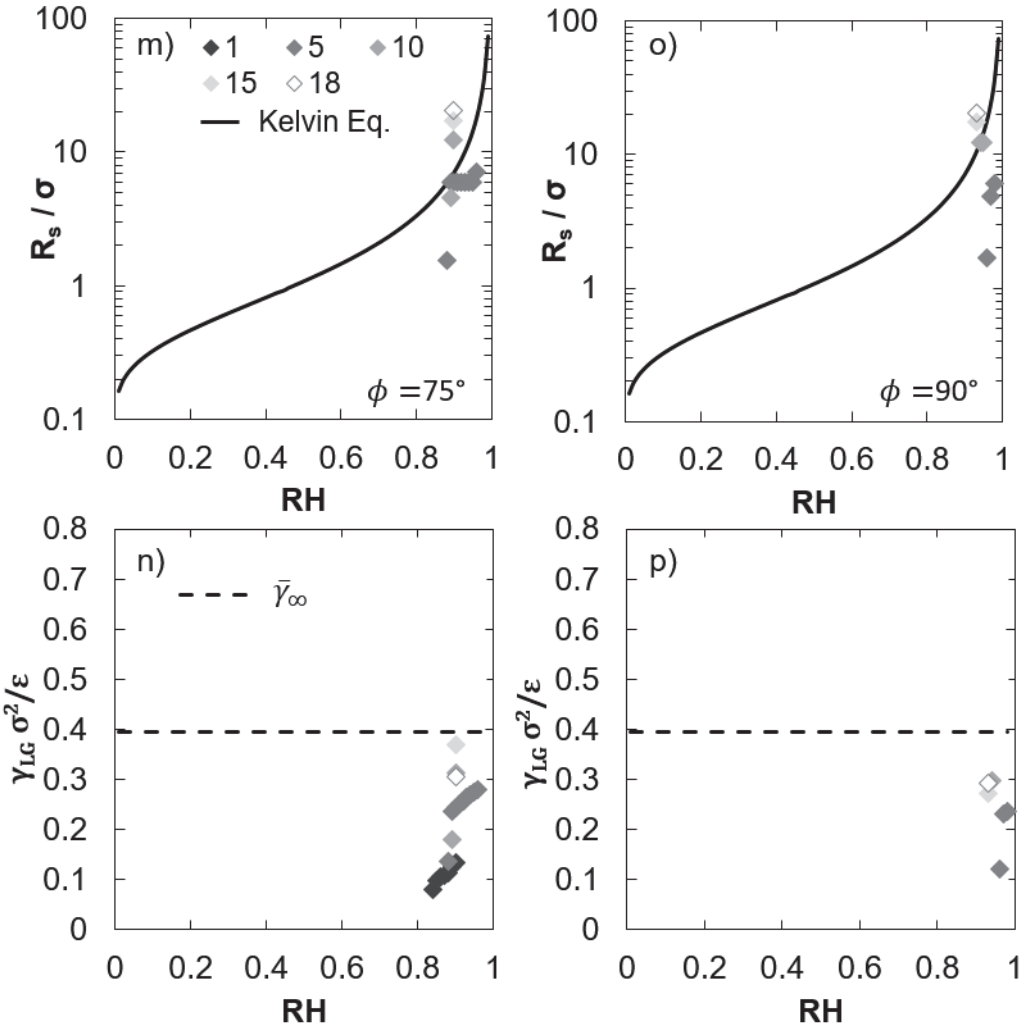

Figure 3.26 Continued m,o) Surface of tension vs. RH at $\phi = 75^o$, $\phi = 90^o$, respectively. Black line represents the Kelvin equation. n,p) Corresponding surface tension vs. RH at $\phi = 75^o$, $\phi = 90^o$, respectively. Dotted black line is the planar surface tension.

It is interesting to note that as the contact angle increases, the liquid-bridges at the closest separation distances actually disappear, meaning that the walls are now sufficiently repulsive to the vapor that the close contact impedes the formation of a vapor. However, as the system approaches RH = 1 and the separation distance is large enough, the effect of the walls is small and stable liquid bridges form without regard

to surface hydrophilicity. This behavior is representative of hysteresis in real experiments.

In summary, Figures 24 and 26 clearly show that the curvature of a liquid-vapor interface between two solid plates is a function of the system saturation, plate separation, and surface hydrophilicity.

3.6.2 Surface of Tension via the Young-Laplace Equation

Alternatively, the curvature of a liquid bridge between two plates can also be adequately described by the Young-Laplace equation (equation (1.4)) because the simulations are static and bulk-like pressures are maintained on either side of the interface. Therefore, only the pressure difference across the interface and the surface tension of the interface is required to calculate the radius of curvature of a liquid bridge between parallel plates. Assuming an infinite curvature into and out of the page, equation (1.4) becomes

$$\bar{R}_s = \frac{\bar{\gamma}_{LG}(\bar{R}_s)}{\Delta P} \tag{3.51}$$

As demonstrated with a bubble in metastable liquid, the surface tension is a function of the curvature of the interface (Figure 3.16). By fitting the simulated surface tension vs. bubble curvature to an exponential function using the method of least squares regression ($R^2_{adj} = 0.995$), the dependence of the surface tension on the curvature of the interface is approximately

$$\bar{\gamma}_{LG}(\bar{R}_s) = 0.4037\exp(-0.0002005\bar{R}_s) - 1.403\exp(-2.678\bar{R}_s) \tag{3.52}$$

Note that this equation corresponds to the non-dimensional surface tension and $\bar{R}_s$ is normalized by the length between lattice sites (σ).

Figure 3.27 shows the dependence of the absolute value of the pressure drop across the interface on the absolute radius of curvature as obtained from equations (3.50) and (3.51). Note first that there is a maximum pressure difference (ca. 0.31) beyond which there is no solution to equation (3.50). This means that when the LDFT simulation predicts a higher pressure difference, the curvature cannot be accurately described by the Young-Laplace equation and other physical phenomena are likely dominating the behavior of the system as is the case with strong wall interactions at small separation distances. Additionally, it can be seen that below this maximum pressure difference there are two possible radii of curvature corresponding to a given pressure difference. An iteration scheme has been developed to select either the first or the second solution (radius of curvature) based on the saturation of the system. Extracting the appropriate pressure difference across the interface from the LDFT simulations is more complicated than the bubble situation because the pressure tensor is anisotropic. Indeed the transverse pressure within the liquid bridge varies in the z-direction. Therefore, the "bulk" pressure within the liquid bridge is assumed to be the average transverse pressure in the z-direction at the center of the bridge:

$$\bar{p}_L = \sum_{i,x=N_x}^{N_z} \bar{p}_T(z) / N_z. \tag{3.52}$$

For large separation distances where liquid bridges are stable, equation (3.52) tends toward the bulk pressure within the liquid as determined by equation (3.6). This

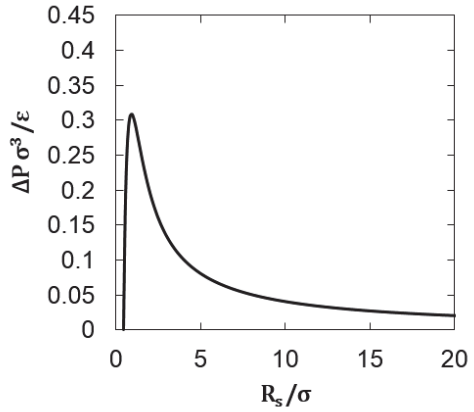

Figure 3.27 Absolute Laplace pressure as a function of the surface of tension (*i.e.*, the radius of curvature of the interface).

is to be expected because the wall interactions have less of an influence on the total free energy of the system. For small separation distances where the walls significantly impact the free energy of the system, the pressure within the liquid bridge deviates from the expected bulk result. However, it more accurately represents the pressure between the two plates and yields a better prediction of the curvature of the interface than the bulk assumption does. The bulk pressure in the vapor is obtained from equation (3.6), which yields the same result if it were determined using equation (3.52) at x = 1. The bulk pressure in the vapor is then subtracted from the pressure in the liquid bridge to yield the pressure difference across the interface (see Figure 3.28).

In short, the surface of tension of an interface has been predicted by inserting the extracted pressure difference from the LDFT simulations into equation (3.50) and then iteratively solving equations (3.50) and (3.51). From the two possible solutions, the surface of tension that best agrees with the system saturation is chosen.

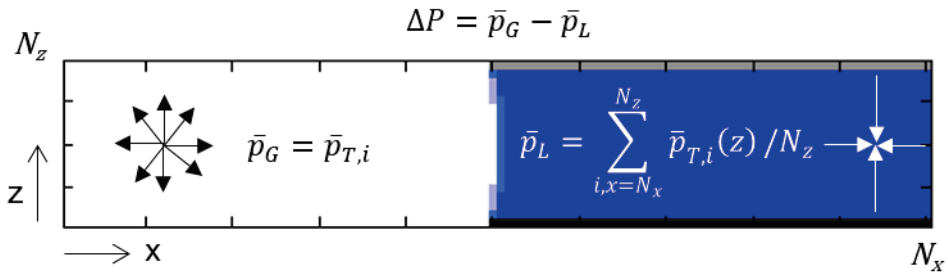

Figure 3.28 Isotropy and anisotropy of the transverse pressures $\bar{p}_T$ within the bulk vapor $\bar{p}_G$ and bulk liquid $\bar{p}_L$ regimes, respectively. The arrows represent the magnitude and direction of the pressures. The white arrows point inward to indicate that the liquid is in a state of tension or negative pressure. The bulk pressure in the vapor is equal to the transverse pressure at any point in the vapor. The bulk pressure in the liquid bridge is found by averaging the transverse pressure in the z-direction at the center of the bridge ($x = N_x$).

The effect of the RH, plate separation and the hydrophilicity of the walls on the curvature of a liquid bridge has been studied at 300 K. The RH is allowed to vary from 0.01 to 1 in 0.01 increments. Five plate separation distances (1, 5, 10, 15, and 20 lattice units) are considered and N_x is fixed at 100 lattice units. The relationship between the affinity of the vapor to the wall β_w and the contact angle ϕ has been calculated by the method described by Monson [134] (see Figure 3.22).The system has been initialized like the previous case by filling the left half with vapor ($\rho_i = 0$) and the right half with liquid ($\rho_i = 1$) to ensure that liquid-bridges form.

A representative liquid bridge is shown in Figure 3.29 for super-hydrophilic walls at RH = 0.88 and N_z = 20. The black circle represents the surface of tension and the yellow line represents the 0.5 density line. As can be seen, the surface of tension appropriately describes the radius of curvature of the liquid-vapor interface. This agreement between the LDFT simulations and the surface of tension estimation is the same for walls of varying hydrophilicity and separation distances, except for RH

levels near saturation where the interface tends toward the planar case or when the LDFT interface does not exhibit constant curvature.

For super-hydrophilic walls, the predicted surface of tension, interfacial surface tension, pressure differences, and capillary forces as a function of RH and wall separation distances are shown in Figure 3.30. The solid black line represents the Kelvin equation or the prediction achieved by assuming the Kelvin equation, the dashed black line is the planar surface tension limit or the zero line for the pressure difference, and the symbols represent the LDFT simulated results, where lighter gray symbols represent larger wall separation. The numbers indicate which plate separation distance corresponds to which set of simulated results.

In Figure 3.30a, the surface of tension for a wall separation distance of one lattice site corresponds to the situation of a monolayer of liquid between the walls. The close proximity of the surface allows the vapor to condense at very low RH levels (<0.2 RH) primarily due to the strong affinity of the adsorbing vapor to the walls. For this separation distance, the surface of tension as a function of RH has a

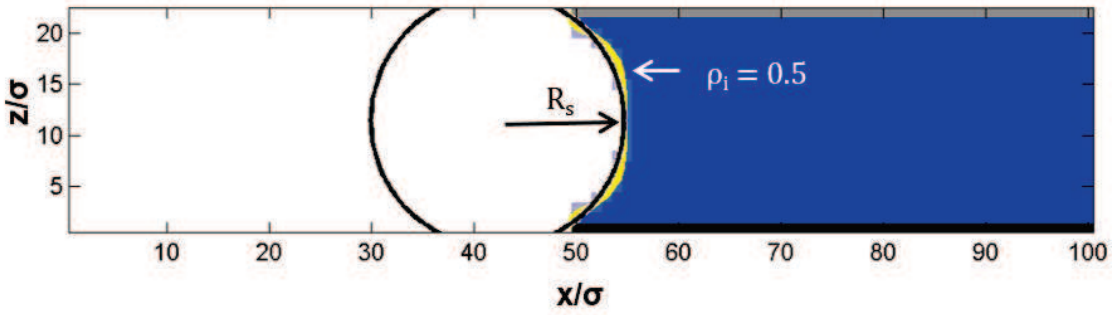

Figure 3.29 Curvature of a liquid bridge between super-hydrophilic walls at 300 K. RH = 0.88 and N_z = 20. The black circle represents the surface of tension and the yellow line represents the 0.5 density line. The deeper the blue the more dense the phase at the site. The black and gray lines indicate the parallel walls.

similar shape as the Kelvin equation, but the slope is greater. As the separation distance increases, the RH level at which a liquid bridge can form increases. This is expected because a higher saturation is required to fill a larger space and the walls have less influence on the overall behavior of the system. Hence, the presence of an external field (attraction of the plates) effectively changes the phase diagram of the condensed vapor between the two plates and the location of the spinodal and binodal are different for each separation distance. Therefore, the influence of super-hydrophilic walls may stabilize the formation of a liquid phase at levels beyond the spinodal limit (lower than 0.28 RH for 300K) for very small separations, thus causing capillary effects at low humidity levels. This is an important effect to consider while working with hydrophilic surfaces experimentally. Once the separation becomes so large that the effect of the plates is negligible, the phase diagram will behave as a two-phase, pure component system would without an external field. This is evidenced by the fact that the slope of the simulated results resemble the Kelvin equation more closely for larger separation distances.

As expected, the surface tension of a curved meniscus (Figure 3.30b) approaches zero as the RH approaches the limit of stability of liquid-bridge formation for small separation distances. However, at a separation distance of 5 lattice sites, the radius of curvature of the interface is always large enough to produce a meniscus with a surface tension equal to the planar limit. Therefore, for plate separation distances greater than 2 molecular diameters (see Figure 3.16), the surface tension can be considered constant.

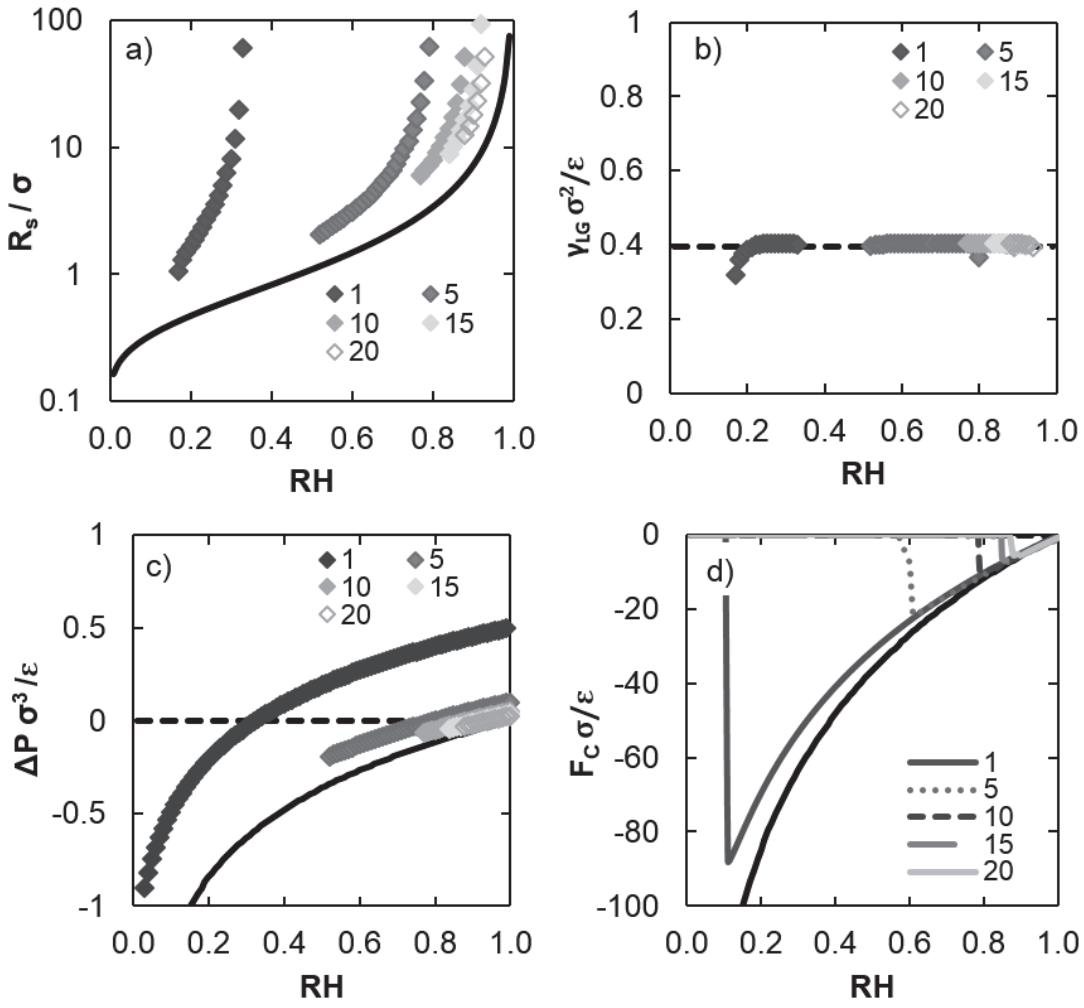

Figure 3.30 Properties of a liquid bridge between two super-hydrophilic ($\beta_w = 1.5$, $\phi = 0^o$) parallel plates at 300 K. Lighter gray symbols represent simulations at larger wall separation and the numbers indicate the plate separation distance h/σ. a) Surface of tension vs. RH. Black line represents the Kelvin equation. b) Surface tension vs. RH. Dotted black line is the planar surface tension. c) Laplace pressure vs. RH. Black line is the pressure difference obtained from the traditional Kelvin equation, dotted black line is the zero line. d) Capillary force as a function of RH. Black line represents the capillary force predicted from the traditional Kelvin equation.

In Figure 3.30c, the pressure differences from the LDFT simulation have also been compared with the Laplace pressures (solid black line) assuming that the Kelvin equation is applicable and the surface tension is constant. Initially, the LDFT pressure differences are negative, which is consistent with the formation of a liquid bridge. As the pressure difference approaches zero (dashed black line) with increasing RH, the surface of tension also expectedly approaches infinity or the planar limit (Figure 3.30a). The pressure differences also approach the continuum limit as the separation distance increases.

Note that the pressure differences associated for a separation distance of one lattice spacing yield liquid-bridge formation for RH levels around 0.02. However, the absolute value of the pressure difference is sometimes greater than 0.31, which has no solution to equations (3.50) and (3.51). Thus, there are no corresponding surfaces of tension or surface tensions for these RH levels. Indeed when the absolute value of the LDFT pressure difference is greater than 0.31, the configuration may represent an unphysical extrapolation of the model, since a monolayer of water between two strongly adhering plates is an extreme case of liquid bridge formation. At larger separation distances, the LDFT pressure difference is generally below 0.31, further suggesting that the abnormal LDFT pressures are a model artifact.

Likewise, positive pressure differences indicate that the liquid bridge is pushing into the bulk vapor. Therefore, in these situations, the system has changed configurations from a liquid-bridge arrangement to a droplet. Even though this configuration also exhibits curvature, it is not the system of interest in this study and its properties are not considered herein. The key point is that the interface becomes

planar as the pressure difference moves from negative to positive with increasing RH. The effect of positive Laplace pressures is also mitigated at higher separation distances, but not completely eliminated.

The capillary force between the walls is equal to the partial derivative of the excess energy with respect to a change in plate separation divided by the total surface area of the two plates:

$$\bar{F}_C = -\frac{1}{\bar{A}_s}\left(\frac{\partial \bar{\Omega}^{ex}}{\partial \bar{h}}\right)_{\mu,T,\bar{A}_s} \approx -\frac{1}{\bar{A}_s}\frac{\Delta \bar{\Omega}^{ex}}{\Delta \bar{h}} \tag{3.53}$$

The excess surface energy in this case is defined as the total energy of the system (from equation (3.45)) minus the energy of a system of the same volume filled with bulk vapor [45]:

$$\bar{\Omega}^{ex} = \bar{\Omega} - \bar{\Omega}^{b} = \bar{\Omega} + p_G V/\varepsilon \tag{3.54}$$

Once the excess energies are calculated for the system at $\bar{h}$ and $\bar{h} + 1$, the total force for a given RH level is calculated from equation (3.53).

The capillary force results are shown in Figure 3.30d where negative forces indicate an attractive force. The solid black line represents the continuum limit for the capillary force between two flat plates and is calculated directly from the Kelvin equation, a constant surface tension, and the Young-Laplace equation, and is multiplied by the surface area of the plates. This model unphysically predicts that the capillary force tends toward an infinite attraction as RH approaches zero, which is purely an effect of the Kelvin equation. The LDFT simulations more realistically indicate that eventually the capillary force tends to zero as the RH approaches zero,

though it passes through a maximum attraction (minimum force) at different RH levels depending on the separation distance of the plates. In general, the shape of the LDFT-generated force curves follows the continuum trend. It is important to know that this particular force curve is specific to liquid bridges between parallel plates. The trend does change with changes in the morphology of the plates [14].

Figures 3.31-3.37 show the results for liquid bridges between plates with contact angles varying from 0° to 90° in 15° increments. The lines and symbols represent the same information as that in Figure 3.30. Interestingly, the observed behavior in Figure 3.30 is typical for all contact angles. For example, the simulations associated with a separation distance of one always have the greatest deviation from the ideal case, since the system is governed primarily by the wall interactions and not the fluid-fluid interactions. In fact, the liquid-bridges at the closest separation distances actually do not appear for contact angles near 90° (Figures 3.36 and 3.37) because the walls are now sufficiently repulsive to the vapor that the close contact impedes the formation of a liquid bridge. As the separation distance increases, the LDFT predictions generally tend toward the continuum limit. This means that the surface tension for larger separation distances is usually equal to the planar surface tension. Finally, the capillary-force curves exhibit maximum attraction and tend toward zero as the RH approaches zero or RH approaches one.

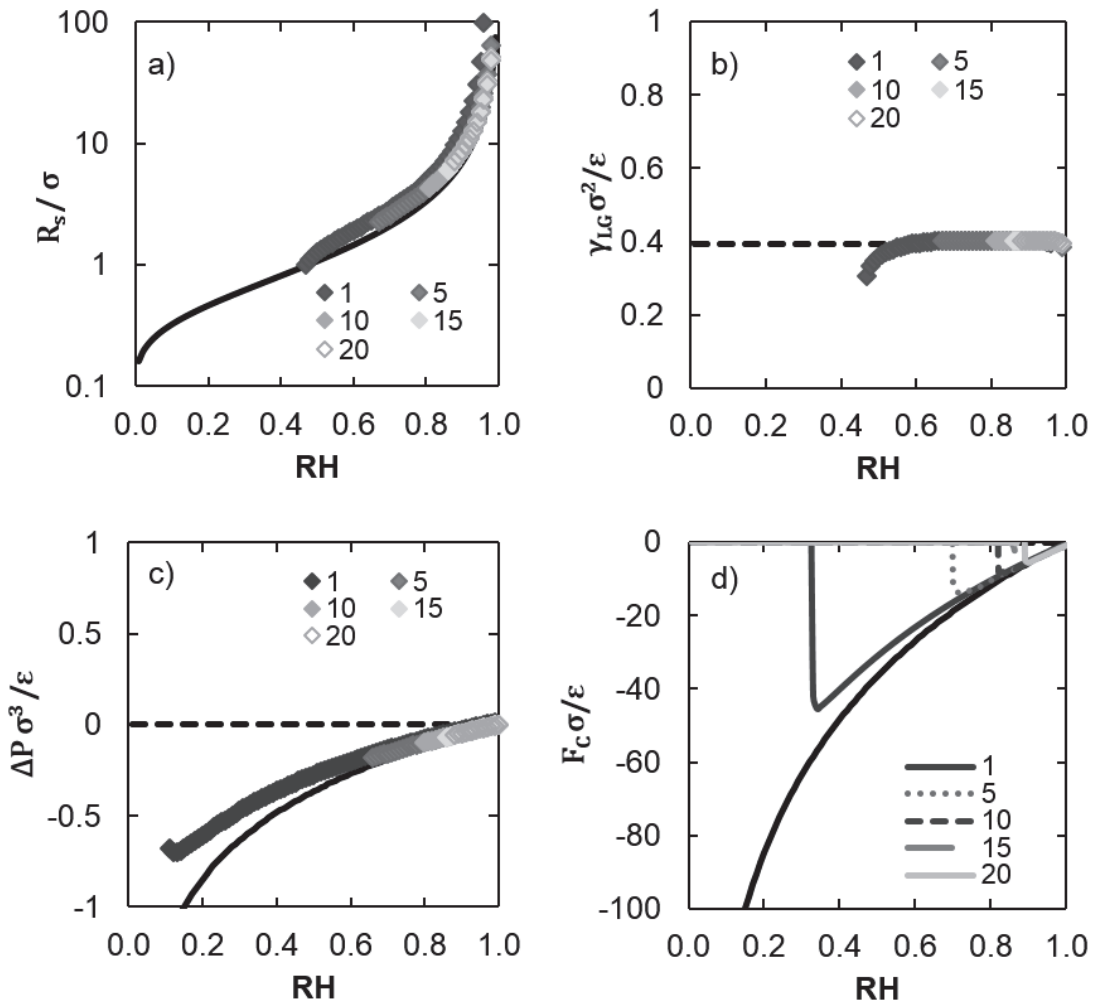

Figure 3.31 Properties of a liquid bridge between hydrophilic ($\beta_w = 1$, $\phi = 0^o$) parallel plates at 300 K. See Figure 3.30 for an explanation of lines and symbols

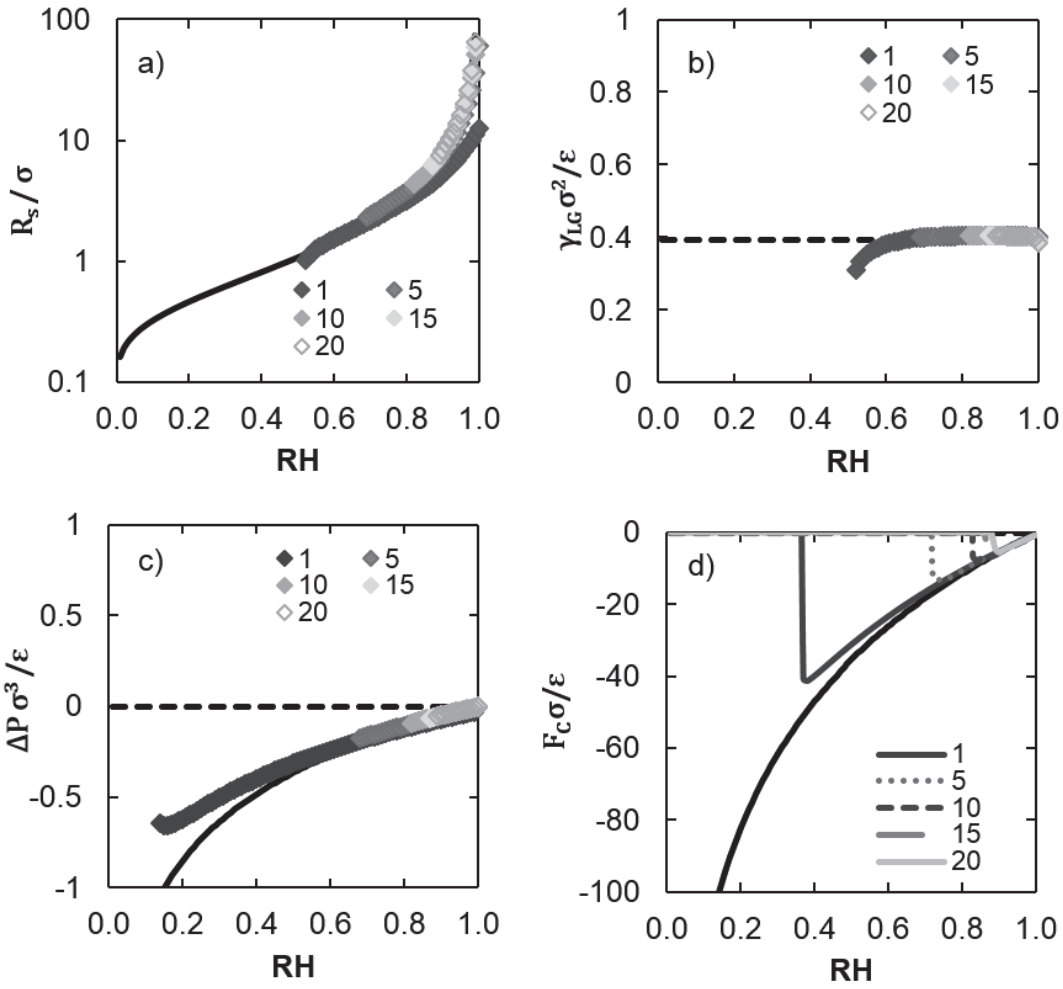

Figure 3.32 Properties of a liquid bridge between hydrophilic ($\beta_w = 0.95$, $\phi = 15^o$) parallel plates at 300 K. See Figure 3.30 for an explanation of lines and symbols.

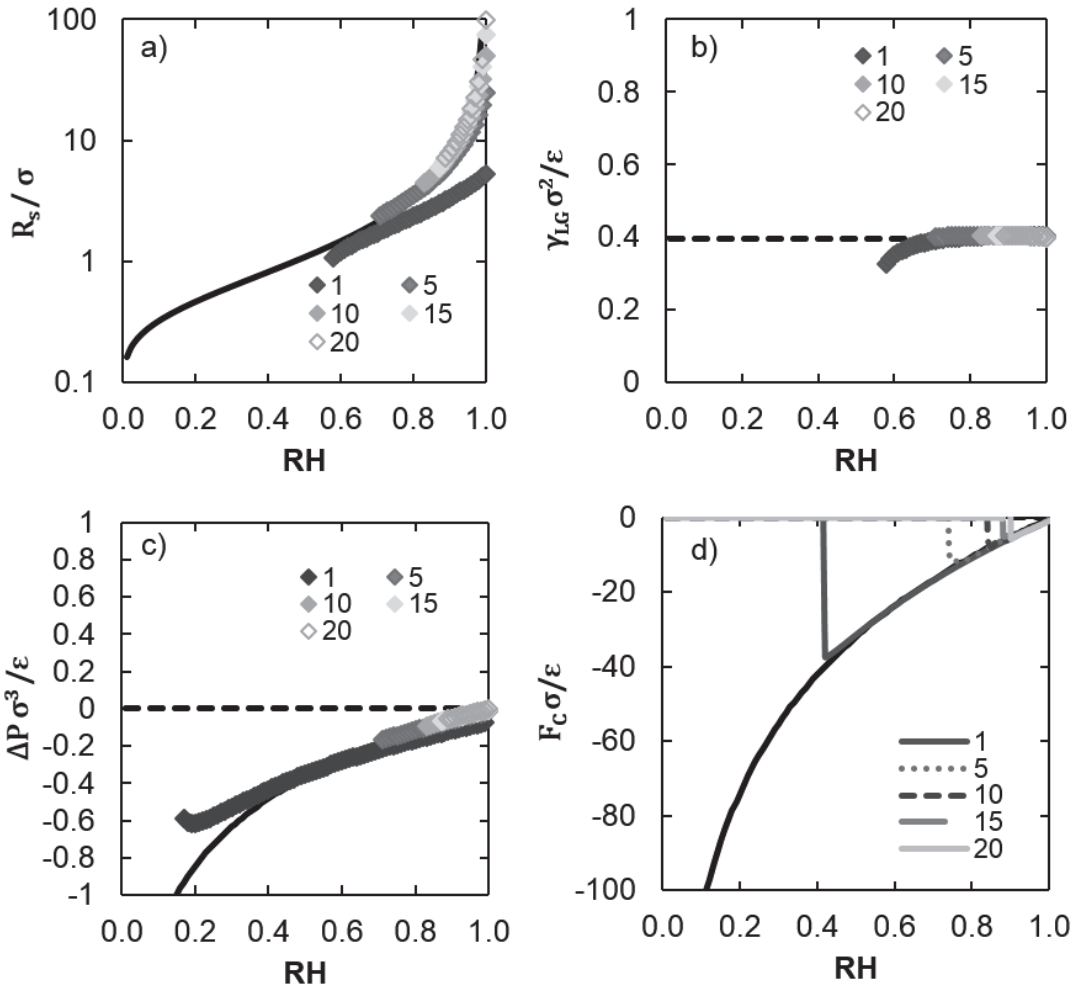

Figure 3.33 Properties of a liquid bridge between hydrophilic ($\beta_w = 0.9$, $\phi = 30^o$) parallel plates at 300 K. See Figure 3.30 for an explanation of lines and symbols.

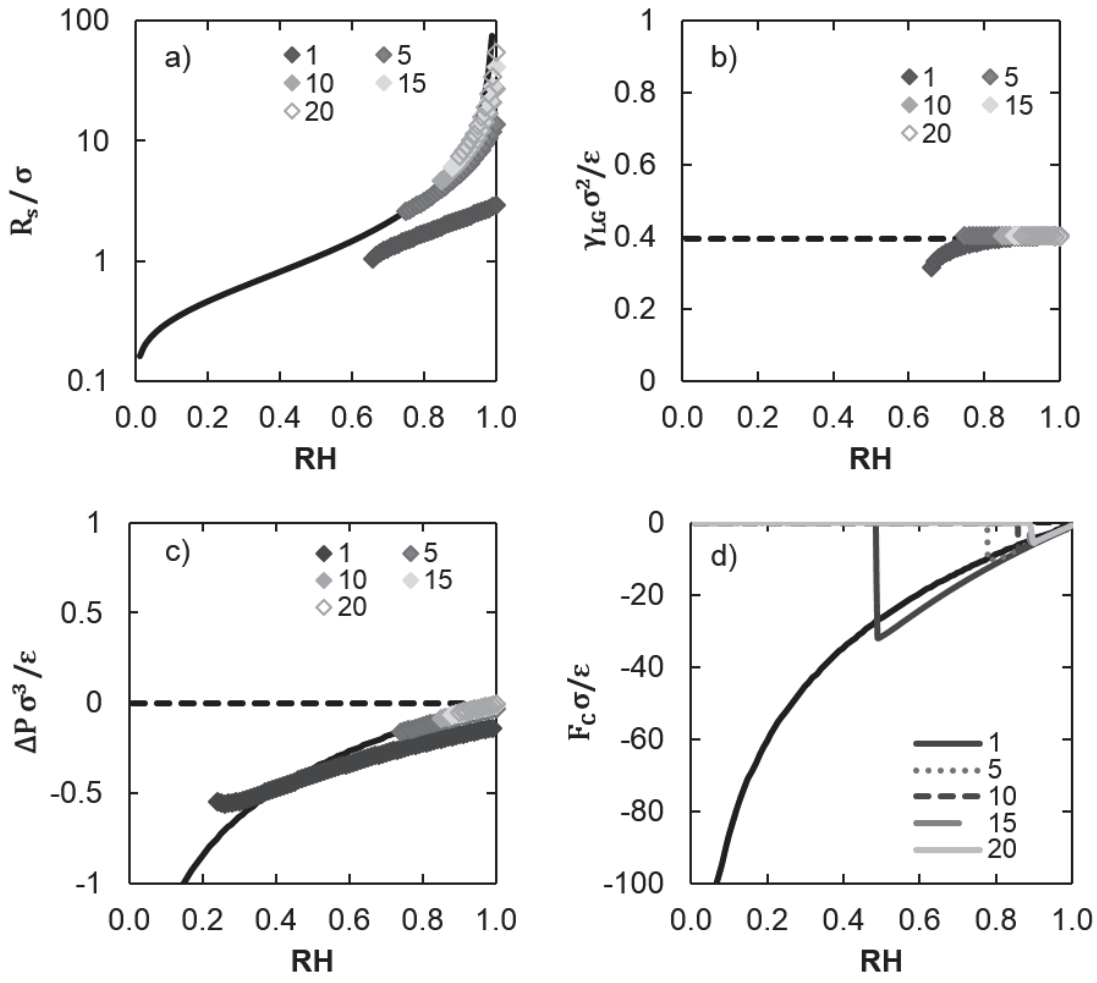

Figure 3.34 Properties of a liquid bridge between hydrophilic ($\beta_w = 0.83$, $\phi = 45^o$) parallel plates at 300 K. See Figure 3.30 for an explanation of lines and symbols.

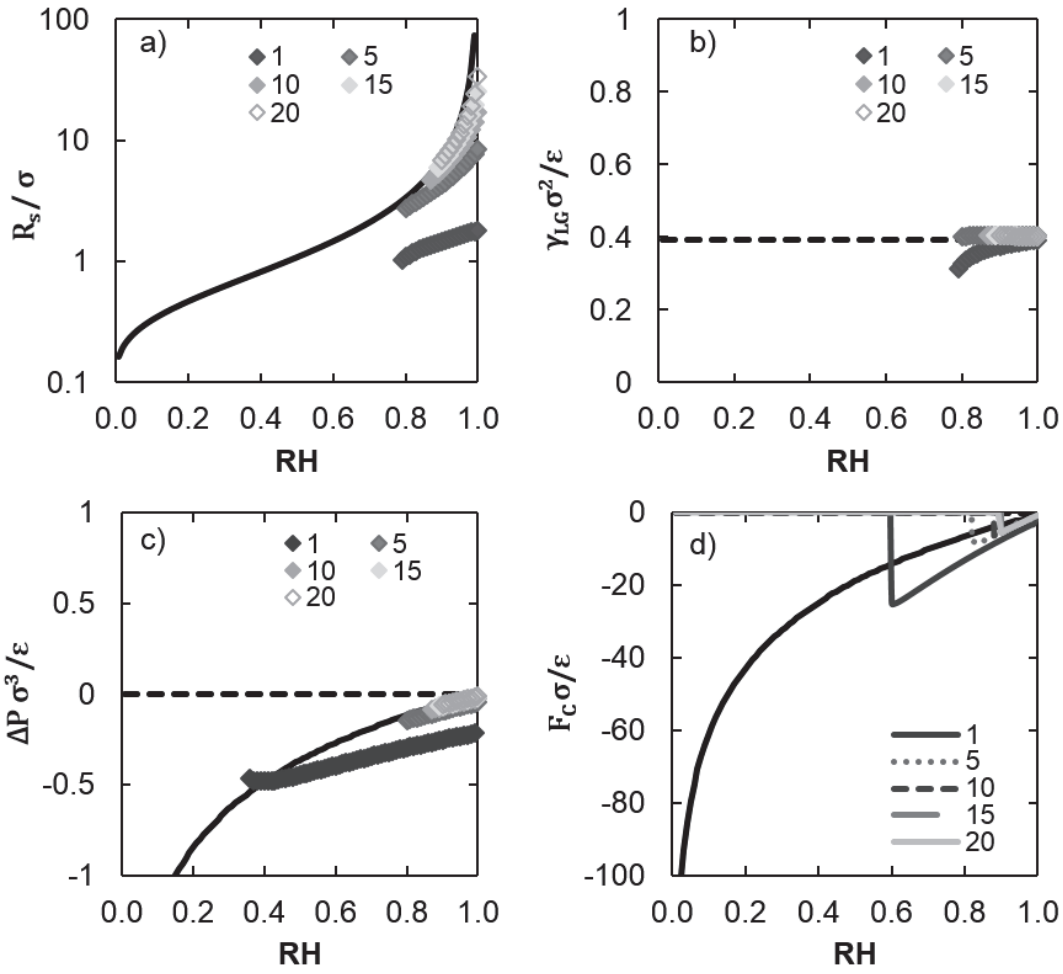

Figure 3.35 Properties of a liquid bridge between hydrophilic ($\beta_w = 0.73$, $\phi = 60^o$) parallel plates at 300 K. See Figure 3.30 for an explanation of lines and symbols.

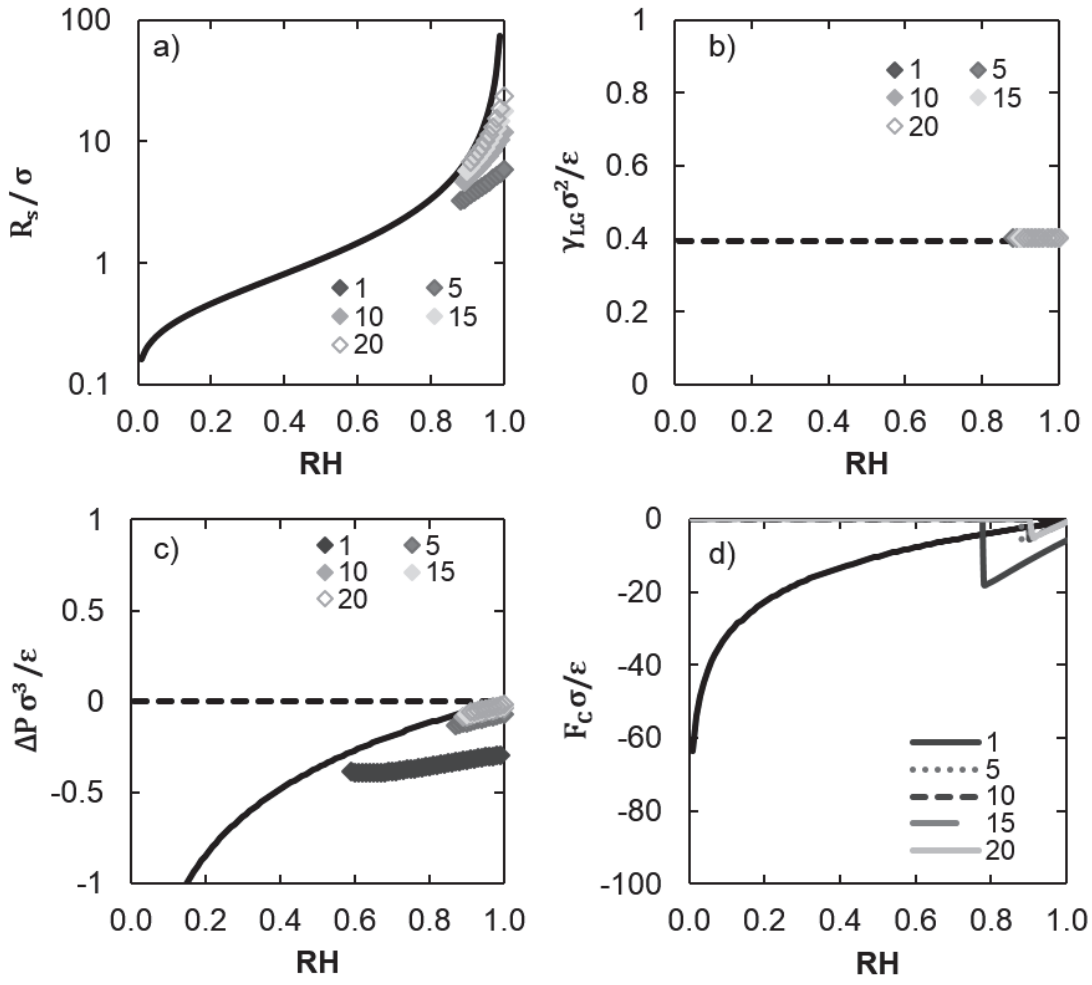

Figure 3.36 Properties of a liquid bridge between hydrophilic ($\beta_w = 0.62$, $\phi = 75^o$) parallel plates at 300 K. See Figure 3.30 for an explanation of lines and symbols.

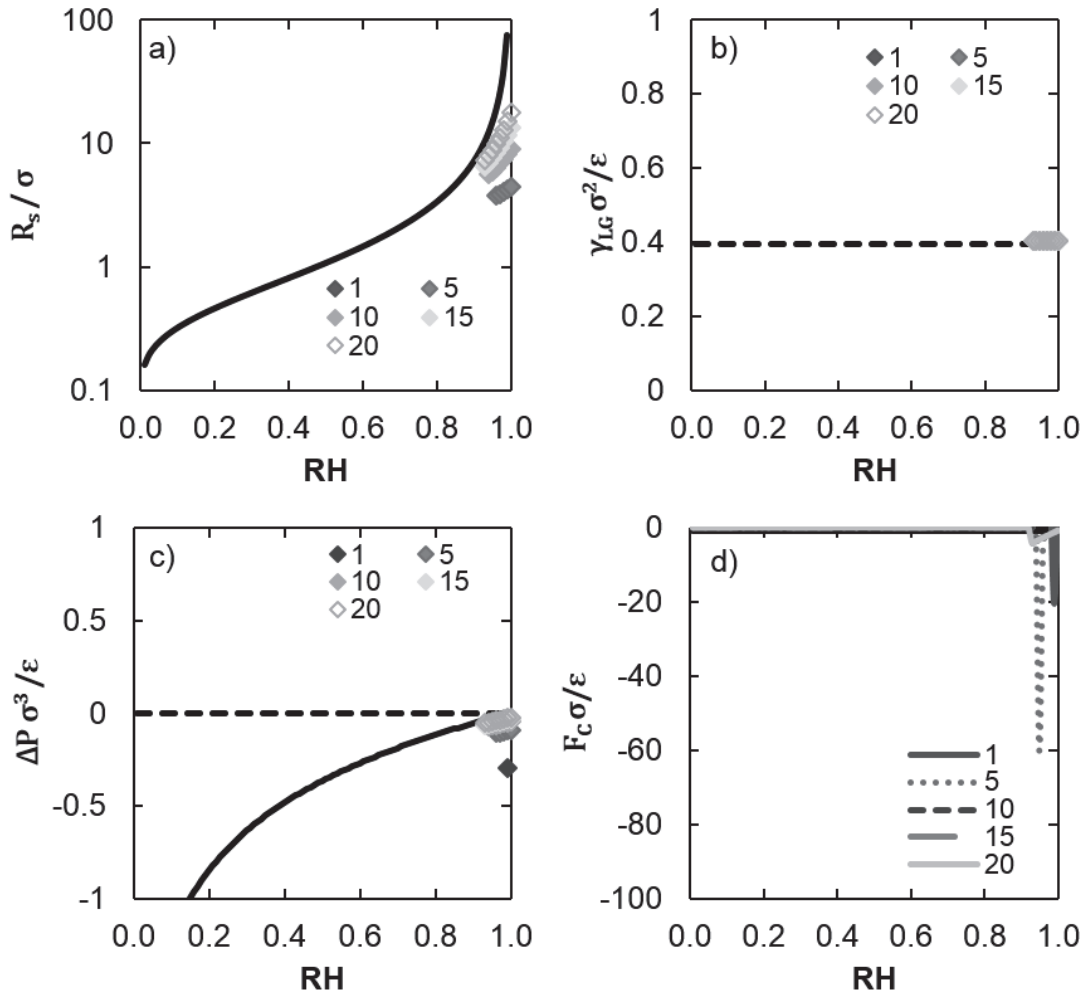

Figure 3.37 Properties of a liquid bridge between parallel plates ($\beta_w = 0.5$, $\phi = 90^o$) at 300 K. See Figure 3.30 for an explanation of lines and symbols.

As expected, an increase in the contact angle (decrease in wall hydrophilicity) increases the RH at which a liquid-bridge can form for a given separation distance. For example, in Figures 3.31a, 3.33a, and 3.35a, the liquid-bridge forms at RH levels of 0.66, 0.71 and 0.8, respectively, for a fixed separation distance of five lattice sites. Essentially, these results show that as the hydrophilicity of the walls decrease, a higher saturation is required to sustain a liquid bridge for a given separation distance. Hence with contact angles near 90°, only RH levels near saturation may produce liquid bridges.

Peculiarly, the LDFT simulations predict that for a contact angle of 90° a stable liquid bridge forms at a *lower* RH at a separation distance of ten, than the liquid bridge formation at a separation distance of five (Figure 3.37). Intuitively, one would expect that if a liquid bridge does not form at a separation distance of five for a given RH, it will not form for larger separation distances. However, it actually depends on the previous saturation of the system. To explain, the LDFT simulations are initialized in such a manner that the presence of a liquid bridge is automatically assumed. Essentially, this is equivalent to performing an experiment at complete saturation and then slightly decreasing the RH. At these high RH values, the system can form stable bridges resembling the planar case. Therefore, when the plates have a negligible effect on the overall free energy of the system, the system will converge onto a planar-like interface without regard to the wall separation. If the system is instead initialized with randomly dispersed vapor and liquid sites (*i.e.*, $0 \leq \rho_i \leq 1$) throughout the system, the liquid bridge converges only part of the time, suggesting that the liquid bridge is not the only possible configuration for that specific separation

distance and RH. Therefore, this unexpected result is actually a reflection of hysteresis, suggesting that the direction in which the simulations and experiments are performed is also important in characterizing capillary forces.

Overall, the Kelvin equation is a reasonable estimate of the surface of tension for liquid bridges between parallel walls, so long as the contact angle is close to zero and the plates are sufficiently separated (Figures 3.31a-3.32a). Yet, it does not predict the limit of stability for a given separation distance unless the dependence of the surface tension and liquid molar volume on the system curvature and saturation are properly considered. Because this information is not commonly known, a constant surface tension and liquid molar volume are often assumed in the Kelvin equation, which easily lends itself to unphysical extrapolations. This effect is exaggerated for super-hydrophilic or hydrophobic surfaces (Figures 3.30a and 3.37a). Therefore, analytical models assuming bulk properties within the Kelvin equation likely reflect unphysical results especially for low RH levels.

Figures 3.30-3.37 are succinctly summarized in Figure 3.38. Here the x-axis represents the RH, the y-axis is the contact angle of the walls, the z-axis is the separation distance between the walls and the color represents the surface of tension or radius of curvature of the interface. The difference here from Figures 3.30-3.37 is that the numerical values of the radius of curvature and its comparison to the Kelvin equation are not shown.

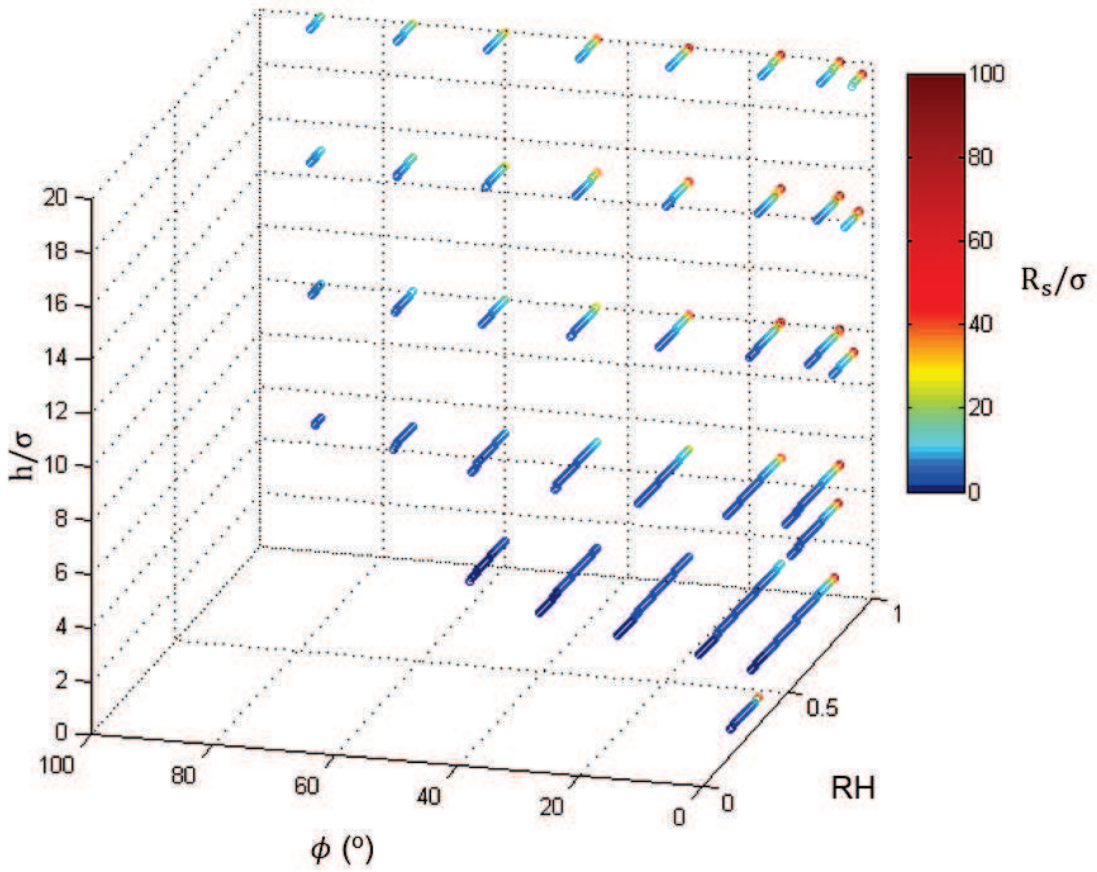

Figure 3.38 Surface of tension of liquid bridges between parallel walls as a function of RH, contact angle, and plate separation distance. The color represents the value of the surface of tension.

3.6.3 Comparison of Methods and Limitations of LDFT

A comparison between the two methods described in sections 3.6.1 and 3.6.2 to estimate the curvature of liquid-bridges between super-hydrophilic plates is shown in Figure 3.39. Generally, the results between the two methods are in reasonable agreement by generating similar values for the radius of curvature of the interface for a given RH and separation distance. Both methods also reveal that the presence of hydrophilic plates stabilize the system allowing liquid-bridge formation at very low RH levels. Moreover, both methods show that the simulated radii of curvature tend

toward the Kelvin equation as the separation distance increases, which means that the effect of the hydrophilicity of the plates becomes insignificant at large separation distances. The discrepancy between the methods is mostly due to the numerical instability of finding the minimum of the excess free energy. Improving the minimizing algorithm should bring both methods into better agreement at more RH levels.

Like any model, LDFT has its limitations. First, these simulations are performed on a lattice. This discretization is most useful for investigating the quantum nature of capillarity near the spinodal, where the consideration of individual molecules is important. However, mean-field density functional theory does not take into account any type of rotational, vibrational, or orientation effects within the molecular or inter-molecular structure. Therefore, it is expected that there are

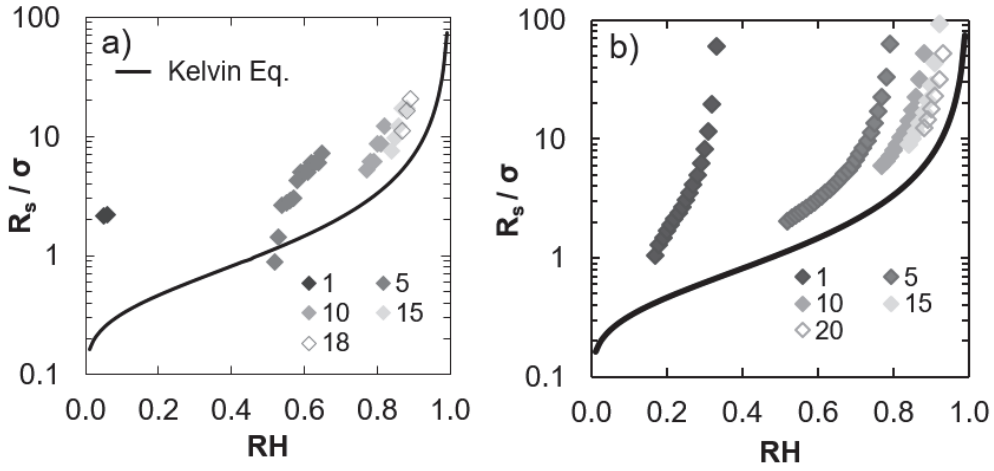

Figure 3.39 Comparison of the two methods to determine R_s as described in sections 3.6.1 and 3.6.2. a) Method of minimizing the excess free energy (3.6.1) b) Invoking the Young-Laplace equation (3.6.2). The numbers indicate the plate separation distance in lattice units. The black line is the Kelvin equation at 300 K.

limitations to the preceding results. Second, these simulations are specific to the parallel walls case and different geometries will likely yield different results. This simply adds another dimension of uncertainty in predicting the effect of system saturation on the strength of the capillary force. Certainly for a real system with non-ideal geometries and omnipresent surface roughness, the observed dependence of the radius of curvature of the interface on the system saturation will be highly irregular.

Yet, as has been demonstrated, the LDFT framework illustrates that assuming the traditional form of the Kelvin equation, or simply multiplying by the contact angle, does not accurately represent all of the possible effects of saturation on a system, though it can be considered a reasonable, first approximation.

3.7 Future Work

The LDFT work herein establishes the foundation necessary to investigate the effects of RH, separation distance, and hydrophilicity on the surface of tension of a liquid bridge. It can easily be extended to investigate the effects of temperature, surfaces with unequal contact angles, surface heterogeneity, and surface geometry on the surface of tension. Furthermore, this model has considerable utility in three dimensions, though care must be taken to appropriately describe the surface of tension of a catenoid.

More appropriately, LDFT is particularly suited to predicting the limit of stability of the liquid-vapor interface in either bubbles or liquid bridges. Therefore, the most useful extension of this study is to investigate the liquid molar volume as a function of the contact angle, separation distance, and saturation level. It is

anticipated that at the spinodal the liquid molar volume is at a maximum, or represents a highly compressed fluid beyond which there is not enough vapor to sustain the necessary Laplace pressure. If the limit of stability of the liquid molar volume can adequately be determined for given saturation levels, contact angles and separation distances, an analytical adjustment of the liquid molar volume can then be included in the Kelvin equation. This adjustment should then help to eliminate the non-physical extrapolations of the Kelvin equation in capillary force predictions.

Two very promising models that could benefit from a corrected Kelvin equation are that of Jaiswal *et. al.* [156] and You *et. al.* [52], [62], which utilize surface roughness and separation distances to determine the forces of adhesion within an order of magnitude of experimental measurements.

3.8 Conclusion

In summary, mean-field density functional theory on a lattice-gas framework has been utilized to describe bulk and two-phase behavior of a pure component system for planar interfaces, bubbles in metastable liquid, and liquid bridges between parallel plates. First the bulk vapor and liquid properties within the lattice-gas are established, which reveals that no stable liquid branch exists below RH of 0.28 at 300K. Next, the concepts of dividing surfaces, especially the surface of tension, are elucidated while investigating the surface tension of a planar interface. The properties of curved interfaces are then studied and show excellent agreement between the Kelvin equation and the LDFT simulations up to the spinodal limit. These simulations also reveal that the surface tension depends on the curvature of the interface for radii

of curvature equal less than or equal to two molecular diameters. A relationship between the radius of curvature of the interface and the surface tension has been used to predict the radii of curvature of liquid bridges between parallel walls at varying RH levels, separation distances, and contact angles. It has been found that the presence of the walls affects the phase behavior of the vapor and can cause it to deviate significantly from bulk behavior. Indeed using constant surfaces of tension and liquid molar volumes may yield significant non-physical extrapolations of the Kelvin equation. Once the proper limits of stability of the liquid bridges are established for a given set of parameters, appropriate pressure differences across the liquid-bridge interface and corresponding capillary forces may be calculated more accurately.

CHAPTER 4. HAMAKER CONSTANTS OF EXPLOSIVES

4.1 Introduction

The following chapter has been published in *Propellants, Explosives, Pyrotechnics* DOI: 10.1002/prep.201500021 [157].

A fundamental understanding of the adhesion between explosives residues, swabs used during detection of these residues, and surfaces to which the residues adhere is necessary to optimize the detection of these residues in airport security settings. The basic forces that control the behavior of the residues are the van der Waals (vdW) forces, which can be considered to be comprised of Keesom (dipole-dipole interactions), Debye (dipole-induced dipole interactions), and London dispersion forces (induced dipole-induced dipole interactions). The Hamaker constant A estimates the magnitude of vdW forces between two dissimilar materials or within a pure material [116]. Adhesive Hamaker constants between materials i and k in medium j are denoted as A_{ijk} while cohesive Hamaker constants for material i in a vacuum are denoted as A_{ii}. Using combining rules established by Israelachvili [116], families of A_{ii} can be used to estimate A_{ijk} among a variety of materials in varying media. As a result, A_{ii} of explosives residues allow prediction of A_{ijk}'s (and correspondingly the strength of adhesion) between these residues and commonly swabbed surfaces.

Methods of predicting A_{ii} using Hamaker's pair-wise additive approach [158] or the Lifshitz theory [3] are well-established [116], [159]. However, many materials, especially powders, do not have idealized, consistent geometries or adequate optical data to allow these approaches to be implemented in a straightforward manner. As has been noted first by Fowkes [160] and verified by van Oss [161] and Israelachvili [116], A_{ii} can be estimated via the surface tension γ of the material. Fowkes and van Oss assert that the surface tension (or surface energy for solids) can be split into a dispersive component γ^D and a polar component γ^P, which describe the London dispersion and all other interactions of the surface tension, respectively [161], [162]. In contrast, Israelachvili does not assume that γ has dispersive and polar components, but instead uses the total surface tension γ^T to predict A_{ii} [116]. This method works well for non-hydrogen bonding materials, since $\gamma^D \approx \gamma^T$, but it grossly exaggerates A_{ii} for materials which participate in hydrogen bonding interactions, like water [116]. This is not surprising because hydrogen bonding significantly contributes to γ^T but is not a vdW force. The A_{ii} discrepancy for polar molecules in Israelachvili's prediction method is eliminated when γ^D is used in place of γ^T, and it is hypothesized that γ^D may be used to approximate A_{ii} if γ^D can be appropriately determined.

For liquids, γ_L^D (subscript refers to the liquid state) is typically determined via the Owens and Wendt method [163] by measuring the contact angle of the liquid against a non-polar solid, usually polytetrafluoroethylene (PTFE) [164]. This of course assumes that PTFE only participates in dispersion interactions. For solid surfaces, γ_S^D is determined by measuring the contact angles of a family of alkanes or other non-polar

liquids against the surface of interest. γ_S^D for powders (and many explosives residues are powders), however, cannot be estimated via contact angle measurements unless the powder is compressed, which is potentially unsafe and/or can alter, through the deformation process, the surface energy of the material in question. Other methods for extracting γ_S^D without measuring the contact angles include the Washburn method via the Lucas-Washburn equation [165], and inverse gas chromatography (IGC) [164], [166]. Since it utilizes small amounts of material, operates in an inert atmosphere, and is a non-destructive technique, IGC has been used in this study to determine γ_S^D for safety reasons.

The only energetic materials that have been characterized to date via IGC are RDX (1,3,5-trinitroperhydro-1,3,5-triazine) [167], [168] and HMX (octahydro-1,3,5,7-tetranitro-1,3,5,7-tetrazocine) [167]. Unfortunately, the two studies investigating γ_S^D for RDX report conflicting results. At 298 K, Luo and Du's [168] extrapolated results predict γ_S^D = 23.0 mJ m^{-2} , whereas Teipel, Mikonsaari, and Torry [167] give an experimental γ_S^D = 41.8 mJ m^{-2}. Furthermore, Luo and Du state that the γ_S^D of RDX increases with increasing temperature, whereas Teipel, Mikonsaari, and Torry report that the γ_S^D of RDX decreases with increasing temperature. As has been observed with water [151], metals [169], and cellulosic fibers [170], γ generally decreases with increasing temperature. Therefore, that γ_S^D of RDX would increase is doubtful, especially since Luo and Du do not offer any explanation as to why RDX would exhibit this kind of unusual behavior. Other concerns with the Luo and Du paper include using only 3 homologous alkanes to predict γ_S^D, injecting air into the column to correct for dead time instead of

methane, and utilizing the highly disputed van Oss method [35], [36], [161], [171]–[174] for determining γ_S^p.

In this study, IGC has been used to characterize γ_S^D and subsequently the A_{ii} for not only RDX, but also for PETN (Pentaerythritol tetranitrate), TNT (trinitrotoluene), ammonium nitrate (AN) and AN-based explosives at 303 K. The AN-based explosives consist of a series of mixtures of AN with fuel oil (ANFO) and mixtures of AN with wax (ANWAX). The resulting value of γ_S^D for RDX is compared to both Teipel's and Luo's results and its implications are discussed. Additionally, the effect of the amount of fuel in the AN mixtures on γ_S^D is examined using simple linear regression. Finally, the IGC-predicted A_{ii}'s are compared to Lifshitz estimations for RDX, PETN, TNT, and AN.

4.2 Experimental Section

4.2.1 Materials

The alkane probes n-hexane, n-heptane, n-octane, n-nonane, and n-decane were purchased from Mallinckrodt and were used without further purification. K9 Non-Hazardous Explosives for Security Training and Testing (NESTT) training materials for RDX, PETN, and TNT were purchased from XM (www.xm-materials.com). These training materials comprised fused silica coated in RDX, PETN, or TNT, with a specific makeup of approximately 92 wt. % silica and 8 wt. % explosive. It was assumed (and later supported) in the IGC measurements that the silica particles were completely coated with the explosive material. The explosives-grade AN (Kinepak™) was obtained from Orica Mining. The paraffin was purchased from Sigma Aldrich, (Product # 76243, Lot #

1391695V) and the fuel oil (winter-grade diesel fuel) was purchased from a local gas station.

The AN paraffin (ANWAX) mixtures at 2, 5, and 10% paraffin by weight were prepared by melting paraffin at ca. 80 °C in a beaker and then stirring the corresponding weight of AN in by hand. Similarly, the AN fuel oil (ANFO) mixtures at 2, 5, and 10 % fuel oil by weight were prepared by adding fuel oil to a beaker and then mixing the AN in by hand. These mixtures were stored in a desiccator while not in use.

4.2.2 Apparatus

A commercial inverse gas chromatograph (Surface Measurement Systems, U.K.) was used for surface energy analysis. Approximately 500 mg of sample was packed in a silanized glass column using a standardized packing method. Samples were equilibrated with dry helium (10 mL/min) at 303 K for 4 hours prior to measurements. This treatment allowed for removal of any sorbed water or volatile impurities from the system. Methane was injected to correct for the retention time corresponding to the dead volume. Solvent probes were injected at infinite dilution conditions at 303 K and detected with a flame ionization detector. The procedure was repeated 3 times for each sample.

4.3 Theory

In IGC the dispersive surface tension of the probes γ_L^D is known for the n-alkane series (see Table 4.1), whereas the dispersive surface energy of the powder γ_S^D is not. To determine the value of γ_S^D, the net retention time t_n (i.e., the amount of time the probe

requires to exit the column minus the dead time), of each probe is recorded. t_n can then be related to net retention volume V_n by [175]

$$V_n = \frac{j_m}{m} F t_n \frac{T}{T_r} \tag{4.1}$$

where m is the sample (powder) mass, F is the exit flow rate of the probe, T is the column temperature, T_r is the reference termperature, and j_m is the James-Martin compressibility factor, which accounts for the pressure drop in the column [24]. Injecting the probes at infinite dilution condition allows for the assumption that probe-probe interactions are negligible and the retention is due solely to probe-substrate interactions. As a result, the probes can be treated as ideal gasses and the Gibbs energy of adsorption, ΔG^0, is related to V_n through

$$\Delta G^0 = RT \ln V_n + C \tag{4.2}$$

where R is the ideal gas constant and C is a constant dependent on the chosen reference state [176].

ΔG^0 can be approximated by multiplying the energy of adhesion per unit surface area, W_A, by the cross-sectional area of the probe molecule a and Avagadro's number N_A:

$$\Delta G^0 = a N_A W_A. \tag{4.3}$$

a has been estimated by Schultz, Lavielle, and Martin [176] by injecting the probes on dispersive solids. Assuming that there are only dispersive interactions between the probe and the powder, equation (4.3) can be expressed as

$$\Delta G^0 \approx \Delta G^D = aN_A(W_A^D). \quad (4.4)$$

According to Fowkes [162], [177], W_A^D is related to the surface energies of the interacting media through

$$W_A^D = 2\sqrt{\gamma_L^D \gamma_S^D}. \quad (4.5)$$

Combining equations (4.2), (4.4) and (4.5), V_n is finally related to the components of the solid surface energy:

$$RT \ln V_n = 2aN_A\left(\sqrt{\gamma_L^D \gamma_S^D}\right) + C. \quad (4.6)$$

By determining the slope of $RT \ln V_n /(2N_A)$ versus $a\sqrt{\gamma_L^D}$ for a homologous series of hydrocarbon probes, γ_S^D becomes

$$\gamma_S^D = (slope)^2. \quad (4.7)$$

Table 4.1 shows values of a and γ_L^D for multiple homologous hydrocarbon probes, as listed in [176].

Table 4.1 γ_L^D and a at 20 °C for the alkane probes obtained from [176].

	γ_L^D	a
Probe	**mJ m^{-2}**	**(nm^2)**
n-Hexane	18.4	0.515
n-Heptane	20.3	0.570
n-Octane	21.3	0.630
n-Nonane	22.7	0.690
n-Decane	23.4[i]	0.750[ii]

i. [166]
ii. Extrapolated from the n-hexane – n-nonane values

Though this analysis is widely applied in IGC measurements, it must be noted that there are significant concerns associated with its use. First, the assumption that γ can be split into a dispersive component and other components and that these components are additive may not be valid [178], [179]. Secondly, Fowkes' theory including polar contributions to γ is thermodynamically inconsistent, in that it has three degrees of freedom, whereas it should only have two [178]. This inconsistency can be eliminated when a dispersive-only liquid interacts with a dispersive-only solid [178]. Additionally, only the dispersion interactions of the vdW forces can be reasonably predicted using a geometric mean [160], [179]. When Keesom and Debye interactions substantially contribute to the vdW force, the use of the geometric mean is questionable [179], [180]. If hydrogen bonding effects are not eliminated in the measurement of γ_S^D these effects can introduce significant error into the Hamaker constant prediction [116], [180]. Finally, IGC is extremely sensitive to the a parameter. Changing this value by 20% can change the resulting γ_S^D by 56% [166].

In an effort to utilize the theory while mitigating its potential shortcomings, only nonpolar probes were used in the analyses. This allows for the assumption that the energetic powders only have dispersive interactions with the probes. In addition, this substantiates the use of the geometric mean in equation (4.5), avoids the thermodynamic inconsistency, and significantly reduces any hydrogen bond contributions to the vdW force. Finally, by using probes with well-established values of a, we can avoid artificially extreme γ_S^D values.

With this approach and assuming that the London dispersion forces dominate the vdW force, A_{ii} can then be reasonably predicted using γ_S^D [160]:

$$A_{ii} = 24\pi\gamma_S^D D_0^2 \tag{4.8}$$

where the minimum separation distance between surfaces, D_0, is approximately 0.165 nm [116]. In this case, equation (4.8) becomes

$$A_{ii} \approx 2.1 \times 10^{-21}\gamma_S^D \tag{4.9}$$

where γ_S^D is in units of mJ m^{-2}.

For comparison, A_{ii} of each explosive compound has also been estimated with the Lifshitz model for the symmetric case of identical phases i in air

$$A_{ii} = \frac{3}{4}kT\left(\frac{\varepsilon_i - 1}{\varepsilon_i + 1}\right)^2 + \frac{3h\nu_e}{16\sqrt{2}}\frac{(n_i^2 - 1)^2}{(n_i^2 + 1)^{1.5}} \tag{4.10}$$

where k is Boltzmann's constant, ε_i is the dielectric constant, n_i is the refractive index in the visible range (at wavelength i), h is Planck's constant and ν_e is the main electronic absorption frequency (assumed to be 3×10^{15} s^{-1}), as reported by Israelachvili [116]. The estimated A_{ii} based on Lifshitz theory are listed in Table 4.2.

4.4 Results and Discussion

The average γ_S^D and A_{ii} as obtained from IGC for RDX, PETN, TNT, AN, ANFO, and ANWAX are reported in Table 4.3, where the ± indicates the 95% confidence interval around the mean. The γ_S^D value for RDX at 303 K in this study agrees with Teipel, Mikonsaari, and Torry [167] who reported γ_S^D = 41.8 mJ m^{-2} for RDX at 298 K. This agreement suggests that the silica in the NESTT materials did not significantly

Table 4.2 Refractive indices n_{589}, dielectric constants ε, and Lifshitz-derived A_{ii} for RDX, PETN, TNT and AN. The error around A_{ii} is ± 20% as suggested by [116].

Explosive	Lifshitz Theory		
	n_{589}	ε^{v}	A_{ii} (J x 10^{21})
RDX	1.59[i]	3.14	94 ± 20
PETN	1.55[ii]	2.72	83 ± 17
TNT	1.54[iii]	2.70	82 ± 17
AN	1.61[iv]	7.10	100 ± 16

i. [181] ii. [182] iii. [183] iv. [184] v. [185]

interact with the alkane probes and justifies the use of the NESTT materials for energetic material characterization via IGC. The result is not in agreement with the results obtained by Luo and Du [168], who predict γ_S^D = 24.3 mJ m^{-2} at 303 K and γ_S^D = 41.8 mJ m^{-2} at 371 K. This illustrates the discrepancies that can arise in the prediction of Hamaker constants using the IGC method, especially when there are variations in the experimental conditions that are the basis for the calculations.

As shown in Figure 4.1, the percentage of fuel oil in the AN does not significantly change the value of γ_S^D as indicated by the overlapping confidence intervals between 0%, 5%, and 10% fuel oil. Even though 2% fuel oil in AN appears to be signficant, a simple linear regression analysis among all levels of fuel oil reveals that the slope is not statistically distinguishable from 0 (p-value = 0.43). This suggests that γ_S^D for ANFO mixtures is not different than pure AN. A similar conclusion can be made with the 0%, 2%, and 5% ANWAX mixtures for the same reasons (p-value = 0.49). However, there is a significant difference from pure AN and ANWAX 10% (p-value = 0.0020), which is likely caused by the liquid paraffin partially coating the AN prills and then hardening.

Table 4.3 The dispersive surface energy γ_S^D and Hamaker Constants A_{ii} of RDX, PETN, TNT and AN-based explosives obtained via experimental IGC measurements. The error indicates the 95% confidence interval around the mean.

Explosive	γ_S^D **(mJ m^{-2})**	A_{ii} **(J x 10^{-21})**
RDX	41.8 ± 0.6	87.9 ± 0.9
PETN	34.6 ± 1.3	72.7 ± 1.9
TNT	34.8 ± 4.1	73.2 ± 5.9
AN	39.6 ± 0.7	83.2 ± 1.1
ANFO 2%	41.5 ± 0.8	87.0 ± 1.2
ANFO 5%	40.1 ± 0.0	84.1 ± 0.1
ANFO 10%	39.8 ± 0.5	83.5 ± 0.7
ANWAX 2%	36.6 ± 1.5	76.9 ± 2.1
ANWAX 5%	38.4 ± 2.8	80.6 ± 4.1
ANWAX 10%	46.4 ± 0.9	97.4 ± 1.4

Solid paraffin has a $\gamma_S^D \approx 68$ mJ m^{-2} [186], so a partial coating of paraffin around the prills would likely increase the γ_S^D of pure AN. This influence is not observed for 2% and 5% ANWAX mixtures because there is not enough paraffin to coat the prills in any appreciable manner. Therefore, it appears that for ANWAX mixtures around 10%, the γ_S^D is a function of the percentage of paraffin in AN. However, this dependence may not be practically significant because the majority of AN-based explosives are optimized at less than 10% fuel. Therefore, it is reasonable to assume that γ_S^D for ANFO or ANWAX is approximately equal to the γ_S^D for pure AN, unless the paraffin content is close to or greater than 10%.

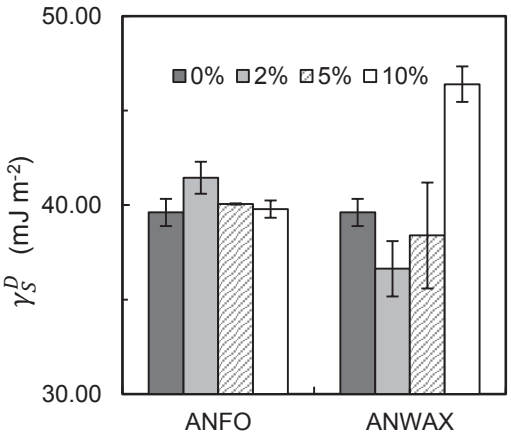

Figure 4.1 The dispersive surface energies γ_S^D of ANFO and ANWAX as a function of the wt. % of fuel in AN. The error bars indicate a 95% confidence interval around the mean.

These results suggest that the addition of fuel oil or paraffin (up to 10%) in AN does not significantly change the cohesive dispersive forces within the composite material, at least near the surface of the prill. It should be noted that this does not necessarily mean that the adhesion of ANFO or ANWAX to a substrate will be the same as the adhesion of AN. This is because (1) the prill's surface topography is extremely variable among AN, ANFO, or ANWAX and (2) the prill's susceptibility to deformation can increase with an increasing amount of fuel. Both the surface topography and the amount of deformation determine the closeness of approach of interacting surfaces and can cause changes in adhesion even if the A_{ii} does not change. The fact that the γ_S^D does not change for different compositions of fuel merely suggests that the A_{ii} of AN may be used in addition to other variables such as surface topography and deformation to predict the overall adhesion between substrates and AN-based explosives.

It should be noted, that the results in Figure 4.1 are specific to explosives-grade AN, which is highly porous and can absorb more fuel oil than less-porous, fertilizer-grade AN. It is likely that γ_S^D for fertilizer-grade AN will significantly depend on the weight percentage of fuel oil due to its lower porosity, but the effects of the grade and method of preparation of AN on γ_S^D have not been considered in this study.

In Figure 4.2, the IGC-predicted A_{ii} of RDX, PETN, TNT, AN and the AN-based explosives in Table 4.3 have been compared against the Lifshitz estimations listed in Table 4.2. Note that the Lifshitz calculations are approximate because much of the required data are not available in the literature. Indeed for ANFO and ANWAX, there are no optical data available. Values for refractive indices and dielectric constants have been taken from a variety of sources (see footnotes to Table 4.2) and v_e has been assumed to be 3×10^{15} s^{-1}. As a result, the error bars around the Lifshitz A_{ii}'s are ± 20% [116]. Where the IGC and Lifshitz results were able to be compared, the agreement between them was very good, within the error associated with the calculations.

In all cases, the IGC technique under-predicts the Lifshitz theory for the energetic powders. The likely explanation for the discrepancy is that the analysis assumes that there are no Keesom and Debye contributions to the overall vdW forces, and this assumption is not strictly valid for any of the explosives investigated. The presence nitro groups in RDX, HMX, PETN and TNT confers permanent local dipoles in each of their molecular structures. Moreover, the contribution of Keesom and Debye forces is even stronger for an ionic compound like AN. This explains why the IGC under-prediction is present for all the explosives but is the largest for AN in Figure 4.2. The IGC-predicted A_{ii}'s for

energetic powders represent the lower limit of the vdW interactions within the material, though the agreement will improve for less ionic energetic powders like RDX.

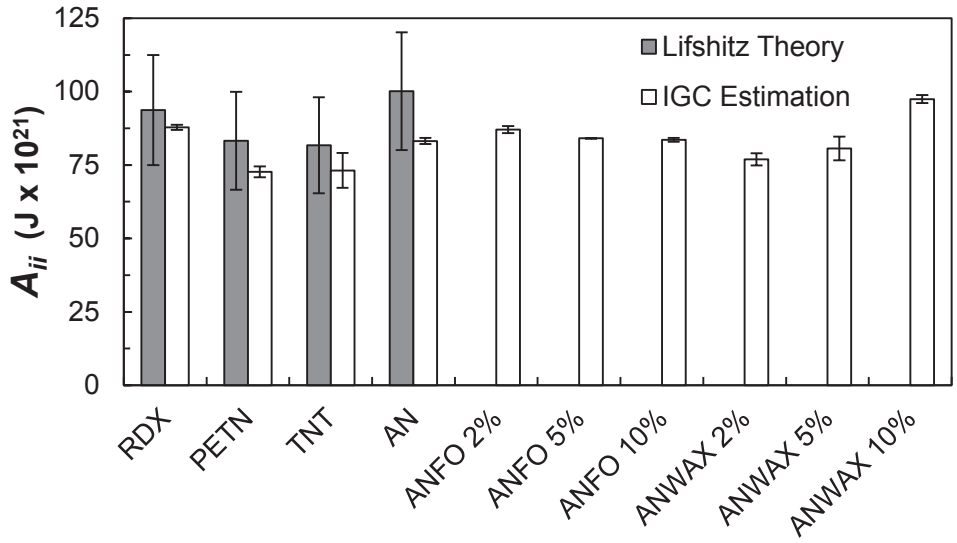

Figure 4.2 Comparison of IGC-predicted A_{ii} to Lifshitz theory estimations for RDX, PETN, TNT, AN and AN-based explosives. The error bars on the Lifshitz estimations are ± 20%, whereas the error bars on the IGC estimations indicate a 95% confidence interval around the mean. The optical data required for the Lifshitz theory were not available for ANFO or ANWAX

4.5 Conclusion

In summary, the γ_S^D and A_{ii} of RDX, PETN, TNT, AN, ANFO and ANWAX at 2, 5 and 10% fuel oil or paraffin, respectively, have been determined via IGC measurements using linear alkane probes. The γ_S^D for RDX at 303 K is in good agreement with the 298 K value from [167] and the predicted Lifshitz A_{ii} from published optical data, but disagrees with the results of [168]. Based on the experimental discrepancies in [168] and

other known thermodynamic trends, the conclusions in [168] appear to be unsubstantiated.

Additionally, it has been determined that γ_S^D for ANFO at 2, 5 and 10 % fuel oil and ANWAX at 2 and 5% paraffin is statistically indistinguishable from γ_S^D of pure AN. Therefore, γ_S^D for AN can be used to approximate γ_S^D and A_{ii} for ANFO and ANWAX, at least below 10% paraffin or fuel oil content. Finally, the IGC-predicted A_{ii}'s, though consistently lower, are within the projected error of the Lifshitz predictions, and can be used to determine the force of adhesion between explosives residues and common surfaces to improve contact sampling technologies in airport security settings.

CHAPTER 5. AFM-IR SPECTROSCOPY OF NANOCRYSTALS

5.1 Introduction

The following chapter has been published in *Analytical Chemistry* 2013 85(23) pp. 11449-11455, DOI: 10.1021/ac4025889 [187].

Drug-polymer composites, such as the coatings of drug-eluting stents [188] and nanoparticulate formulations [189], [190], are of widespread interest because the drug's release kinetics and bioavailability are controlled through proper polymeric selection and composite microstructure. To effectively engineer drug delivery systems, a fundamental understanding of drug structure and distribution in the dosage form is required [191]–[194]. This understanding necessitates methods to unambiguously chemically characterize drug formulations on the micro- and nanoscales.

Fourier transform infrared (FTIR) spectroscopy provides a wealth of chemical and structural information and is frequently used to characterize drug-polymer composites [191], [195]. However, nanoscale phenomena cannot be discerned with conventional FTIR spectroscopy because the spatial resolution is restricted to 3–30 μm by the optical diffraction limit [196]–[199]. In contrast, assumptions concerning the nanoscopic makeup of a system can be deduced from topographical and phase contrast analysis of solids obtained via atomic force microscopy (AFM), but this technique cannot describe

compositional effects directly. Recent innovations have overcome these limitations by combining the two techniques.

In infrared scattering Scanning Near-field Optical Micrscopy (sSNOM), a purely optical technique, an infrared light source is focused onto the apex of a cantilever tip. The tip apex acts as a point source near the substrate which circumvents the optical diffraction limit since the AFM tip is within nanometers of the surface. This technique has effectively imaged polymer/polymer blends [200], polymer/inorganic patterns [201], [202], and nanoparticles embedded in biological materials [203] with a spatial resolution of up to 20 nm [201], [202]. However, the optical signal for the infrared sSNOM technique is approximately six times weaker than that of infrared spectroscopy based on the absorptivity of the sample.

Contrastingly, photothermal induced resonance (PTIR) exploits the increased signal caused by infrared absorption. It allows for spatial resolution of chemical information on the nanoscale [199], [204]–[207], and has successfully assessed compositional variations in polymer blends [195], [208]–[215] and living cells [204]–[206], [216], [217]. As a result, PTIR has been used to analyze the drug-polymer blends in this study.

In PTIR spectroscopy, a sample is deposited onto a mid-infrared transparent ZnSe prism which is then irradiated by electromagnetic energy of defined wavelengths. When the wavelength of the incident radiation corresponds to one of the sample's absorption bands, the sample absorbs energy and converts it into heat. The resulting thermal stress induces a mechanical expansion in the sample. An AFM cantilever in contact with the sample will deflect as a result of this expansion. An optical parametric oscillator (OPO)

nanosecond laser creates fast thermal expansions, or pulses, in the material. These can cause an AFM cantilever in contact mode to oscillate. By recording the cantilever deflection as a function of time and taking the Fourier-transform of this signal, the cantilever's harmonic modes are determined. A local, composition-specific infrared spectrum may be obtained by examining the maximum amplitude of the cantilever's vibration modes as a function of the wavelength of the incident energy [207]. These spectra can be highly sensitive and quantitative when evaluated at the harmonic modes of the cantilever. At the same time, the cantilever acts like a spring-damper system where the tip resonant frequency changes with variations in surface stiffness. By tracking the contact resonant frequency as a function of position on a sample, one may simultaneously obtain high-resolution stiffness maps of heterogeneous samples [199].

The goal of this work is to evaluate the use of PTIR spectroscopy to allow chemical and mechanical evaluation of organic drug particles with diameters ca. 100 nm embedded within solid matrices, thereby extending prior efforts with this technique into the characterization of drug formulations. To this end, griseofulvin (GF) particles embedded in hydroxypropyl methyl cellulose (HPMC) have been characterized with a lateral resolution up to the smallest particle measured (90 nm), which is below the diffraction limit at infrared wavelengths. Additionally, particle size distributions via dynamic light scattering (DLS) and PTIR image analysis are shown to be similar, suggesting that the PTIR measurements are not significantly affected by inhomogeneous infrared absorptivity of the system. Finally, PTIR spectra well above the noise threshold from 3600 to 1000 cm^{-1} for 100, 350, and 800 nm GF particles have been obtained.

5.2 Methods

5.2.1 Materials

All chemicals were used as obtained without further purification. Griseofulvin (GF), a poorly water-soluble drug (EP/BP grade, solubility in water: 8.9 mg/l) was purchased from Letco Medical (Decatur, AL). Hypromellose, a.k.a., hydroxypropyl methyl cellulose (HPMC), was used as neutral polymeric stabilizer in suspension preparation and film/matrix former during spin-casting. Two grades of HPMC with identical chemistry but with slightly different viscosity, Methocel E15LV and E3, were purchased from Dow Chemical (Midland, MI). Sodium dodecyl sulfate (SDS) purchased from Sigma-Aldrich Co. (St. Louis, MO) was used as a wetting agent and for its known synergistic stabilizing action with cellulosic polymers in drug suspensions [189], [190], [218]. All solutions were prepared in Milli-Q® ultrapure water (Millipore Corporation, Billerica, MA).

5.2.2 Suspension Preparation.

Two aqueous suspensions of GF nanoparticles in HPMC/SDS were prepared via wet stirred media milling (WSMM) process to determine the potential of the PTIR technique for extracting chemical information on crystalline nanoparticles embedded in a polymer matrix. Sample 1 suspension with 10% GF, 2.5% HPMC E15LV, and 0.5% (w/w) (SDS) was prepared using a standard WSMM process, as described in [189]. To the best knowledge of the authors, drug particles with a median size below 100 nm have not been prepared using the WSMM process before. Sample 2 suspension was prepared

using a novel, intensified WSMM process that utilizes 100 μm wear-resistant, yttrium-stabilized zirconia milling beads (Saint Gobain, Mountainside, NJ), synergistic stabilizing action of HPMC/SDS combination, and the low-viscosity HPMC grade. To this end, sample 2 suspension with 10% GF, 2.5% HPMC E3, and 0.2% (w/w) SDS was milled for 6 h.

5.2.3 Sample Preparation.

The suspensions were stirred at 300 rpm for 30 minutes. The d_{50} were characterized by DLS (Zetasizer Nano-zs, Malvern) after diluting the suspensions with purified water (1:19 (v/v) for sample 1 and 1:30 (v/v) for sample 2). The d_{50} of sample 1 was 335.7 nm and for sample 2 was 85 nm. Next, 0.5 mL of sample 1 was added to an aqueous solution (4 mL) containing 2.5 % HPMC E15LV and 0.5% SDS by weight resulting in a 1:8 dilution (v/v). This solution was then spin-cast using a custom-made holder onto a ZnSe prism at 33.3 Hz (2000 rpm) for 20 s leaving a thin film of GF nanoparticles in HPMC. Similarly, 0.05 mL of sample 2 was added to 2 mL of the same aqueous solution as sample 1, resulting in a 1:40 dilution (v/v) and spin cast onto the prism at 33.3 Hz for 20 s. Film thickness was estimated by comparing the vertical displacement of the tip when moving from the coated to the uncoated regions on the substrate. As a result, sample 1 was ~500 nm thick and sample 2 was ~100 nm thick on average. The minimum heights in Figures 5.1 and 5.2 referred to these average film thicknesses and the maximum heights were due to the topography of the embedded GF clusters.

5.2.4 Image Analysis.

The image analysis comparing the PTIR absorption data from Figure 5.2e to the DLS data of sample 2 was performed with MATLAB® (R2012a, The MathWorks, Inc.). Initially, each pixel in Figure 5.2e was normalized between zero and one by subtracting the image's minimum PTIR value and then dividing by the maximum PTIR value. The projected areas of the GF particles were determined by separating areas of signal intensity: large, medium large, medium small and small particles corresponded to areas with a normalized signal between 0.45-1, 0.38-0.45, 0.31-0.38, and 0.2-0.31, respectively. The equivalent diameters of each particle in the image were then calculated by estimating the diameter of a circular disc with the same area as the projected area of the particle.

5.2.5 PTIR Imaging.

All measurements were performed with an Anasys Intsruments nanoIR™ AFM (Santa Barbara, CA) using C-450 silicon cantilever probes in contact mode. Ten blank/background spectra, which normalized the signal intensity as a function of laser power, were obtained and averaged before each set of experiments. The sample was irradiated by an OPO nanosecond laser at a wavelength corresponding to the sample's absorption bands (e.g., 1710 cm^{-1} or 1625 cm^{-1} for griseofulvin), which rapidly expanded and contracted causing the in-contact cantilever probe to oscillate. PTIR spectra and images were obtained by recording the peak-to-peak amplitude of the cantilever oscillations at varying locations on the sample. The first (61.0 kHz) and third (394 kHz)

modes of the cantilever were used to distinguish between nanoparticles in Figures 5.1 and 5.2, respectively [209].

The images in Figure 5.1 were 2 μm x 2 μm and irradiated at 1710 cm^{-1} with a resolution of 512 x 256 pixels. The pixel spacing on the AFM and infrared images was approximately 4 nm in the x-direction and 8 nm in the y-direction. Figures 5.2a-c were 10 μm x 10 μm images irradiated at 1625 cm^{-1} with a resolution of 512 x 256 pixels yielding a pixel spacing of 20 nm in the x-direction and 40 nm in the y-direction. Figures 5.2d-f were 2.5 μm x 2.5 μm images scanned at 1625 cm^{-1} with a resolution of 256 x 256 pixels yielding a pixel spacing of approximately 10 nm in both the x- and the y-directions. The AFM topographical map in Figure 5.4 was a 2.5 μm x 2.5 μm scan with a resolution of 512 x 256 pixels. A total of 16 spectra were collected and co-averaged at each pixel for the PTIR figures, which were scanned at 0.1-0.12 Hz. Individual spectra from 1800 to 1200 cm^{-1} were co-averages of 128 laser pulses per wavelength in increments of 4 cm^{-1}. Individual spectra from 3600 to 1000 cm^{-1} were co-averages of 256 laser pulses per wavelength in increments of 6.5 cm^{-1}.

5.3 Results and Discussion

Figure 5.1 shows the results of topographical and PTIR analysis to obtain simultaneous topographical and chemical assessment of HPMC films containing GF nanoparticles. The AFM topographical image (Figure 5.1a) reveals several micron-sized agglomerates in the polymer. To establish the chemical composition of these surface features, the sample was illuminated at 1710 cm^{-1}, a characteristic absorption band unique

to GF ketone groups [219]. The light areas of the PTIR image (Figure 5.1b) indicate regions of high material infrared absorptivity while the dark areas are regions of low absorptivity. The images also demonstrate the dependence of the PTIR signal on sample thickness [213] because infrared intensities generally varied directly with changes in local topography (*i.e.*, thicker samples/taller structures showed stronger intensities). The agreement between the topographical and chemical images confirms that the particles are GF. Furthermore, Figure 5.1c shows clear GF features, including (C=O) absorption bands at 1710 and 1664 cm^{-1} and the (C=C) absorption band at 1625 cm^{-1} for spectra obtained in the particle regions [219]. It also shows a complete absence of these features for spectra obtained outside the particle regions (in the HPMC matrix).

The high correlation between AFM topography and the PTIR signal of sample 1 suggests that the spatial resolution for PTIR on GF-HPMC films may be limited by the size of the cantilever tip. Generally, variations in the thickness and thermo-mechanical properties of the matrix surrounding the particle can reduce this resolution [210], [213], [216], [220] by introducing thermal artifacts into the system response [195], [204], [206], [208], [210], [212], [216], [221]. For example, there is an unexpected increase in apparent spatial resolution and contrast from the topographical to the PTIR images in Figure 5.1 because of the greater sensitivity of the PTIR technique on the sample thickness than the topographical contact mode of the AFM. Yet this increase is only apparent in the higher regions. The lower regions have lower contrast in the PTIR image suggesting that as the topographical variation between the HPMC matrix and GF nanoparticles decreases, the spatial resolution and contrast of the PTIR images decreases

as well. Therefore, smaller GF particles have been analyzed to determine the resolution limit of PTIR on sub-micron particles.

Topographical, PTIR, and stiffness images of a second GF nanoparticulate sample dispersed in HPMC were obtained by irradiating the material at 1625 cm^{-1} as shown in Figure 5.2. Figure 2a shows the topography of the sample, with many GF particles in the HPMC matrix. The blue areas in the PTIR images (Figures 5.2b and 5.2e) indicate areas of low infrared absorptivity, whereas the pink, yellow, and red areas (see color scale to right hand side of image) indicate regions of high infrared absorptivity, reflecting the presence of GF at these locations. Figures 5.2a-c show that a broad particle/cluster size distribution (PSD), ranging from tens of nanometers (likely primary particles) to approximately 1 micrometer (likely agglomerates), is present in the 10 x 10 μm^2 area studied. Figures 5.2d and e show a magnified area of sample 2 in which a 90 nm wide GF particle was distinguishable (shown by the solid white circle) in both the topographical and chemical maps. This demonstrates that sub-100 nm GF particles can be chemically characterized with the PTIR technique.

The stiffness images also confirm the presence of crystalline GF embedded in the HPMC matrix (Figures 5.2c and 5.2f) with increased spatial resolution because the change in the contact resonant frequency is independent of material absorptivity. In these images, the crystalline nanoparticles were noticeably stiffer than the surrounding HPMC as indicated by the bright areas on the maps. The nature of the soft regions surrounding each particle is not clear, but it is hypothesized that these are surfactant- and water-rich regions that form during the drying of the films. Independent of the nature of these soft

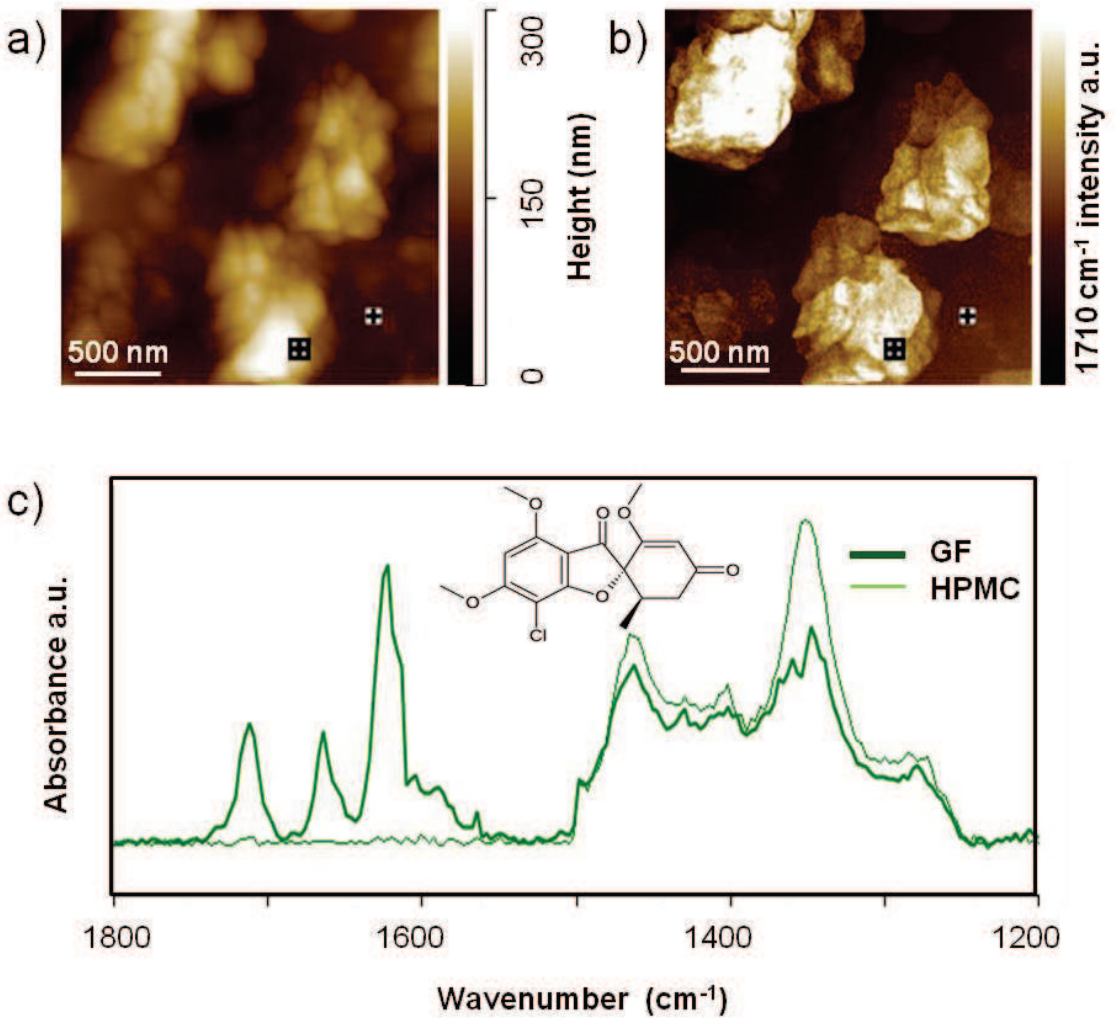

Figure 5.1 (a) AFM height image showing micron-sized GF agglomerates embedded in HPMC. (b) Simultaneous PTIR chemical image when sample was illuminated at 1710 cm^{-1} (a characteristic frequency of the C=O bonds in GF). (c) The molecular structure of GF, the GF (bold green) and HPMC (light green) spectra from 1800 to 1200 cm^{-1} and their locations (bold and regular crosshairs) in (a) and (b). Spectrum acquisition time: 3 minutes. Sample studied: sample 1 was a 1:8 (v/v) dilution of an aqueous solution originally containing 10 % GF, 2.5 % HPMC and 0.5% SDS (w/w) with d_{50} = 335.7 nm.

regions, the results in Figure 5.2 demonstrate that PTIR measurements approaching spatial resolution limits can be greatly enhanced by analyzing shifts in the contact resonant frequency (stiffness maps) in addition to the PTIR signals themselves.

To verify that the particle sizes from the PTIR analyses are representative of the true particle sizes, the distribution of the particles' equivalent diameters via image analysis (of the PTIR results) and DLS has been compared (Figure 5.3). Appropriate particle diameters from the PTIR image (Figure 5.2e) have been calculated as equivalent diameters based on the particles' projected areas. The distribution of equivalent diameters from the DLS analysis has been calculated assuming spherical particles. In the curve in Figure 5.3a, the DLS results for sample 2 are presented. There is a broad particle size distribution with d_{50}= 85 nm. After converting the projected areas of the particles in Figure 5.3b to equivalent spheres, the diameter distribution has been plotted as the histogram in Figure 5.3a. As can be seen, the size distribution has d_{50}=96 nm, and the general shape shows reasonable agreement with the DLS curve suggesting that the PTIR measurements on the sub-100 nm particles provide a reasonable representation of the particle distribution, in spite of the heterogeneous nature of the sample.

As shown in Figure 5.4, spectra were collected from HPMC and from GF particles approximately 100, 350, and 800 nm in diameter in sample 2 over the wavelengths 3600 to 1000 cm^{-1}.The color-coded crosshairs in the AFM topographical map in Figure 5.4 show the spectra acquisition locations for each particle and HPMC. The griseofulvin absorption peaks are readily distinguishable from the baseline noise for

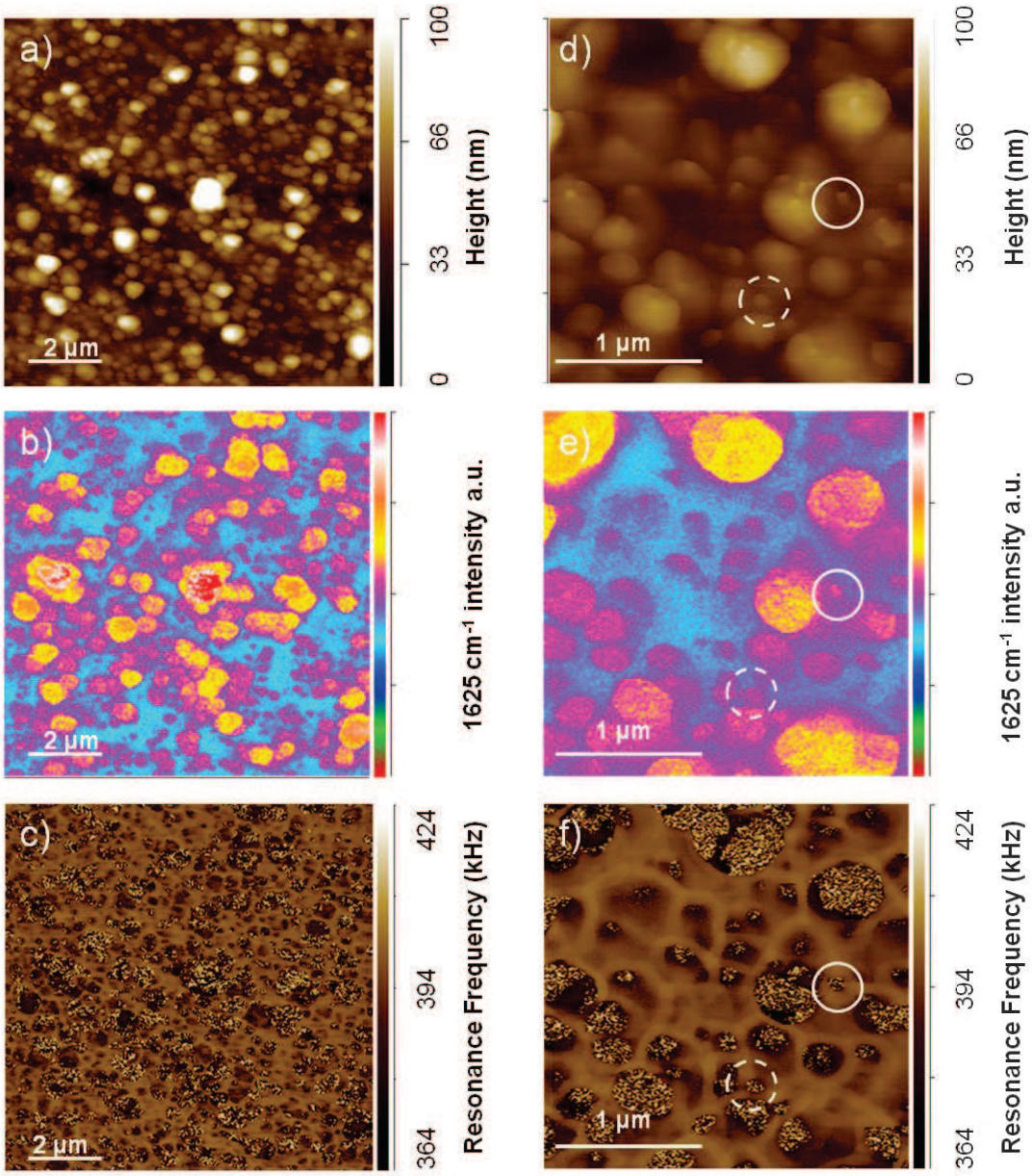

Figure 5.2. PTIR analysis of GF particles dispersed in HPMC. (a) 10x10 μm^2 AFM height image showing the broad GF particle size distribution. (b) Simultaneous PTIR chemical image illuminated at 1625 cm^{-1}, a characteristic frequency of the C=C bonds in GF; blue indicates low infrared absorptivity and pink, yellow, and red indicate areas of GF. (c) Simultaneous stiffness image, with nominal contact resonant frequency of 394 kHz; darker areas are softer than lighter areas. (d) A magnified AFM height image of sample 2 and its corresponding (e) PTIR and (f) stiffness images showing a 90 nm wide nanoparticle (solid white circle) and a 100 nm wide nanoparticle (dashed white circle). Sample studied: sample 2 was a 1:40 (v/v) dilution of an aqueous solution originally containing 10 % GF, 2.5 % HPMC and 0.2% SDS (w/w) with d_{50} = 85 nm.

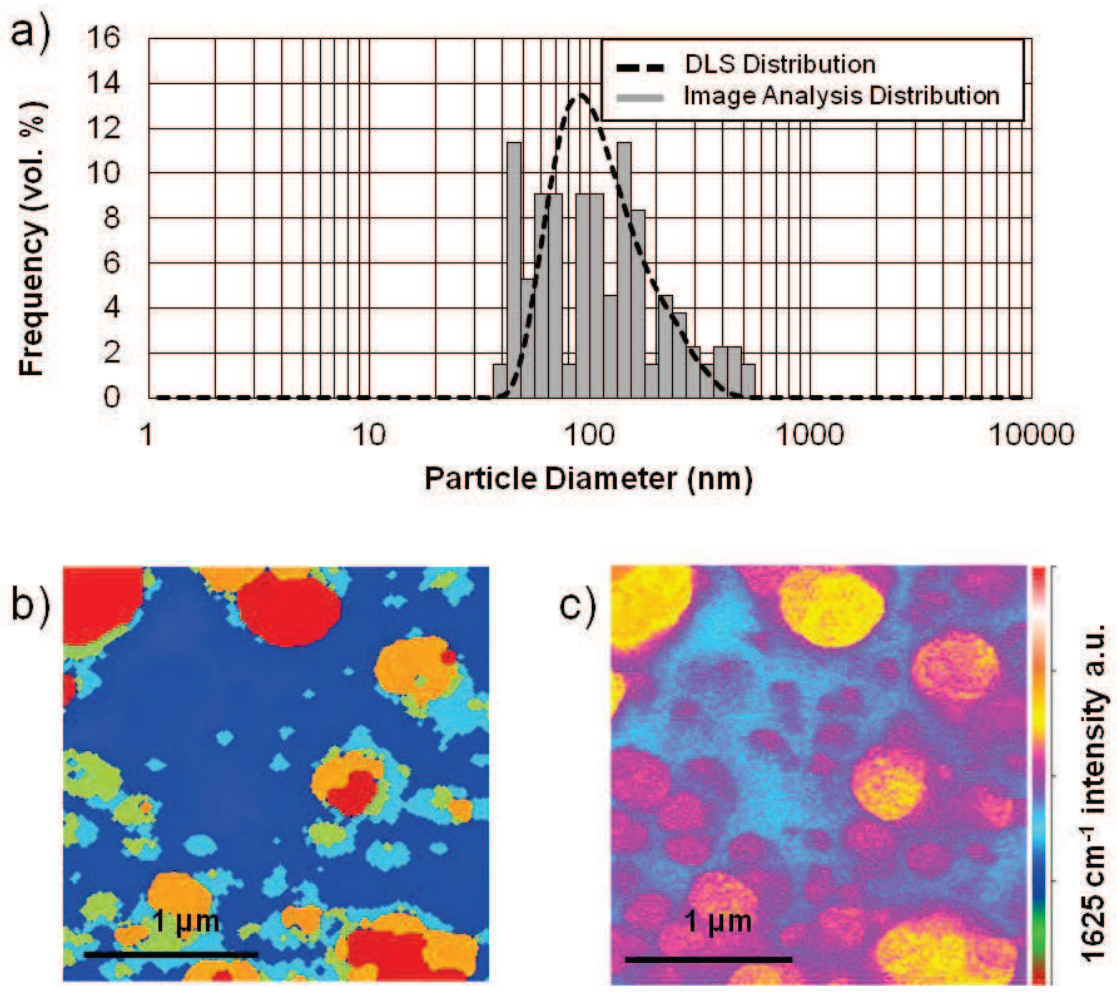

Figure 5.3 (a) Equivalent diameter particle size distribution based on the percentage of the total volume as measured by DLS (curve) and projected areas from image analysis (histogram). (b) Projected particle areas from PTIR image (2e), the different colors represent different particle areas detected by the image analysis (*i.e.*, red for the largest particles and light blue for the smallest). (c) Figure 2e, replicated for ease of comparison with (b).

all three particles, as well as from the HPMC spectrum for the spectral region 1700-1600 cm^{-1}. The self-consistent signal-to-noise ratios for the 100, 350, and 800 nm particles at 1625 cm^{-1} were 5:1, 9:1, and 15:1 demonstrating that the GF is quantifiably different from the background signal. In addition, the GF signals for the 100, 350, and 800 nm

particles at 1625 cm^{-1} were 5, 8, and 26 times greater than the HPMC signal at 1625 cm^{-1}, respectively. These results indicate that the PTIR technique is sensitive enough to chemically characterize local areas of heterogeneity to at least the 100 nm scale in drug-polymer systems.

This study demonstrates that chemical information for sub-100 nm particles can be obtained via PTIR for drug particles dispersed in a solid polymer matrix. Because the resolution of this technique depends on the infrared absorptivity and the thermomechanical properties of the components, the true resolution will vary for other samples. For materials with sufficient variation in electronic and mechanical properties, this method offers great promise for both nanoparticle and nano/micro- structural characterization of drug delivery systems.

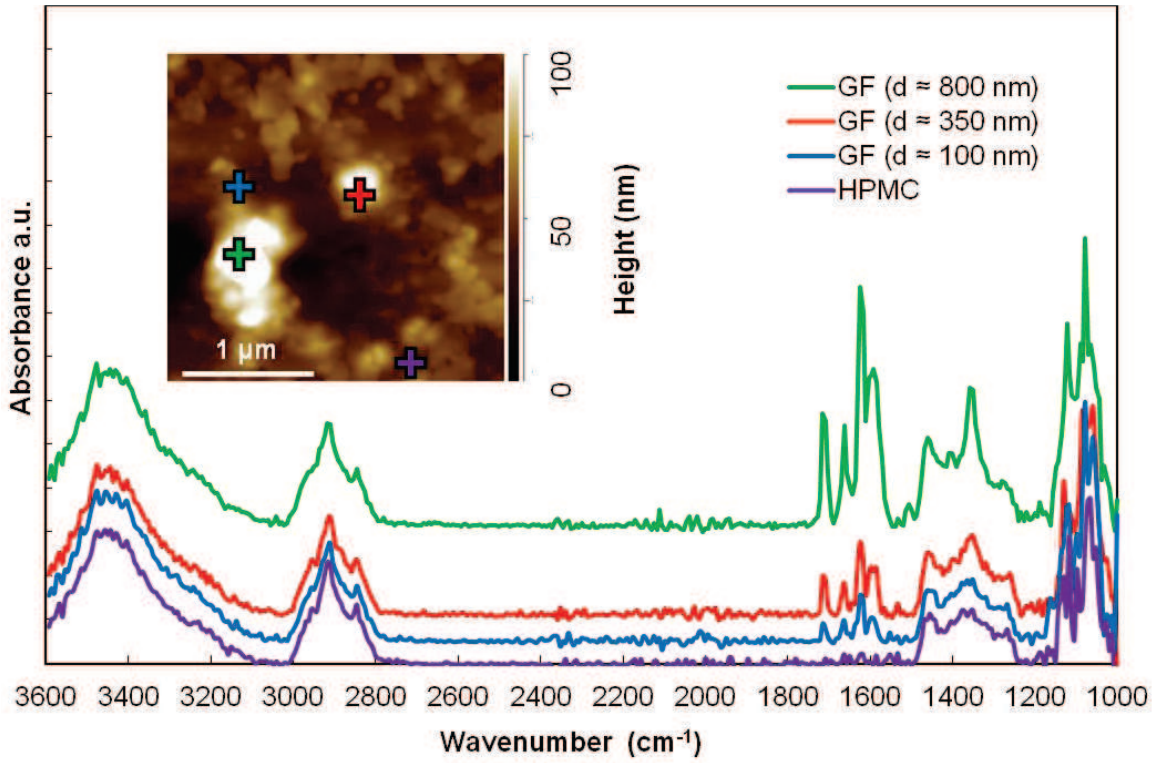

Figure 5.4 PTIR spectra of 800 nm (green), 350 nm (red), 100 nm (blue) GF particles and HPMC (purple) from 3600 to 1000 cm^{-1} and their corresponding locations indicated by the color-coded crosshairs on the AFM height image (inset). Spectrum acquisition time: 6.5 minutes.

5.4 Conclusion

The resolution and applicability of the PTIR technique for drug-polymer systems was tested using crystalline GF nanoparticles embedded in a HPMC matrix. Sub-100 nm drug particles in a polymer matrix were chemically characterized for the first time. PTIR spectra distinguishable from a background HPMC spectrum were also obtained for GF nanoparticles 100, 350, and 800 nm in diameter. This means that as modern pharmaceutical applications continue to emphasize localized drug delivery via

micro/nano-engineered structures, PTIR can be used to unambiguously chemically characterize drug formulations at these length scales.

REFERENCES

REFERENCES

[1] I. S. Fischer, R. N. Dave, J. Luke, A. D. Rosato, and R. Pfeffer, "Particle Technology in the Engineering Curriculum at NJIT," in *ASEE Annual Conference Proceedings*, 1996, pp. 1–13.

[2] B. J. Ennis, J. Green, and R. Davies, "Particle Technology: the legacy of neglect in the U.S.," *Chem. Eng. Prog.*, vol. 90, no. 4, pp. 32–43, 1994.

[3] J. L. Sinclair, "A Survey Course in Particle Technology," *Chem. Eng. Educ.*, vol. 33, pp. 266–269, 1999.

[4] A. D. Zimon, *Adhesion of Dust and Powder*, 2nd ed. New York: Consultants Bureau, 1982.

[5] N. V. Zarate, "The Influence of Interfacial Condensed Moisture on Adhesion between Solid Organic Particles and Surfaces," Purdue University, 2010.

[6] L. Xu, A. Lio, J. Hu, D. F. Ogletree, and M. Salmeron, "Wetting and Capillary Phenomena of Water on Mica," *J. Phys. Chem. B*, vol. 102, no. 3, pp. 540–548, 1998.

[7] D. Sedin and K. Rowlen, "Adhesion forces measured by atomic force microscopy in humid air," *Anal. Chem.*, vol. 72, no. 10, pp. 2183–9, May 2000.

[8] T. Thundat, X. Zheng, and G. Chen, "Role of relative humidity in atomic force microscopy imaging," *Surf. Sci.*, vol. 294, pp. L939–L943, 1993.

[9] F. Podczeck, *Particle-particle Adhesion in Pharmaceutical Powder Handling*. London: Imperial College Press, 1998.

[10] U.S. Department of the Interior: National Park Service, "Redwood : Frequently Asked Questions," 2015. [Online]. Available: http://www.nps.gov/redw/faqs.htm. [Accessed: 11-Feb-2015].

[11] W. C. Sherbrooke, A. J. Scardino, R. De Nys, and L. Schwarzkopf, “Functional morphology of scale hinges used to transport water: Convergent drinking adaptations in desert lizards (Moloch horridus and Phrynosoma cornutum),” *Zoomorphology*, vol. 126, pp. 89–102, 2007.

[12] F. T. Malik, R. M. Clement, D. T. Gethin, W. Krawszik, and a R. Parker, “Nature’s moisture harvesters: a comparative review.,” *Bioinspir. Biomim.*, vol. 9, p. 031002, 2014.

[13] P. J. Bentley and W. F. Blumer, “Uptake of water by the lizard, Moloch horridus.,” *Nature*, vol. 194, pp. 699–700, 1962.

[14] H.-J. Butt and M. Kappl, “Normal capillary forces.,” *Adv. Colloid Interface Sci.*, vol. 146, no. 1–2, pp. 48–60, Feb. 2009.

[15] J. Litster and B. Ennis, *The Science and Engineering of Granulation Processes*. London: Kluwer Academic Publisher, 2004.

[16] S. P. Beaudoin, P. Jaiswal, A. J. Harrison, J. Laster, K. Smith, M. Sweat, and M. Thomas, “Fundamental Forces in Particle Adhesion,” in *Particle Adhesion and Removal*, 1st ed., K. L. Mittal and R. Jaiswal, Eds. Wiley-Scrivener, 2015, pp. 1–79.

[17] H. Christenson, “Adhesion between surfaces in undersaturated vapors--a reexamination of the influence of meniscus curvature and surface forces,” *J. Colloid Interface Sci.*, vol. 121, no. 1, pp. 170–178, 1988.

[18] D. B. Asay, M. P. de Boer, and S. H. Kim, “Equilibrium Vapor Adsorption and Capillary Force: Exact Laplace–Young Equation Solution and Circular Approximation Approaches,” *J. Adhes. Sci. Technol.*, vol. 24, no. 15–16, pp. 2363–2382, Jan. 2010.

[19] L. Fisher and J. N. Israelachvili, “Direct measurement of the effect of meniscus forces on adhesion: A study of the applicability of macroscopic thermodynamics to microscopic liquid interfaces,” *Colloids and Surfaces*, vol. 3, pp. 303–319, 1981.

[20] L. R. Fisher and J. N. Israelachvili, “Experimental studies on the applicability of the Kelvin equation to highly curved concave menisci,” *J. Colloid Interface Sci.*, vol. 80, no. 2, pp. 528–541, Apr. 1981.

[21] H. Christenson, “Capillary condensation in systems of immiscible liquids,” *J. Colloid Interface Sci.*, vol. 104, no. 1, pp. 234–249, 1985.

[22] S. Ono and S. Kondo, “Molecular Theory of Surface Tension in Liquids,” in *Structure of Liquids / Struktur der Flüssigkeiten SE - 2*, vol. 3 / 10, Springer Berlin Heidelberg, 1960, pp. 134–280.

[23] L. G. Leal, *Advanced Transport Phenomena: Fluid Mechanics and Convective Transport Processes*. New York, NY: Cambridge University Press, 2007.

[24] A. Marchand, J. H. Weijs, J. H. Snoeijer, and B. Andreotti, “Why is surface tension a force parallel to the interface?,” *Am. J. Phys.*, vol. 79, no. October, p. 999, 2011.

[25] J. N. Israelachvili, *Intermolecular and Surface Forces, Third Edition*, 3rd ed. Boston: Academic Press, 2011.

[26] T. Young, “An Essay on the Cohesion of Fluids,” *Philos. Trans. R. Soc. London*, vol. 95, no. January, pp. 65–87, 1805.

[27] J. C. Melrose, “Thermodynamic Aspects of Capillarity,” *Ind. Eng. Chem.*, vol. 60, no. 3, pp. 53–70, 1968.

[28] J. Melrose, “Model calculations for capillary condensation,” *AIChE J.*, vol. 149, no. 1933, pp. 986–994, 1966.

[29] J. C. Melrose, “On the thermodynamic relations between immersional and adhesional wetting,” *J. Colloid Sci.*, vol. 20, no. 8, pp. 801–821, 1965.

[30] J. Gaydos, Y. Rotenberg, P. Chen, L. Boruvka, and Aw. Neumann, “Outline of the Generalized Theory of Capillarity,” in *Applied Surface Thermodynamics, Second Edition*, CRC Press, 2010, pp. 1–48.

[31] D. S. Corti, K. J. Kerr, and K. Torabi, “On the interfacial thermodynamics of nanoscale droplets and bubbles.,” *J. Chem. Phys.*, vol. 135, no. 2, p. 024701, Jul. 2011.

[32] F. P. Buff, “The Theory of Capillarity,” in *Structure of Liquids / Struktur der Flüssigkeiten SE - 3*, vol. 3 / 10, Springer Berlin Heidelberg, 1960, pp. 281–304.

[33] E. Guggenheim and N. Adam, “The thermodynamics of adsorption at the surface of solutions,” *Proc. R. Soc. London. Ser. A, Contain. Pap. a Math. Phys. Character*, vol. 139, no. 837, pp. 218–236, 1933.

[34] H. Tavana, “Thermodynamic Status of Contact Angles,” in *Applied Surface Thermodynamics, Second Edition*, CRC Press, 2010, pp. 329–421.

[35] A. W. Adamson and A. P. Gast, *Physical Chemistry of Surfaces*, 6th ed. New York: John Wiley & Sons, Inc., 1997.

[36] D. Y. Kwok and A. W. Neumann, "Contact angle measurement and contact angle interpretation," *Adv. Colloid Interface Sci.*, vol. 81, no. 3, pp. 167–249, Sep. 1999.

[37] Y. Liu, J. Wang, and X. Zhang, "Accurate determination of the vapor-liquid-solid contact line tension and the viability of Young equation.," *Sci. Rep.*, vol. 3, p. 2008, Jan. 2013.

[38] P. Lambert, *Capillary Forces in Microassembly*. Springer, 2007.

[39] F. M. Orr, L. E. Scriven, and a. P. Rivas, "Pendular rings between solids: meniscus properties and capillary force," *J. Fluid Mech.*, vol. 67, p. 723, 1975.

[40] M. Schrader, P. Virnau, D. Winter, T. Zykova-Timan, and K. Binder, "Methods to extract interfacial free energies of flat and curved interfaces from computer simulations," *Eur. Phys. J. Spec. Top.*, vol. 177, no. 1, pp. 103–127, Oct. 2009.

[41] A. Nold, D. N. Sibley, B. D. Goddard, and S. Kalliadasis, "Fluid structure in the immediate vicinity of an equilibrium three-phase contact line and assessment of disjoining pressure models using density functional theory," pp. 1–15, Jun. 2014.

[42] C. M. Mate, "Application of disjoining and capillary pressure to liquid lubricant films in magnetic recording," *J. Appl. Phys.*, vol. 72, no. 7, p. 3084, 1992.

[43] A. Shapiro and E. Stenby, "Kelvin equation for a non-ideal multicomponent mixture," *Fluid Phase Equilib.*, vol. 134, pp. 87–101, 1997.

[44] A. a. Shapiro and E. H. Stenby, "Thermodynamics of the multicomponent vapor–liquid equilibrium under capillary pressure difference," *Fluid Phase Equilib.*, vol. 178, no. 1–2, pp. 17–32, Mar. 2001.

[45] R. Evans and U. Marini Bettolo Marconi, "Phase equilibria and solvation forces for fluids confined between parallel walls," *J. Chem. Phys.*, vol. 86, no. 12, pp. 7138–7148, 1987.

[46] J. Melrose, "Chemical potential changes in capillary condensation," *J. Colloid Interface Sci.*, vol. 38, no. 2, pp. 312–322, 1972.

[47] R. Digilov, "Kelvin Equation for Meniscuses of Nanosize Dimensions," *Langmuir*, vol. 16, no. 3, pp. 1424–1427, Feb. 2000.

[48] O. H. Pakarinen, A. H. Foster, M. Paajanen, T. Kalinainen, J. Katainen, I. Makkonen, J. Lahtinen, and R. M. Nieminen, "Towards an accurate description of the capillary force in nanoparticle-surface interactions," *Model. Simul. Mater. Sci. Eng.*, vol. 13, pp. 1175–1186, 2005.

[49] A. P. Hughes, U. Thiele, and A. J. Archer, "Liquid drops on a surface: Using density functional theory to calculate the binding potential and drop profiles and comparing with results from mesoscopic modelling," *J. Chem. Phys.*, vol. 142, p. 074702, 2015.

[50] A. Harrison, D. S. Corti, and S. P. Beaudoin, "Capillary forces in nanoparticle adhesion: A review of AFM methods," *Part. Sci. Technol.*, 2015.

[51] J. McFarlane and D. Tabor, "Adhesion of solids and the effect of surface films," *Proc. R. Soc. Lond. A. Math. Phys. Sci.*, vol. 202, no. 1069, pp. 224–243, 1950.

[52] S. You and M. P. Wan, "Modeling and experiments of the adhesion force distribution between particles and a surface," *Langmuir*, vol. 30, pp. 6808–6818, 2014.

[53] M. Kohonen and H. Christenson, "Capillary condensation of water between rinsed mica surfaces," *Langmuir*, vol. 16, no. 18, pp. 7285–7288, 2000.

[54] H.-J. Butt, B. Cappella, and M. Kappl, "Force measurements with the atomic force microscope: Technique, interpretation and applications," *Surf. Sci. Rep.*, vol. 59, no. 1–6, pp. 1–152, Oct. 2005.

[55] M. Farshchi-Tabrizia, M. Kappl, and H.-J. Butt, "Influence of Humidity on Adhesion: An Atomic Force Microscope Study," *J. Adhes. Sci. Technol.*, vol. 22, no. 2, pp. 181–203, Apr. 2008.

[56] L. Sirghi, R. Szoszkiewicz, and E. Riedo, "Volume of a nanoscale water bridge.," *Langmuir*, vol. 22, no. 3, pp. 1093–8, Jan. 2006.

[57] A. Ata, Y. I. Rabinovich, and R. K. Singh, "Role of surface roughness in capillary adhesion," *J. Adhes. Sci. Technol.*, vol. 16, no. 4, pp. 337–346, Apr. 2002.

[58] L. J. D. Frink and F. van Swol, "A molecular theory for surface forces adhesion measurements," *J. Chem. Phys.*, vol. 106, no. 9, p. 3782, 1997.

[59] X. Xue and A. A. Polycarpou, "An improved meniscus surface model for contacting rough surfaces.," *J. Colloid Interface Sci.*, vol. 311, no. 1, pp. 203–11, Jul. 2007.

[60] S. C. Chen and J. F. Lin, “Detailed modeling of the adhesion force between an AFM tip and a smooth flat surface under different humidity levels,” *J. Micromechanics Microengineering*, vol. 18, no. 11, p. 115006, Nov. 2008.

[61] H. Schubert, “Capillary forces-modeling and application in particulate technology,” *Powder Technol.*, vol. 37, no. 1, pp. 105–116, 1984.

[62] S. You and M. P. Wan, “Mathematical models for the van der Waals force and capillary force between a rough particle and surface.,” *Langmuir*, vol. 29, no. 29, pp. 9104–17, Jul. 2013.

[63] M. Köber, E. Sahagún, P. García-Mochales, F. Briones, M. Luna, and J. J. Sáenz, “Nanogeometry matters: unexpected decrease of capillary adhesion forces with increasing relative humidity.,” *Small*, vol. 6, no. 23, pp. 2725–30, Dec. 2010.

[64] P. B. Paramonov and S. F. Lyuksyutov, “Density-functional description of water condensation in proximity of nanoscale asperity.,” *J. Chem. Phys.*, vol. 123, no. 8, p. 084705, Aug. 2005.

[65] J. Jang and G. C. Schatz, “Lattice Gas Monte Carlo Simulation of Capillary Forces in Atomic Force Microscopy,” *J. Adhes. Sci. Technol.*, vol. 24, pp. 37–41, 2010.

[66] D. B. Asay and S. H. Kim, “Effects of adsorbed water layer structure on adhesion force of silicon oxide nanoasperity contact in humid ambient.,” *J. Chem. Phys.*, vol. 124, no. 17, p. 174712, May 2006.

[67] H. J. Choi, J. Y. Kim, S. D. Hong, M. Y. Ha, and J. Jang, “Molecular simulation of the nanoscale water confined between an atomic force microscope tip and a surface,” *Mol. Simul.*, vol. 35, no. 6, pp. 466–472, May 2009.

[68] A. Ptak, H. Gojzewski, M. Kappl, and H.-J. Butt, “Influence of humidity on the nanoadhesion between a hydrophobic and a hydrophilic surface,” *Chem. Phys. Lett.*, vol. 503, no. 1–3, pp. 66–70, Feb. 2011.

[69] N. V Zarate, A. J. Harrison, J. D. Litster, and S. P. Beaudoin, “Effect of relative humidity on onset of capillary forces for rough surfaces.,” *J. Colloid Interface Sci.*, vol. 411, pp. 265–72, Dec. 2013.

[70] R. Jones, H. M. Pollock, J. A. S. Cleaver, and C. S. Hodges, “Adhesion Forces between Glass and Silicon Surfaces in Air Studied by AFM: Effects of Relative Humidity, Particle Size, Roughness, and Surface Treatment,” *Langmuir*, vol. 18, no. 21, pp. 8045–8055, Oct. 2002.

[71] J. Jang, G. C. Schatz, and M. A. Ratner, “Capillary force in atomic force microscopy.,” *J. Chem. Phys.*, vol. 120, no. 3, pp. 1157–60, Jan. 2004.

[72] M. He, A. Szuchmacher Blum, D. E. Aston, C. Buenviaje, R. M. Overney, and R. Luginbühl, “Critical phenomena of water bridges in nanoasperity contacts,” *J. Chem. Phys.*, vol. 114, no. 3, pp. 1355–1360, 2001.

[73] T. Eastman, “Adhesion forces between surface-modified AFM tips and a mica surface,” *Langmuir*, vol. 12, no. 11, pp. 2859–2862, 1996.

[74] B. Bhushan and S. Sundararajan, “Micro/nanoscale friction and wear mechanisms of thin films using atomic force and friction force microscopy,” *Acta Mater.*, vol. 46, no. 11, pp. 3793–3804, Jul. 1998.

[75] H. Knapp and A. Stemmer, “Preparation, comparison and performance of hydrophobic AFM tips,” *Surf. interface Anal.*, vol. 27, pp. 324–331, 1999.

[76] C. Ziebert and K.-H. Zum Gahr, “Microtribological Properties of Two-Phase Al 2 O 3 Ceramic Studied by AFM and FFM in Air of Different Relative Humidity,” *Tribol. Lett.*, vol. 17, no. 4, pp. 901–909, 2004.

[77] D.-I. Kim, J. Grobelny, N. Pradeep, and R. F. Cook, “Origin of adhesion in humid air.,” *Langmuir*, vol. 24, no. 5, pp. 1873–7, Mar. 2008.

[78] J. Tang, C. Wang, M. Liu, and M. Su, “Effect of humidity on the surface adhesion force of inorganic crystals by the force spectrum method,” *Chinese Sci. Bull.*, vol. 46, no. 11, pp. 912–914, 2001.

[79] A. Fukunishi and Y. Mori, “Adhesion force between particles and substrate in a humid atmosphere studied by atomic force microscopy,” *Adv. Powder Technol.*, vol. 17, no. 5, pp. 567–580, 2006.

[80] A. Çolak, H. Wormeester, H. J. W. Zandvliet, and B. Poelsema, “The influence of instrumental parameters on the adhesion force in a flat-on-flat contact geometry,” *Appl. Surf. Sci.*, vol. 308, pp. 106–112, Jul. 2014.

[81] A. Çolak, H. Wormeester, H. J. W. Zandvliet, and B. Poelsema, “Surface adhesion and its dependence on surface roughness and humidity measured with a flat tip,” *Appl. Surf. Sci.*, vol. 258, no. 18, pp. 6938–6942, Jul. 2012.

[82] H.-J. Butt, M. Farshchi-Tabrizi, and M. Kappl, “Using capillary forces to determine the geometry of nanocontacts,” *J. Appl. Phys.*, vol. 100, no. 2, p. 024312, 2006.

[83] S. H. Yang, M. Nosonovsky, H. Zhang, and K.-H. Chung, “Nanoscale water capillary bridges under deeply negative pressure,” *Chem. Phys. Lett.*, vol. 451, no. 1–3, pp. 88–92, Jan. 2008.

[84] E.-S. Yoon, S. H. Yang, H.-G. Han, and H. Kong, “An experimental study on the adhesion at a nano-contact,” *Wear*, vol. 254, no. 10, pp. 974–980, Jul. 2003.

[85] M. Paajanen, J. Katainen, O. H. Pakarinen, A. S. Foster, and J. Lahtinen, “Experimental humidity dependency of small particle adhesion on silica and titania,” *J. Colloid Interface Sci.*, vol. 304, no. 2, pp. 518–523, 2006.

[86] E. J. Thoreson, J. Martin, and N. A. Burnham, “The role of few-asperity contacts in adhesion,” *J. Colloid Interface Sci.*, vol. 298, no. 1, pp. 94–101, 2006.

[87] X. Xiao and L. Qian, “Investigation of Humidity-Dependent Capillary Force,” *Langmuir*, vol. 16, no. 21, pp. 8153–8158, 2000.

[88] M. Fujihira, D. Aoki, Y. Okabe, and H. Takano, “Effect of capillary force on friction force microscopy: a scanning hydrophilicity microscope,” *Chem. Lett.*, vol. 25, no. 7, pp. 499–500, 1996.

[89] S. Biggs, R. G. Cain, R. R. Dagastine, and N. W. Page, “Direct measurements of the adhesion between a glass particle and a glass surface in a humid atmosphere,” *J. Adhes. Sci. Technol.*, vol. 16, no. 7, pp. 869–885, Jan. 2002.

[90] A. A. Feiler, P. Jenkins, and M. W. Rutland, “Effect of relative humidity on adhesion and frictional properties of micro- and nano-scopic contacts,” *J. Adhes. Sci. Technol.*, vol. 19, no. 3–5, pp. 165–179, Jan. 2005.

[91] D. Triantafyllidis, L. Li, and F. H. Stott, “The effects of laser-induced modification of surface roughness of Al2O3-based ceramics on fluid contact angle,” *Mater. Sci. Eng. A*, vol. 390, no. 1–2, pp. 271–277, Jan. 2005.

[92] A. P. Tetuko, D. S. Khaerudini, P. Sardjono, P. Sebayang, and G. Rosengarten, “Superhydrophobic surface as a fluid enhancement material in engineering applications,” vol. 3, pp. 3–6, 2013.

[93] G. Grenci, G. Birarda, E. Mitri, L. Businaro, S. Pacor, L. Vaccari, and M. Tormen, “Optimization of microfluidic systems for IRMS long term measurement of living cells,” *Microelectron. Eng.*, vol. 98, pp. 698–702, Oct. 2012.

[94] H. K. Christenson and J. N. Israelachvili, “Growth of Ionic Crystallites on Exposed Surfaces,” *J. Colloid Interface Sci.*, vol. 117, no. 2, pp. 576–577, 1987.

[95] J. Israelachvili, “Thin Film Studies Using Multiple-Beam Interferometry,” *J. Colloid Interface Sci.*, vol. 44, no. 2, pp. 259–272, 1973.

[96] B. V Derjaguin, Z. M. Zorin, Y. I. Rabinovich, and N. V. Churaev, “Results of Analytical Investigation of the Composition of ‘Anomalous’ Water,” *J. Colloid Interface Sci.*, vol. 46, no. 3, pp. 437–441, 1974.

[97] F. W. DelRio, M. L. Dunn, L. M. Phinney, C. J. Bourdon, and M. P. de Boer, “Rough surface adhesion in the presence of capillary condensation,” *Appl. Phys. Lett.*, vol. 90, no. 16, p. 163104, 2007.

[98] P. J. van Zwol, G. Palasantzas, and J. T. M. De Hosson, “Influence of roughness on capillary forces between hydrophilic surfaces,” *Phys. Rev. E*, vol. 78, pp. 031601–031606, 2008.

[99] P. J. van Zwol, G. Palasantzas, and J. T. M. De Hosson, “Influence of random roughness on the adhesion between metal surfaces due to capillary condensation,” *Appl. Phys. Lett.*, vol. 91, no. 10, p. 101905, 2007.

[100] Y. Rabinovich, J. Adler, M. Esayanur, and A. Ata, “Capillary forces between surfaces with nanoscale roughness,” *Adv. Colloid Interface Sci.*, vol. 96, no. 1–3, pp. 213–230, 2002.

[101] M. P. Boer, “Capillary Adhesion Between Elastically Hard Rough Surfaces,” *Exp. Mech.*, vol. 47, no. 1, pp. 171–183, Jan. 2007.

[102] M. Kohonen, N. Maeda, and H. Christenson, “Kinetics of Capillary Condensation in a Nanoscale Pore,” *Phys. Rev. Lett.*, vol. 82, pp. 4667–4670, 1999.

[103] Z. Wei and Y.-P. Zhao, “Growth of liquid bridge in AFM,” *J. Phys. D. Appl. Phys.*, vol. 40, no. 14, pp. 4368–4375, Jul. 2007.

[104] Y. I. Rabinovich, A. Singh, M. Hahn, S. Brown, and B. Moudgil, “Kinetics of liquid annulus formation and capillary forces,” *Langmuir*, vol. 27, pp. 13514–13523, 2011.

[105] Greg Haugstad, “Probing Material Properties II: Adhesive Nanomechanics and Mapping Distance-Dependent Interactions,” in *Atomic Force Microscopy: Understanding Basic Modes and Advanced Applications*, John Wiley & Sons, Inc., 2012, pp. 258–329.

[106] D. B. Asay and S. H. Kim, “Evolution of the adsorbed water layer structure on silicon oxide at room temperature.,” *J. Phys. Chem. B*, vol. 109, no. 35, pp. 16760–3, Sep. 2005.

[107] H.-J. Butt, “Capillary forces: influence of roughness and heterogeneity.,” *Langmuir*, vol. 24, no. 9, pp. 4715–21, May 2008.

[108] Y. Men, X. Zhang, and W. Wang, “Rupture kinetics of liquid bridges during a pulling process: a kinetic density functional theory study.,” *J. Chem. Phys.*, vol. 134, no. 12, p. 124704, Mar. 2011.

[109] E. A. Boucher, M. J. B. Evans, and S. McGarry, “Capillary Phenomena XX. Fluid Bridges between Horizontal Solid Plates in a Gravitational Field,” *J. Colloid Interface Sci.*, vol. 89, no. 1, pp. 154–165, 1982.

[110] E. A. Boucher and M. J. B. Evans, “Capillary phenomena. XII. Properties of fluid bridges between solids in a gravitational field,” *J. Colloid Interface Sci.*, vol. 75, no. 2, pp. 409–418, 1980.

[111] E. a. Boucher, M. J. B. Evans, and H. J. Kent, “Capillary Phenomena. II. Equilibrium and Stability of Rotationally Symmetric Fluid Bodies,” *Proc. R. Soc. A Math. Phys. Eng. Sci.*, vol. 349, no. 1656, pp. 81–100, 1976.

[112] J. Qian and H. Gao, “Scaling effects of wet adhesion in biological attachment systems,” *Acta Biomater.*, vol. 2, pp. 51–58, 2006.

[113] P. Prokopovich and V. Starov, “Adhesion models: from single to multiple asperity contacts.,” *Adv. Colloid Interface Sci.*, vol. 168, no. 1–2, pp. 210–22, Oct. 2011.

[114] J. Hu, X. D. Xiao, D. F. Ogletree, and M. Salmeron, “Imaging the condensation and evaporation of molecularly thin films of water with nanometer resolution.,” *Science*, vol. 268, no. 5208, pp. 267–9, Apr. 1995.

[115] D. Asay, A. Barnette, and S. Kim, “Effects of Surface Chemistry on Structure and Thermodynamics of Water Layers at Solid-Vapor Interfaces,” *J. Phys. Chem. C*, vol. 113, pp. 2128–2133, 2009.

[116] J. Israelachvili, *Intermolecular and surface forces: revised third edition*, 3rd ed. Burlington: Academic Press, 2011.

[117] A. Fogden and L. R. White, “Contact elasticity in the presence of capillary condensation,” *J. Colloid Interface Sci.*, vol. 138, no. 2, pp. 414–430, 1990.

[118] D. Frenkel and B. Smit, *Understanding Molecular Simulation: From Algorithms to Applications*. San Diego, CA: Academic Press, 2002.

[119] S. M. M. Langroudi, M. Ghassemi, a. Shahabi, and H. R. Nejad, “A molecular dynamics study of effective parameters on nano-droplet surface tension,” *J. Mol. Liq.*, vol. 161, no. 2, pp. 85–90, Jun. 2011.

[120] J.-A. Ko, H.-J. Choi, M.-Y. Ha, S.-D. Hong, and H.-S. Yoon, “A study on the behavior of water droplet confined between an atomic force microscope tip and rough surfaces.,” *Langmuir*, vol. 26, no. 12, pp. 9728–35, Jun. 2010.

[121] S. Cheng and M. O. Robbins, “Capillary adhesion at the nanometer scale,” *Phys. Rev. E*, vol. 89, no. 6, p. 062402, Jun. 2014.

[122] J. Jang, G. Schatz, and M. Ratner, “Capillary Force on a Nanoscale Tip in Dip-Pen Nanolithography,” *Phys. Rev. Lett.*, vol. 90, no. 15, pp. 18–21, Apr. 2003.

[123] J. Jang, G. Schatz, and M. Ratner, “How Narrow Can a Meniscus Be?,” *Phys. Rev. Lett.*, vol. 92, no. 8, pp. 1–4, Feb. 2004.

[124] J. Jang, M. A. Ratner, and G. C. Schatz, “Atomic-scale roughness effect on capillary force in atomic force microscopy.,” *J. Phys. Chem. B*, vol. 110, no. 2, pp. 659–62, Jan. 2006.

[125] J. Jang, M. Yang, and G. Schatz, “Microscopic origin of the humidity dependence of the adhesion force in atomic force microscopy.,” *J. Chem. Phys.*, vol. 126, no. 17, p. 174705, May 2007.

[126] J. Jang, J. Jeon, and S. Hwang, “Monte Carlo study on the water bridge that produces the pull-off force in atomic force microscopy,” *Colloids Surfaces A Physicochem. Eng. Asp.*, vol. 300, no. 1–2, pp. 60–64, Jun. 2007.

[127] S. Han and J. Jang, “A thermodynamic perturbation method to calculate surface forces in confined-fluid systems,” *Bull. Korean Chem. Soc.*, vol. 27, no. 1, pp. 31–32, 2006.

[128] J. Jang, J. Sung, and G. C. Schatz, “Influence of Surface Roughness on the Pull-Off Force in Atomic Force Microscopy,” *J. Phys. Chem. C*, vol. 111, no. 12, pp. 4648–4654, Mar. 2007.

[129] H. Shinto, K. Uranishi, M. Miyahara, and K. Higashitani, “Wetting-induced interaction between rigid nanoparticle and plate: A Monte Carlo study,” *J. Chem. Phys.*, vol. 116, no. 21, p. 9500, 2002.

[130] O. Stukalov, C. a. Murray, A. Jacina, and J. R. Dutcher, “Relative humidity control for atomic force microscopes,” *Rev. Sci. Instrum.*, vol. 77, no. 3, p. 033704, 2006.

[131] J. Jang, G. C. Schatz, and M. a. Ratner, “Liquid meniscus condensation in dip-pen nanolithography,” *J. Chem. Phys.*, vol. 116, no. 9, p. 3875, 2002.

[132] E. Kierlik, P. Monson, M. Rosinberg, L. Sarkisov, and G. Tarjus, "Capillary Condensation in Disordered Porous Materials: Hysteresis versus Equilibrium Behavior," *Phys. Rev. Lett.*, vol. 87, no. 5, p. 055701, Jul. 2001.

[133] E. Kierlik, P. Monson, M. Rosiberg, and G. Tarjus, "Adsorption hysteresis and capillary condensation in disordered porous solids: a density functional study," *J. Phys. Condens. Matter*, vol. 14, pp. 9295–9315, 2002.

[134] P. Monson, "Contact angles, pore condensation, and hysteresis: insights from a simple molecular model," *Langmuir*, vol. 24, pp. 12295–12302, 2008.

[135] Y. Men, X. Zhang, and W. Wang, "Capillary liquid bridges in atomic force microscopy: formation, rupture, and hysteresis.," *J. Chem. Phys.*, vol. 131, no. 18, p. 184702, Nov. 2009.

[136] K. Binder, "Simulations of Interfacial Phenomena in Soft Condensed Matter and Nanoscience," *J. Phys. Conf. Ser.*, vol. 510, p. 012002, May 2014.

[137] H. Kim, B. Smit, and J. Jang, "Monte Carlo Study on the Water Meniscus Condensation and Capillary Force in Atomic Force Microscopy," *J. Phys. Chem. C*, vol. 116, no. 41, pp. 21923–21931, Oct. 2012.

[138] K. Binder, D. Landau, and M. Müller, "Monte Carlo studies of wetting, interface localization and capillary condensation," *J. Stat. Phys.*, vol. 110, no. March, pp. 1411–1514, 2003.

[139] E. Albano, K. Binder, and W. Paul, "Capillary condensation in the two-dimensional lattice gas: A Monte Carlo test of fluctuation corrections to the Kelvin equation," *J. Phys. A Math. Theor.*, vol. 30, pp. 3285–3297, 1997.

[140] S. Kim and S. H. Ehrman, "Grand canonical Monte Carlo simulation study of capillary condensation between nanoparticles.," *J. Chem. Phys.*, vol. 127, no. 13, p. 134702, Oct. 2007.

[141] Y. Men and X. Zhang, "Physical basis for constrained lattice density functional theory.," *J. Chem. Phys.*, vol. 136, no. 12, p. 124704, Mar. 2012.

[142] M. Nosonovsky, S. Yang, and H. Zhang, "On the sensitivity of the capillary adhesion force to the surface roughness," in *Scanning Probe Microscopy in Nanoscience and Nanotechnology 2*, 2011, pp. 573–586.

[143] R. Pandit, M. Schick, and M. Wortis, "Systematics of multilayer adsorption phenomena on attractive substrates," *Phys. Rev. B*, vol. 26, no. 9, pp. 5112–5140, 1982.

[144] D. P. Landau and K. Binder, *A Guide to Monte Carlo Simulations in Statistical Physics*, 2nd ed. Cambridge: Cambridge University Press, 2005.

[145] F. Wang and D. Landau, "Determining the density of states for classical statistical models: A random walk algorithm to produce a flat histogram," *Phys. Rev. E*, vol. 64, p. 056101, 2001.

[146] F. Wang and D. Landau, "Efficient, Multiple-Range Random Walk Algorithm to Calculate the Density of States," *Phys. Rev. Lett.*, vol. 86, no. 10, pp. 2050–2053, Mar. 2001.

[147] T. L. Hill, *Statistical Mechanics*. New York, NY: McGraw-Hill Book Company, Inc, 1956.

[148] D. Andrienko, P. Patricio, and O. I. Vinogradova, "Capillary bridging and long-range attractive forces in a mean-field approach.," *J. Chem. Phys.*, vol. 121, no. 9, pp. 4414–23, Sep. 2004.

[149] J. W. Tester and M. Modell, *Thermodynamics and Its Applications*, 3rd ed. Upper Saddle River: Prentice Hall PTR, 1997.

[150] A. Malijevský and G. Jackson, "A perspective on the interfacial properties of nanoscopic liquid drops.," *J. Phys. Condens. Matter*, vol. 24, no. 46, p. 464121, Nov. 2012.

[151] N. Vargaftik, B. Volkov, and L. Voljak, "International tables of the surface tension of water," *J. Phys. Chem. Ref. Data*, vol. 12, no. 3, pp. 817–820, 1983.

[152] A. Tröster and K. Binder, "Positive Tolman Length in a Lattice Gas with Three-Body Interactions," *Phys. Rev. Lett.*, vol. 107, no. 26, p. 265701, Dec. 2011.

[153] A. Tröster, M. Oettel, B. Block, P. Virnau, and K. Binder, "Numerical approaches to determine the interface tension of curved interfaces from free energy calculations.," *J. Chem. Phys.*, vol. 136, no. 6, p. 064709, Feb. 2012.

[154] K. Torabi and D. S. Corti, "Towards a Molecular Theory of Homogeneous Bubble Nucleation II. Calculation of the Number Density of Critical Nuclei and the Rate of Nucleation," *J. Phys. Chem. B*, vol. In Review, 2013.

[155] W. Thomson, "On the equilibrium of vapour at a curved surface of liquid," *Philos. Mag. Ser. 4*, vol. 42, no. 282, pp. 448–452, 1871.

[156] R. P. Jaiswal, G. Kumar, C. M. Kilroy, and S. P. Beaudoin, "Modeling and validation of the van der Waals force during the adhesion of nanoscale objects to rough surfaces: a detailed description.," *Langmuir*, vol. 25, no. 18, pp. 10612–23, Sep. 2009.

[157] A. J. Harrison, A. Otte, T. Carvajal, R. Pinal, and S. P. Beaudoin, "Cohesive Hamaker Constants and Dispersive Surface Energies of RDX, PETN,TNT, and Ammonium Nitrate-Based Explosives," *Propellants, Explos. Pyrotech.*, 2015.

[158] H. Hamaker, "The London—van der Waals attraction between spherical particles," *Physica*, vol. 4, no. 10, pp. 1058–1072, 1937.

[159] V. A. Parsegian, *Van der Waals forces : a handbook for biologists, chemists, engineers, and physicists*. New York : Cambridge University Press, 2006.

[160] F. Fowkes, "Attractive forces at interfaces," *Ind. Eng. Chem.*, vol. 56, no. 12, pp. 40–52, 1964.

[161] C. J. van Oss, *Interfacial Forces in Aqueous Media*, 2nd ed. New York: Taylor & Francis, 2006.

[162] F. M. Fowkes, "Donor-Acceptor Interactions at Interfaces," *J. Adhes.*, vol. 4, no. 2, pp. 155–159, Jun. 1972.

[163] D. Owens and R. Wendt, "Estimation of the surface free energy of polymers," *J. Appl. Polym. Sci.*, vol. 13, pp. 1741–1747, 1969.

[164] M. Nardin and E. Papirer, "Relationship between vapor pressure and surface energy of liquids: application to inverse gas chromatography," *J. Colloid Interface Sci.*, vol. 137, no. 2, pp. 534–545, Jul. 1990.

[165] E. Washburn, "The dynamics of capillary flow," *Phys. Rev.*, vol. 17, no. 3, pp. 273–283, 1921.

[166] M. Belgacem and A. Gandini, "Inverse gas chromatography as a tool to characterize dispersive and acid-base properties of the surface of fibers and powders," in *Interfacial Phenomena in Chromatography*, E. Pefferkorn, Ed. CRC Press, 1999, pp. 42–124.

[167] U. Teipel, I. Mikonsaari, and S. Torry, "Wettability Analysis," in *Energetic Materials: Particle Processing and Characterization*, U. Teipel, Ed. Weinheim: Weinheim : Wiley-VCH, 2005, pp. 403–431.

[168] Y. Luo and M. Du, “The Use of Inverse Gas Chromatography (IGC) to Determine the Surface Energy of RDX,” *Propellants, Explos. Pyrotech.*, vol. 32, no. 6, pp. 496–501, Dec. 2007.

[169] V. Lazarev, “Surface tension as a function of temperature for some molten metals,” *Theor. Exp. Chem.*, vol. 3, no. 4, pp. 294–295, 1967.

[170] P. Jandura, B. Riedl, and B. V. Kokta, “Inverse gas chromatography study on partially esterified paper fiber.,” *J. Chromatogr. A*, vol. 969, no. 1–2, pp. 301–11, Sep. 2002.

[171] D. Kwok, D. Li, and A. Neumann, “Evaluation of the Lifshitz-van der Waals/acid-base approach to determine interfacial tensions,” *Langmuir*, vol. 10, pp. 1323–1328, 1994.

[172] D. Kwok and A. Neumann, “A simple experimental test of the lifshitz-van der waals/acid-base approach to determine interfacial tensions,” *Can. J. Chem. Eng.*, vol. 74, pp. 1–3, 1996.

[173] D. Y. Kwok, “The usefulness of the Lifshitz–van der Waals/acid–base approach for surface tension components and interfacial tensions,” *Colloids Surfaces A Physicochem. Eng. Asp.*, vol. 156, no. 1–3, pp. 191–200, Oct. 1999.

[174] M. Greiveldinger and M. Shanahan, “A Critique of the Mathematical Coherence of Acid/Base Interfacial Free Energy Theory.,” *J. Colloid Interface Sci.*, vol. 215, no. 1, pp. 170–178, Jul. 1999.

[175] D. A. Skoog and J. J. Leary, *Principles of instrumental analysis*, 4th ed. Fort Worth: Saunders College Publishing, 1992.

[176] J. Schultz, L. Lavielle, and C. Martin, “The Role of the Interface in Carbon Fibre-Epoxy Composites,” *J. Adhes.*, vol. 23, no. 1, pp. 45–60, Sep. 1987.

[177] F. M. Fowkes and M. a. Mostafa, “Acid-Base Interactions in Polymer Adsorption,” *Ind. Eng. Chem. Prod. Res. Dev.*, vol. 17, no. 1, pp. 3–7, Mar. 1978.

[178] D. Kwok, D. Li, and A. Neumann, “Fowkes’ surface tension component approach revisited,” *Colloids Surfaces A Physicochem. Eng. Asp.*, vol. 89, pp. 181–191, 1994.

[179] J. Kloubek, “Development of methods for surface free energy determination using contact angles of liquids on solids,” *Adv. Colloid Interface Sci.*, vol. 38, pp. 99–142, Mar. 1992.

[180] F. Fowkes, M. Kaczinski, and D. Dwight, “Characterization of polymer surface sites with contact angles of test solutions. 1. Phenol and iodine adsorption from methylene iodide onto PMMA films,” *Langmuir*, vol. 7, no. 11, pp. 2464–2470, 1991.

[181] R. J. Hudson, P. Zioupos, and P. P. Gill, “Investigating the Mechanical Properties of RDX Crystals Using Nano-Indentation,” *Propellants, Explos. Pyrotech.*, vol. 37, no. 2, pp. 191–197, Apr. 2012.

[182] S. M. Kaye, *Encyclopedia of Explosives and Related Items. Volume 8.* Dover, NJ: Army Armament Research and Development Center, Large Caliber Weapons Systems Laboratory, 1978.

[183] R. Tisdale, “Optical Properties of Sublimed 2, 4, 6-Trinitrotoluene,” United States Naval Postgraduate School, 1960.

[184] M. a Jarzembski, M. L. Norman, K. a Fuller, V. Srivastava, and D. R. Cutten, “Complex refractive index of ammonium nitrate in the 2-20-micron spectral range.,” *Appl. Opt.*, vol. 42, no. 6, pp. 922–30, Mar. 2003.

[185] D. Daniels, “Ground penetrating radar for buried landmine and IED detection,” in *Unexploded Ordnance Detection and Mitigation*, 2009, pp. 89–111.

[186] E. B. Greenhill and S. R. McDonald, “Surface Free-Energy of Solid Paraffin Wax,” *Nature*, vol. 171, p. 37, 1953.

[187] A. Harrison, E. Bilgili, S. P. Beaudoin, and L. S. Taylor, “Atomic force microscope infrared spectroscopy of organic nanocrystals,” *Anal. Chem.*, vol. 85, no. 23, pp. 11449–11455, 2013.

[188] K. R. Kamath, J. J. Barry, and K. M. Miller, “The Taxus drug-eluting stent: a new paradigm in controlled drug delivery.,” *Adv. Drug Deliv. Rev.*, vol. 58, no. 3, pp. 412–36, Jun. 2006.

[189] L. Sievens-Figueroa, A. Bhakay, J. I. Jerez-Rozo, N. Pandya, R. J. Romañach, B. Michniak-Kohn, Z. Iqbal, E. Bilgili, and R. N. Davé, “Preparation and characterization of hydroxypropyl methyl cellulose films containing stable BCS Class II drug nanoparticles for pharmaceutical applications.,” *Int. J. Pharm.*, vol. 423, no. 2, pp. 496–508, Feb. 2012.

[190] A. Bhakay, R. Davé, and E. Bilgili, “Recovery of BCS Class II drugs during aqueous redispersion of core–shell type nanocomposite particles produced via fluidized bed coating,” *Powder Technol.*, vol. 236, pp. 221–234, Feb. 2013.

[191] B. Van Eerdenbrugh and L. S. Taylor, “Application of mid-IR spectroscopy for the characterization of pharmaceutical systems.,” *Int. J. Pharm.*, vol. 417, no. 1–2, pp. 3–16, Sep. 2011.

[192] Q. Zhu, L. S. Taylor, and M. T. Harris, “Evaluation of the microstructure of semicrystalline solid dispersions.,” *Mol. Pharm.*, vol. 7, no. 4, pp. 1291–300, Aug. 2010.

[193] S. Datta and D. J. W. Grant, “Crystal structures of drugs: advances in determination, prediction and engineering.,” *Nat. Rev. Drug Discov.*, vol. 3, no. 1, pp. 42–57, Jan. 2004.

[194] M. Zilberman and J. J. Elsner, “Antibiotic-eluting medical devices for various applications.,” *J. Control. Release*, vol. 130, no. 3, pp. 202–15, Sep. 2008.

[195] B. Van Eerdenbrugh, M. Lo, K. Kjoller, C. Marcott, and L. S. Taylor, “Nanoscale Mid-Infrared Imaging of Phase Separation in a Drug–Polymer Blend,” *J. Pharm. Sci.*, vol. 101, no. 6, pp. 2066–2073, 2012.

[196] C. Petibois, M. Piccinini, M. C. Guidi, and A. Marcelli, “Facing the challenge of biosample imaging by FTIR with a synchrotron radiation source.,” *J. Synchrotron Radiat.*, vol. 17, no. 1, pp. 1–11, Jan. 2010.

[197] E. Levenson, P. Lerch, and M. C. Martin, “Infrared imaging: Synchrotrons vs. arrays, resolution vs. speed,” *Infrared Phys. Technol.*, vol. 49, no. 1–2, pp. 45–52, Sep. 2006.

[198] E. Levenson, P. Lerch, and M. C. Martin, “Spatial resolution limits for synchrotron-based infrared spectromicroscopy,” *Infrared Phys. Technol.*, vol. 51, no. 5, pp. 413–416, May 2008.

[199] A. Dazzi, C. Prater, Q. Hu, D. B. Chase, J. F. Rabolt, and C. Marcott, “AFM-IR: Combining Atomic Force Microscopy and Infrared Spectroscopy for Nanoscale Chemical Characterization,” *Appl. Spectrosc.*, vol. 66, no. 12, pp. 1365–1384, 2012.

[200] T. Taubner, R. Hillenbrand, and F. Keilmann, “Nanoscale polymer recognition by spectral signature in scattering infrared near-field microscopy,” *Appl. Phys. Lett.*, vol. 85, no. 21, p. 5064, 2004.

[201] F. Huth, A. Govyadinov, S. Amarie, W. Nuansing, F. Keilmann, and R. Hillenbrand, “Nano-FTIR absorption spectroscopy of molecular fingerprints at 20 nm spatial resolution.,” *Nano Lett.*, vol. 12, no. 8, pp. 3973–8, Aug. 2012.

[202] X. G. Xu, M. Rang, I. M. Craig, and M. B. Raschke, “Pushing the Sample-Size Limit of Infrared Vibrational Nanospectroscopy: From Monolayer toward Single Molecule Sensitivity,” *J. Phys. Chem. Lett.*, vol. 3, no. 13, pp. 1836–1841, Jul. 2012.

[203] S. Amarie, P. Zaslansky, Y. Kajihara, E. Griesshaber, W. W. Schmahl, and F. Keilmann, “Nano-FTIR chemical mapping of minerals in biological materials.,” *Beilstein J. Nanotechnol.*, vol. 3, pp. 312–23, Jan. 2012.

[204] A. Dazzi, R. Prazeres, F. Glotin, and J. M. Ortega, “Local infrared microspectroscopy with subwavelength spatial resolution with an atomic force microscope tip used as a photothermal sensor.,” *Opt. Lett.*, vol. 30, no. 18, pp. 2388–90, Sep. 2005.

[205] A. Dazzi, R. Prazeres, F. Glotin, and J. M. Ortega, “Subwavelength infrared spectromicroscopy using an AFM as a local absorption sensor,” *Infrared Phys. Technol.*, vol. 49, no. 1–2, pp. 113–121, Sep. 2006.

[206] C. Mayet, a Dazzi, R. Prazeres, F. Allot, F. Glotin, and J. M. Ortega, “Sub-100 nm IR spectromicroscopy of living cells.,” *Opt. Lett.*, vol. 33, no. 14, pp. 1611–3, Jul. 2008.

[207] A. Dazzi, F. Glotin, and R. Carminati, “Theory of infrared nanospectroscopy by photothermal induced resonance,” *J. Appl. Phys.*, vol. 107, no. 12, p. 124519, 2010.

[208] T. Awatani, H. Midorikawa, N. Kojima, J. Ye, and C. Marcott, “Morphology of water transport channels and hydrophobic clusters in Nafion from high spatial resolution AFM-IR spectroscopy and imaging,” *Electrochem. commun.*, vol. 30, pp. 5–8, May 2013.

[209] J. R. Felts, H. Cho, M.-F. Yu, L. a. Bergman, A. F. Vakakis, and W. P. King, “Atomic force microscope infrared spectroscopy on 15 nm scale polymer nanostructures,” *Rev. Sci. Instrum.*, vol. 84, no. 2, p. 023709, 2013.

[210] J. Felts, K. Kjoller, M. Lo, C. Prater, and W. King, “Nanometer-Scale Infrared Spectroscopy of Heterogeneous Polymer Nanostructures Fabricated by Tip-Based Nanofabrication,” *ACS Nano*, vol. 6, no. 9, pp. 8015–8021, 2012.

[211] A. M. Katzenmeyer, V. Aksyuk, and A. Centrone, “Nanoscale infrared spectroscopy: improving the spectral range of the photothermal induced resonance technique.,” *Anal. Chem.*, vol. 85, no. 4, pp. 1972–9, Feb. 2013.

[212] K. Kjoller, J. R. Felts, D. Cook, C. B. Prater, and W. P. King, “High-sensitivity nanometer-scale infrared spectroscopy using a contact mode microcantilever with an internal resonator paddle.,” *Nanotechnology*, vol. 21, no. 18, p. 185705, May 2010.

[213] B. Lahiri, G. Holland, and A. Centrone, “Chemical Imaging Beyond the Diffraction Limit: Experimental Validation of the PTIR Technique.,” *Small*, no. 1, pp. 1–7, Oct. 2012.

[214] M. Lo, C. Prater, A. Dazzi, R. Shetty, and K. Kjoller, “Nanoscale chemical composition mapping of polymers at 100nm spatial resolution with AFM-based IR spectroscopy,” *Proc. SPIE*, vol. 8373, p. 83730L–83730L–4, May 2012.

[215] B. Van Eerdenbrugh, M. Lo, K. Kjoller, C. Marcott, and L. S. Taylor, “Nanoscale mid-infrared evaluation of the miscibility behavior of blends of dextran or maltodextrin with poly(vinylpyrrolidone).,” *Mol. Pharm.*, vol. 9, no. 5, pp. 1459–69, May 2012.

[216] A. Dazzi, R. Prazeres, F. Glotin, J. M. Ortega, M. Al-Sawaftah, and M. de Frutos, “Chemical mapping of the distribution of viruses into infected bacteria with a photothermal method.,” *Ultramicroscopy*, vol. 108, no. 7, pp. 635–41, Jun. 2008.

[217] C. Policar, J. B. Waern, M.-A. Plamont, S. Clède, C. Mayet, R. Prazeres, J.-M. Ortega, A. Vessières, and A. Dazzi, “Subcellular IR imaging of a metal-carbonyl moiety using photothermally induced resonance.,” *Angew. Chem. Int. Ed. Engl.*, vol. 50, no. 4, pp. 860–4, Jan. 2011.

[218] E. Bilgili and A. Afolabi, “A combined microhydrodynamics-polymer adsorption analysis for elucidation of the roles of stabilizers in wet stirred media milling.,” *Int. J. Pharm.*, vol. 439, no. 1–2, pp. 193–206, Dec. 2012.

[219] J. E. Page and S. Staniforth, “Griseofulvin analogues. Part V. Infrared absorption,” *J. Chem. Soc.*, pp. 1292–1303, 1962.

[220] J. Houel, E. Homeyer, S. Sauvage, P. Boucad, A. Dazzi, R. Prazeres, and J.-M. Ortega, “Midinfrared absorption measured at a lambda/400 resolution with an atomic force microscope,” *Opt. Express*, vol. 17, no. 13, pp. 1053–1057, 2009.

[221] S. Sauvage, a. Driss, F. Réveret, P. Boucaud, a. Dazzi, R. Prazeres, F. Glotin, J.-M. Ortéga, a. Miard, Y. Halioua, F. Raineri, I. Sagnes, and a. Lemaître, “Homogeneous broadening of the S to P transition in InGaAs/GaAs quantum dots measured by infrared absorption imaging with nanoscale resolution,” *Phys. Rev. B*, vol. 83, no. 3, p. 035302, Jan. 2011.

VITA

VITA

Aaron Harrison began studying Chemical Engineering at Brigham Young University in 2004 after receiving the Chemical Engineering Entering Freshman Scholarship. He then postponed his studies to serve as a missionary for the Church of Jesus Christ of Latter-day Saints in Russia from 2005 to 2007. Upon returning to BYU, he immediately began undergraduate research with the Design Institute for Physical Properties (DIPPR) with a focus on thermodynamic properties of pure component materials and liquid-liquid mixtures of biofuels. He received his B.S. in Chemical Engineering from Brigham Young University in August 2011. Following graduation he began his graduate work at Purdue University under Stephen Beaudoin. He will graduate with his PhD in December 2015.